Cardiac Output Estimation from Arterial Blood Pressure Waveforms using the MIMIC II Database

by

Tiffany Chen

Bachelor of Science in Electrical Science and Engineering,
Massachusetts Institute of Technology (2008)

Submitted to the Department of Electrical Engineering
and Computer Science
in partial fulfillment of the requirements for the degree of

Master of Engineering in Electrical Engineering and Computer Science

at the

MASSACHUSETTS INSTITUTE OF TECHNOLOGY

June 2009

© Massachusetts Institute of Technology 2009. All rights reserved.

Author . . . .
Department of Electrical Engineering
and Computer Science
May 22, 2009

Certified by . . . .
Roger G. Mark
Distinguished Professor in Health Sciences and Technology and
Electrical Engineering and Computer Science
Thesis Supervisor

Accepted by . . . .
Arthur C. Smith
Chairman, Department Committee on Graduate Theses

Cardiac Output Estimation from Arterial Blood Pressure Waveforms using the MIMIC II Database

by

Tiffany Chen

Submitted to the Department of Electrical Engineering
and Computer Science
on May 22, 2009, in partial fulfillment of the
requirements for the degree of
Master of Engineering in Electrical Engineering and Computer Science

Abstract

The effect of signal quality on the accuracy of cardiac output (CO) estimation from arterial blood pressure (ABP) was evaluated using data from the MIMIC II database. Thermodilution CO (TCO) was the gold standard, and a total of 121 records with 1,497 TCO measurements were used. Six lumped-parameter and systolic area CO estimators were tested, using ABP features and a robust heart rate (HR) estimate. Signal quality indices for ABP and HR were calculated using previously described metrics. For retrospective analysis, results showed that the Liljestrand estimator yielded the lowest error for all levels of signal quality and for any single estimator when using five or more calibration points. Increasing signal quality decreased error and only marginally reduced the amount of available data, as a signal quality level of 90% preserved sufficient data for almost continuous CO estimation. At the recommended signal quality thresholds, the lowest gross root mean square normalized error (RMSNE) was found to be 15.4% (or 0.74 L/min) and average RMSNE was 13.7% (0.71 L/min). Based on these results, a linear combination (LC) of the six CO estimation methods was developed and proved superior to all other methods when up to 13 TCO calibration values were used.

The clinical utility of the CO estimates were examined by correlating changes in four vasoactive medication doses with corresponding changes in estimated resistance, which was derived from mean ABP and estimated CO. Regression analysis failed to show a clear correlation between dose level and estimated resistance for the Liljestrand and LC estimators except for neosynephrine, revealing the limitations of current SQI methods in ensuring signal fidelity. Examples of types of non-physiological or artifactual ABP waveforms are shown, and a potential damping detection method is proposed.

Thesis Supervisor: Roger G. Mark
Title: Distinguished Professor in Health Sciences and Technology and Electrical Engineering and Computer Science

Acknowledgments

First off, I would like to thank my thesis supervisor Prof. Roger Mark. His insight, knowledge, and humor has made the past year at LCP a great experience. Scrutinizing over patients on the annotation station with him has made me appreciate the complexities of human physiology. His attention to detail and willingness to spend time with each of his students has made him a respected teacher.

I'd like to thank the LCP crew, particularly Dr. Gari Clifford. While trying to convince me that the real world is a scam, he is always full of ideas for new projects or potential solutions to problems I've encountered while working at LCP and has provided valuable signal processing advice for my project, and for this I am grateful for. I would also like to thank database guru Mauro Villarroel, who has made me appreciate the orange chicken that I had believed was just another figment of Americanized Chinese food, for his help on all my computer and database problems that I have managed to get myself into; Omar Abdala, for his critical eye for statistical approaches to analyze results and his reassurances that people have indeed graduated on time from this lab; Daniel Scott, for his choice of Bertucci's pizza at group meetings and his prompt solutions to my broken SQL queries; Li-Wei Lehman, for her practicality in problem solving (and also in making sure the lab doesn't get sued); and George Moody, for the girl scout cookies he provides and also for the solutions to my occasional missing files and WFDB difficulties.

I'd also like to thank the students that have come and gone through the lab whom I have become friends with beyond the walls of E25-505: Shamim Nemati, for introducing us to what a "normal" MIT graduate student is like and for being a great TA, and last but by far not the least, Anagha Deshmane, my fellow M.Eng-er, who has provided countless hours of company and entertainment with her random outbursts and unique taste in music.

I would not have been able to get here today without my family and friends. Thanks to Mom, Dad, and Jayme for supporting me and giving me the opportunities to pursue my interests. Special thanks to the fellow '08s who have accompanied me in my adventures since freshman year.

Thanks for a great year.

The work described was supported by Grant Number RO1-EB001659 from the National Institute of Biomedical Imaging and Bioengineering. The content is solely the responsibility of the author and does not necessarily represent the official views of the National Institute of Biomedical Imaging and Bioengineering or the National Institutes of Health.

Contents

1 Introduction **19**

1.1 Cardiovascular System Background 19

1.2 Motivation for Cardiac Output Estimation 20

1.3 Arterial Blood Pressure 25

1.4 MIMIC II Database 27

1.5 ABP Signal Quality Index 28

1.6 HR Estimation and HRSQI 31

1.7 Project Scope and Goals 33

2 Cardiac Output Estimation **35**

2.1 Cardiac Output Estimation Theory 35

2.1.1 Lumped-Parameter Models 36

2.1.2 Pressure-Area Methods 39

2.2 Evaluation Procedure 40

2.2.1 Database-specific processing 41

2.2.2 Feature extraction 42

2.2.3 SQI Correction 43

2.2.4 CO Estimation 44

2.3 Results 47

2.3.1 Error Criteria 47

2.3.2 Estimator Comparison 48

2.3.3 HRSQI and ABPSQI Thresholds 49

2.3.4 Window size 50

2.3.5 Ordering of mean and median averaging 56
2.3.6 Window threshold 57
2.3.7 Analysis at recommended parameters 58
2.4 Discussion 63

3 Estimated Peripheral Resistance & Vasoactive Drugs 71
3.1 Vasoactive Drugs 71
3.1.1 Dobutamine 72
3.1.2 Dopamine 72
3.1.3 Levophed 73
3.1.4 Neosynephrine (Phenylephrine) 73
3.2 Experimental Procedure 73
3.2.1 Patient selection 73
3.2.2 Estimated resistance 73
3.2.3 Event identification 75
3.2.4 Estimated resistance changes 75
3.2.5 Dose level changes 77
3.2.6 Outlier rejection 78
3.3 Results 82
3.3.1 Proportion of expected events 82
3.3.2 Regression analysis for $\Delta\hat{R}$ and ΔD 83
3.3.3 Regression analysis for $\nabla\hat{R}$ and ∇D 87
3.4 Discussion 90

4 Limitations of Signal Quality Indices 93
4.1 SQI for ABP 93
4.1.1 Saturation 94
4.1.2 Systolic or diastolic pressure jumps 95
4.1.3 Gradual artifacts requiring HR examination 98
4.2 Proposed damping detection method 100
4.2.1 Flushing detection 105

4.2.2 Envelope extraction 106
4.2.3 Fidelity search 108

5 Conclusion **111**
5.1 Summary 111
5.2 Areas for future work 112

List of Figures

1-1 Cardiovascular system. 21

1-2 Example of severe acute hemorrhage. 22

1-3 Typical thermodilution curve 23

1-4 Cardiac cycle. 26

1-5 Arterial blood pressure from a MIMIC II patient. 27

1-6 A clinical ABP waveform with jSQI designated at the bottom, flagging regions of abnormality. 30

1-7 Outline of wSQI procedure. wSQI uses fuzzy logic and fuzzy reprentation to determine a continuous signal quality index for blood pressure. 30

1-8 Clinical ABP and ECG waveforms with wSQI designated at the bottom. Note that wSQI lags one beat behind waveforms. 31

1-9 A two-lead ECG waveform and corresponding ECG SQI. ECGSQI is derived from combining several quality indices related to beat detecton (bSQI), inter-channel agreement (iSQI), Gassianity (kSQI), and spectral coherence (sSQI). 32

2-1 Mean arterial pressure model. P_m, mean arterial pressure; R, peripheral resistance; Q cardiac output. 37

2-2 Windkessel model. $P(t)$, arterial pressure; R, peripheral resistance; $Q(t)$ cardiac output; C compliance. 38

2-3 Liljestrand nonlinear compliance model. Compliance varies according to systolic and diastolic pressure. $P(t)$, arterial pressure; R, peripheral resistance; $Q(t)$ cardiac output; C compliance. 39

2-4 Systolic area estimation. Stroke volume is proportional to the area of the shaded region. 40
2-5 Cardiac output estimation and evaluation procedure. 41
2-6 Beat extraction based on wabp. The SSF function amplifies the rising portion of each beat. 42
2-7 Distribution of records with thermodilution points taken during periods of clean SQI. 44
2-8 Thermodilution value distribution. 45
2-9 Time in hours between thermodilution measurements. Mean time is 3.1 hours, median time is 2.1 hours, and standard deviation is 8.8 hours. 46
2-10 Case ID a40006 with and without SQI correction. 47
2-11 Estimator comparison at different ABPSQI thresholds. 49
2-12 Case ID a40006 with SQI correction 51
2-13 Case ID a40075 with SQI correction. 52
2-14 CO estimation errors at different ABPSQI and HRSQI thresholds using the RMSNE error criteria for the Liljestrand method. 53
2-15 CO estimation errors at different ABPSQI and HRSQI thresholds using the RMSE error criteria for the Liljestrand method. 54
2-16 Data availability at different ABPSQI and HRSQI thresholds. 55
2-17 Effect of window size and ABPSQI threshold on CO estimation error using the Liljestrand method. 56
2-18 Effect of performing mean or median operation before and after CO estimation using the Liljestrand method. 57
2-19 Effect of minimum number of good beats in a window. 58
2-20 Calibration constant histogram for Mean Arterial Pressure. 60
2-21 Calibration constant histogram for Windkessel. 60
2-22 Calibration constant histogram for Liljestrand nonlinear compliance. . 60
2-23 Calibration constant histogram for Herd. 60
2-24 Calibration constant histogram for Systolic area. 60
2-25 Calibration constant histogram for Wesseling. 60

2-26 Calibration constant linear regression with thermodilution for Mean Arterial Pressure. 61

2-27 Calibration constant linear regression with thermodilution for Windkessel. 61

2-28 Calibration constant linear regression with thermodilution for Liljestrand nonlinear compliance. 61

2-29 Calibration constant linear regression with thermodilution for Herd. . 61

2-30 Calibration constant linear regression with thermodilution for Systolic area. 61

2-31 Calibration constant linear regression with thermodilution for Wesseling. 61

2-32 Normalized error, $\left(\frac{\text{ECO}-\text{TCO}}{\text{TCO}}\right)(100\%)$, at a range of thermodilution values. 62

2-33 Absolute error, $\text{ECO} - \text{TCO}$, at a range of thermodilution values. . . 63

2-34 RMSNE as a function of heart rate. 64

2-35 RMSE as a function of heart rate. 64

2-36 RMSNE as a function of mean ABP. 65

2-37 RMSE as a function of mean ABP. 65

2-38 RMSNE as a function of pulse pressure. 66

2-39 RMSE as a function of pulse pressure. 66

2-40 5% bootstrap Mean Square Error (MSE) with raw estimations. The estimators are in the following order: 1) mean arterial pressure, 2) Windkessel, 3) Herd, 4) Liljestrand, 5) Systolic Area, 6) Wesseling, and 7) LC. Errors bars indicate standard deviations over 20 runs. . . 68

3-1 P_m, ECO, $\hat{R}$, and levophed doses for a41244. 76

3-2 Distribution of $\Delta\hat{R}$ and ΔD for vasoconstrictors for the Liljestrand estimator. The green and red ellipses represent the 2 and 3 standard deviation boundaries of the joint distribution. 78

3-3 Distribution of $\Delta\hat{R}$ and ΔD for vasodilators for the Liljestrand estimator. The green and red ellipses represent the 2 and 3 standard deviation boundaries of the joint distribution. 79
3-4 Distribution of $\nabla\hat{R}$ and ∇D for vasoconstrictors for the Liljestrand estimator. The green and red ellipses represent the 2 and 3 standard deviation boundaries of the joint distribution. 79
3-5 Distribution of $\nabla\hat{R}$ and ∇D for vasodilators for the Liljestrand estimator. The green and red ellipses represent the 2 and 3 standard deviation boundaries of the joint distribution. 80
3-6 Distribution of $\Delta\hat{R}$ and ΔD for vasoconstrictors for the LC estimator. 80
3-7 Distribution of $\Delta\hat{R}$ and ΔD for vasodilators for the LC estimator. . . 81
3-8 Distribution of $\nabla\hat{R}$ and ∇D for vasoconstrictors for the LC estimator. 81
3-9 Distribution of $\nabla\hat{R}$ and ∇D for vasodilators for the LC estimator. . . 82
3-10 Medication changes and corresponding resistance changes for each event, organized by drug effect, for Liljestrand estimator. 84
3-11 Medication changes and corresponding resistance changes for each event, organized by medication, for Liljestrand estimator. 84
3-12 Medication changes and corresponding resistance changes for each event, organized by drug effect, for LC estimator. 85
3-13 Medication changes and corresponding resistance changes for each event, organized by medication, for LC estimator. 85
3-14 Medication slopes and corresponding resistance slopes for each event, organized by drug effect for the Liljestrand estimator. 87
3-15 Medication slopes and corresponding resistance slopes for each event, organized by medication for the Liljestrand estimator. 88
3-16 Medication slopes and corresponding resistance slopes for each event, organized by drug effect for the LC estimator. 88
3-17 Medication slopes and corresponding resistance slopes for each event, organized by medication for the LC estimator. 89

4-1 Estimated CO, estimated R, HR, and ABP for a41232. Periods of signal quality greater than 90 for HRSQI and ABPSQI are flagged on their respective plots. 96

4-2 Estimated CO, estimated R, HR, and ABP for a40694. Periods of signal quality greater than 90 for HRSQI and ABPSQI are flagged on their respective plots. 97

4-3 Example of artifact from a40694: saturation to mean. 98

4-4 Estimated CO, estimated R, HR, and ABP for a40542. Periods of signal quality greater than 90 for HRSQI and ABPSQI are flagged on their respective plots. 99

4-5 Estimated CO, estimated R, HR, and ABP for a40638. Periods of signal quality greater than 90 for HRSQI and ABPSQI are flagged on their respective plots. 101

4-6 Estimated CO, estimated R, HR, and ABP for a41895. Periods of signal quality greater than 90 for HRSQI and ABPSQI are flagged on their respective plots. 102

4-7 Estimated CO, estimated R, HR, and ABP for a41681. Periods of signal quality greater than 90 for HRSQI and ABPSQI are flagged on their respective plots. 103

4-8 Estimated CO, estimated R, HR, and ABP for a40968. Thermodilution is shown in red with error bars of 20%. Periods of signal quality greater than 90 for HRSQI and ABPSQI are flagged on their respective plots. 104

4-9 Example of artifact from a41232: damping and consequent flush. . . . 105

4-10 Proposed damping detection method. 106

4-11 Envelope extraction for a40022. 107

4-12 Envelope extraction for a40022 using the RMS method. 108

4-13 Envelope extraction for a40022 using the Hilbert method. 108

4-14 Fidelity search for a41661. 109

List of Tables

1.1 jSQI criteria. 29

2.1 Cardiac output estimators indexed by i. P_m, mean arterial pressure; P_p, pulse pressure; P_d, diastolic arterial pressure; P_s, systolic arterial pressure; h, heart rate; A_s, area during systole. 36
2.2 Extracted ABP Features. 43
2.3 Statistics for calibration constants k_i for different estimators at recommended SQI thresholds to remove noisy data. 59

3.1 List of vasoactive medications and their effects on peripheral resistance. 72
3.2 List of ICD-9 codes used to identify patients with septic shock, cardiogenic shock, and hemorrhage. 74
3.3 Expected estimated resistance and medication changes. 83
3.4 $\Delta\hat{R}$ and ΔD regression results for the Liljestrand estimator. Linear regression line in the form of $y = ax + b$. 86
3.5 $\Delta\hat{R}$ and ΔD regression results for the LC estimator. Linear regression line in the form of $y = ax + b$. 86
3.6 $\nabla\hat{R}$ and ∇D regression results for the Liljestrand estimator. Linear regression line in the form of $y = ax + b$. 87
3.7 $\nabla\hat{R}$ and ∇D regression results for the LC estimator. Linear regression line in the form of $y = ax + b$. 89

Chapter 1

Introduction

Modern intensive care units (ICUs) measure a large number of physiologic signals that are intended to provide clinicians comprehensive information to diagnose and treat patients. However, the quantity of information can be overwhelming to the clinician and hinder the integration of relevant data crucial to the patient's condition. One of the many signals typically measured in an ICU setting is blood pressure, which can be processed and interpreted to aid clinicians in better tracking of the patient's state.

1.1 Cardiovascular System Background

The major functions of the cardiovascular system are to perfuse the vital organs with blood, provide oxygen to tissues, and distribute essential molecules to the cells while carrying away metabolic waste products to maintain the body's internal environment. As illustrated in Fig.1-1, blood is carried from the heart to the body through the arteries, thick-walled vessels that carry the blood at high pressures. The arteries branch into a series of arterioles, which then in turn branch into capillaries. These capillaries, with their walls only a single layer of cells thick, are the site of exchange of oxygen, carbon dioxide, nutrients, and wastes to and from the tissues. Blood is carried back to the heart through the veins, thin-walled vessels that carry the blood at low pressures. After the blood returns to the right atrium of the heart, it passes into the right ventricle, from which it is ejected into the pulmonary system for gas exchange. Oxygenated blood returns to the heart and fills the left atrium. Blood then fills the left ventricle, and the left ventricle pumps the blood through the systemic circulation system.

Cardiac output (CO) is a measure of the amount of blood pumped by either ventricle. In steady state, the outputs of both ventricles are the same. In a healthy adult male, cardiac output is approximately 5 L/min [7]. Cardiac output can vary, however, according to the body's physiological needs; for example, a well-trained athlete, while exercising, can increase cardiac output to up to 30 L/min to increase the rate of transport of oxygen, nutrients, and wastes [13]. Abnormally low levels of cardiac output can also be an indication of pathology.

1.2 Motivation for Cardiac Output Estimation

Cardiac output is one of the most important hemodynamic signals to measure in patients with compromised cardiovascular performance. Fig.1-2 illustrates the significance of cardiac output monitoring in severe acute hemorrhage, displaying the changes in total peripheral resistance, heart rate, arterial blood pressure, right atrial pressure, and cardiac output during a hemorrhage. Although arterial blood pressure decreases throughout blood loss and drops sharply at approximately 10 minutes after onset of hemorrhage, cardiac filling pressure and cardiac output provide earlier indications of anomalous cardiovascular behavior. This example illustrates the fact that measurements of cardiac output and filling pressure provide information for "early diagnosis, monitoring of disease progression, and titration of therapy in heart failure, shock of any type, sepsis, and during cardiac surgery" [15]. If cardiac output could be measured at more frequent intervals, or even continuously, clinicians could detect abnormalities in the cardiovascular system and execute appropriate interventions sooner.

Currently, cardiac output monitoring in the ICU is monitored invasively and only intermittently. In the ICU, the thermodilution cardiac output (TCO) method, introduced by Fegler in 1954 [12], has been the "gold standard" commonly used to

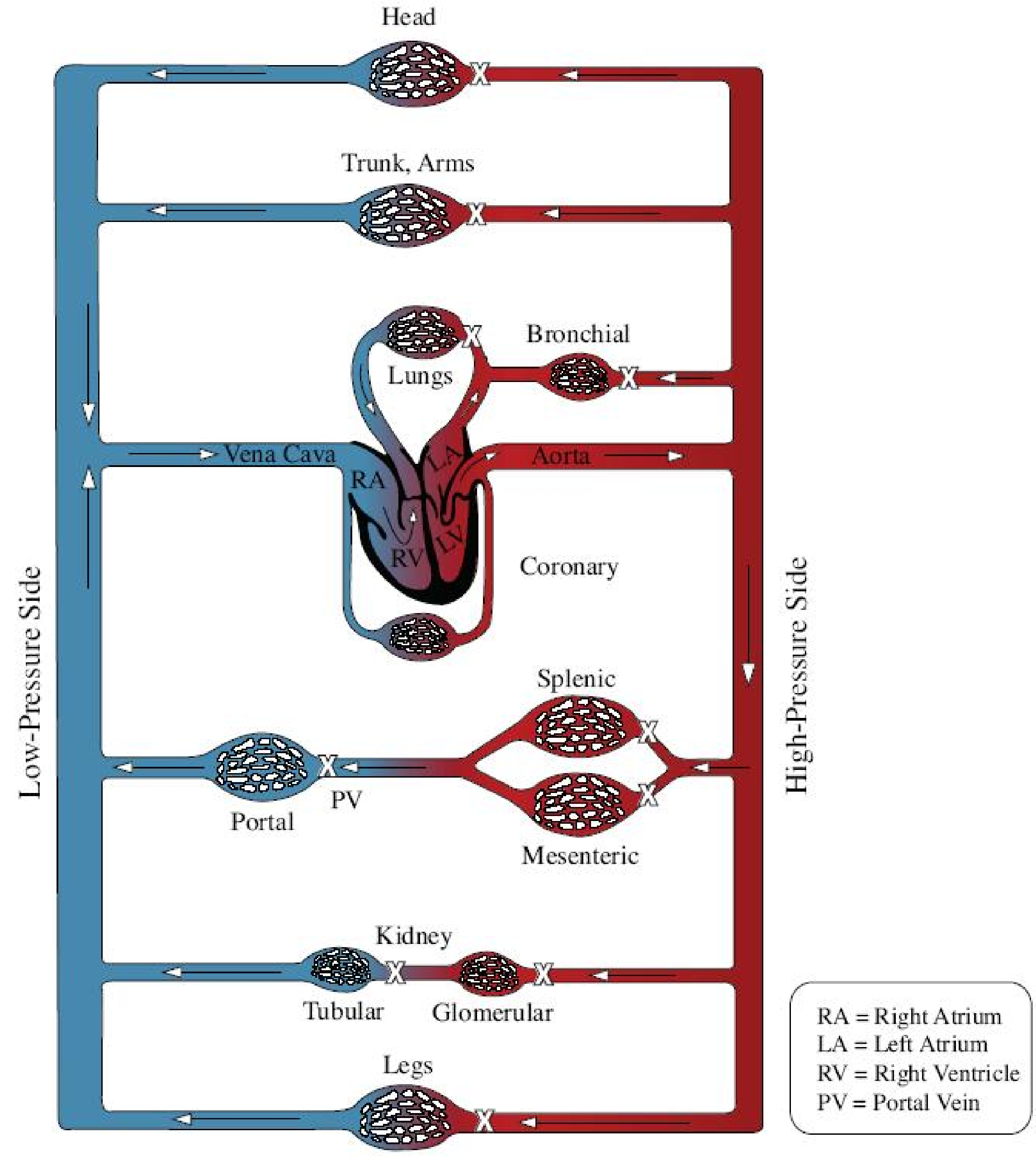
Head
Trunk, Arms
Lungs
Bronchial
Vena Cava
Aorta
RA
LA
RV
LV
Coronary
Low-Pressure Side
High-Pressure Side
Splenic
Portal
PV
Mesenteric
Kidney
Tubular
Glomerular
Legs
RA = Right Atrium
LA = Left Atrium
RV = Right Ventricle
PV = Portal Vein

Figure 1-1: Cardiovascular system. *X*s indicate local control points. The arterial system is displayed on the right, while the venous system is displayed on the left. Adapted from [29].

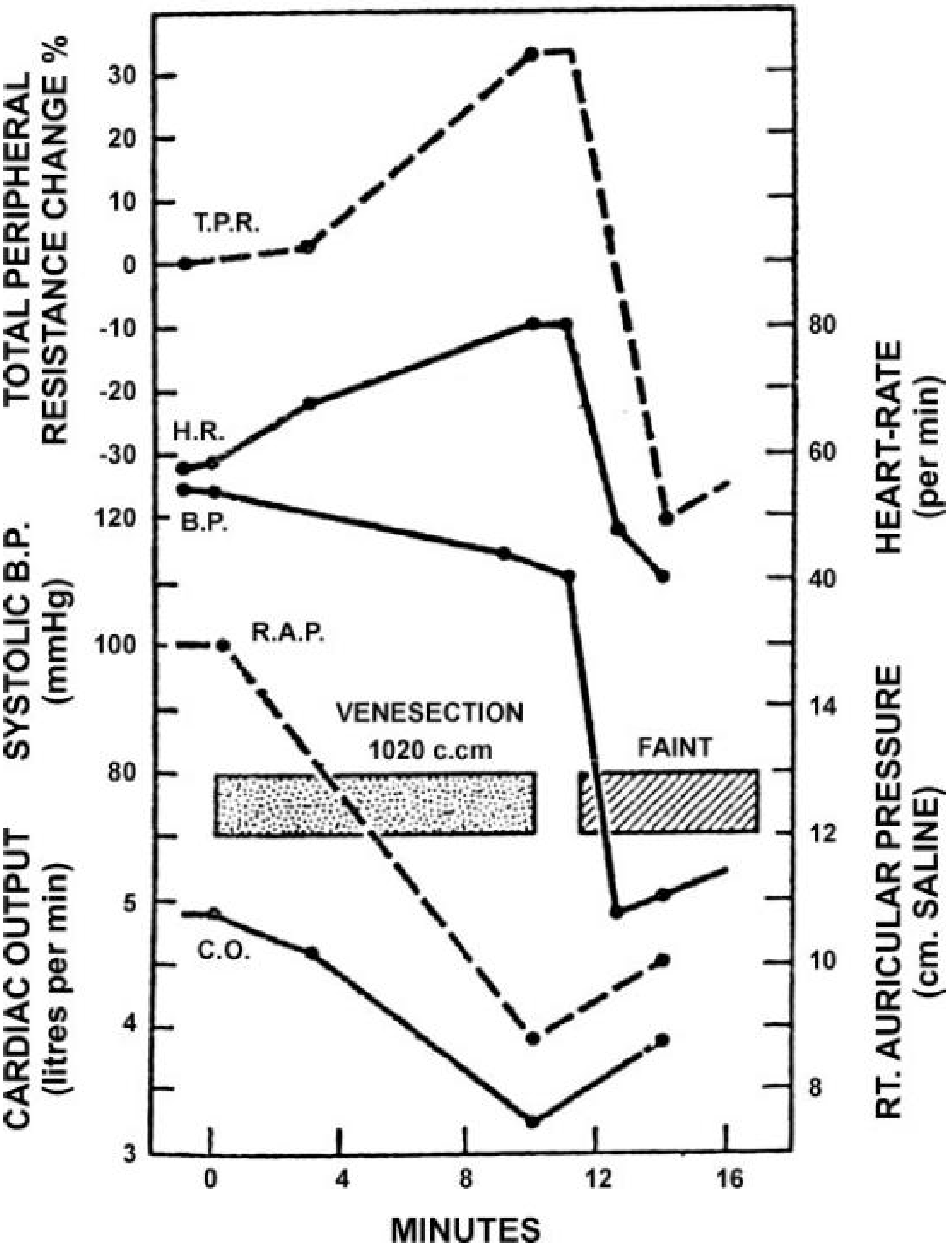

Figure 1-2: Example of severe acute hemorrhage starting at t=0. TPR, total peripheral resistance; HR, heart rate; BP, blood pressure; RAP, right atrial pressure; CO, cardiac output; RT, right. Adapted from [3].

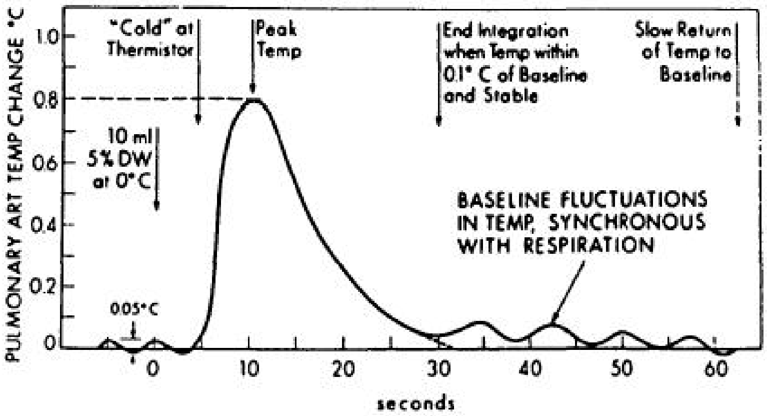

Figure 1-3: Typical thermodilution curve. Baseline fluctuations may reach 0.1 degrees Celsius. Adapted from [31].

measure cardiac output, whereby a bolus of cold solution of saline or dextrose is injected into the right atrium. Temperature change is monitored at the pulmonary artery using a balloon-tipped Swan-Ganz catheter, which involves an invasive procedure that requires threading the catheter through the vena cava and the right heart. Using this method, cardiac output is inversely proportional to the integral of the measured temperature curve, as illustrated in Fig.1-3. This method can only be performed in well-equipped environments such as ICUs or cardiac catheterization labs. Current invasive procedures for monitoring cardiac output increase the potential for complications, including the higher risk of infection and sepsis, and increase the possibilities of morbidity and mortality [6]. Furthermore, TCO measurements can only be taken intermittently to prevent volume overload and to allow for sufficient time for temperature changes to occur in the bloodstream [20]. Therefore, both patients and clinicians would benefit from having a continuous, non-invasive, reliable method of estimating CO.

Other methods of measuring CO exist, but requires additional measurements, tests, and/or equipment. The Fick method derives CO through calculating oxygen consumed over a given period of time by measuring oxygen consumption per minute with a spirometer, oxygen concentration of venous blood from the pulmonary artery, and oxygen concentration of arterial blood from a peripheral artery. Impedance cardiography is a non-invasive method of measuring CO, whereby electrodes are placed on the neck and chest to transmit and detect impedance changes in the thorax. Impedance changes are due to changes in intrathoracic fluid volume and respiration, so changes in blood volume per cardiac cycle can be measured and used to estimate stroke volume and CO, but reliability and reproducibility of measurements have been limited [42]. The Doppler ultrasound method uses reflected sound waves to calculate flow velocity and volume to obtain cardiac output and is a non-invasive, accurate way of measuring CO using a handheld transducer placed over the skin.

The precision for thermodilution measurements is approximately $\pm 10-20\%$ (0.5-1 L/min for a standard 5L/min cardiac output) with a 95% confidence interval [27, 36]. Studies have shown that measuring cardiac output using thermodilution has little bias compared to existing methods such as the Fick method, but other studies show TCO can also overestimate cardiac output by as much as 2.3 L/min [22, 17, 11]. Furthermore, a variety of factors contribute to error in cardiac output estimation by thermodilution: temperature and volume of injectate, rewarming of injectate, timing of injection and respiration, speed and mode of injection, and intravenous fluid administration, among others [31].

Cardiac output is determined by a variety of factors, including heart rate, stroke volume, venous compliance, total peripheral resistance, blood volume, intrathoracic pressure, and cardiac compliance. Many have developed non-invasive or minimally invasive methods to continuously estimate CO [8, 19]. In particular, the arterial blood pressure (ABP) waveform has generated much interest and research for its use in estimating cardiac output. Not only is ABP a routinely measured signal in ICU settings, but measurements are often continuous and less invasive, providing a source of data for continuous CO estimation. Even if CO estimates from ABP are less accurate than existing methods, the derived CO trends can be a powerful tool for clinicians; for example, decreasing CO may indicate shock, and the effectiveness of therapies can be monitored by examining whether or not CO increases to normal levels. Most importantly, CO estimation using ABP requires little to no additional equipment or personnel if the computational power of the existing bedside monitor is sufficient for the numerical calculations required.

1.3 Arterial Blood Pressure

Arterial blood pressure is regulated by cardiovascular control mechanisms and reflects the cardiovascular system function. Fig.1-4 illustrates the pressure changes in a typical cardiac cycle during which the heart fills and ejects blood, along with the associated aortic flow, ventricular volume, heart sounds, venous pulse, and electrocardiogram. The cardiac cycle can be separated into diastolic and systolic phases. During diastole, the ventricles relax and fill with blood, and this phase is approximately two-thirds of the cardiac cycle. During systole, the ventricles contract and pump blood to the pulmonary and systemic systems, creating high pressures in the blood vessels. Diastolic and systolic arterial blood pressures are indicated in Fig.1-5 by P_d and P_s, respectively. The pulse pressure P_p is the difference between the systolic and diastolic pressures. Mean pressure P_m is the time-averaged arterial blood pressure through one cardiac cycle and is approximately equal to the diastolic pressure plus one-third of the pulse pressure. Typical values for systolic and diastolic pressures are 120 mmHg and 80 mmHg, respectively, and blood pressure is often written as 120/80.

In an ICU setting, ABP is frequently measured invasively using a pressure transducer connected by a catheter to an artery. The radial artery (or occasionally the femoral artery) is used due to its ease in cannulation and the low incidence of complications [35]. Systolic and pulse pressures are higher in these large arteries than in the aorta, while diastolic and mean pressures are slightly lower downstream. Eventually, as the blood reaches the arterioles, capillaries, venules, and veins, pulse pressure is absent [7]. Blood pressure can also be measured intermittently and noninvasively using an oscillometric system. ABP fluctuates diurnally with a baseline change of approximately 20 mmHg, with blood pressure being lower at night [2]. Since ICU patients are managed for cardiovascular stability with drugs and are almost always supine, ABP and heart rate are much more restricted in range than for active, healthy subjects [21].

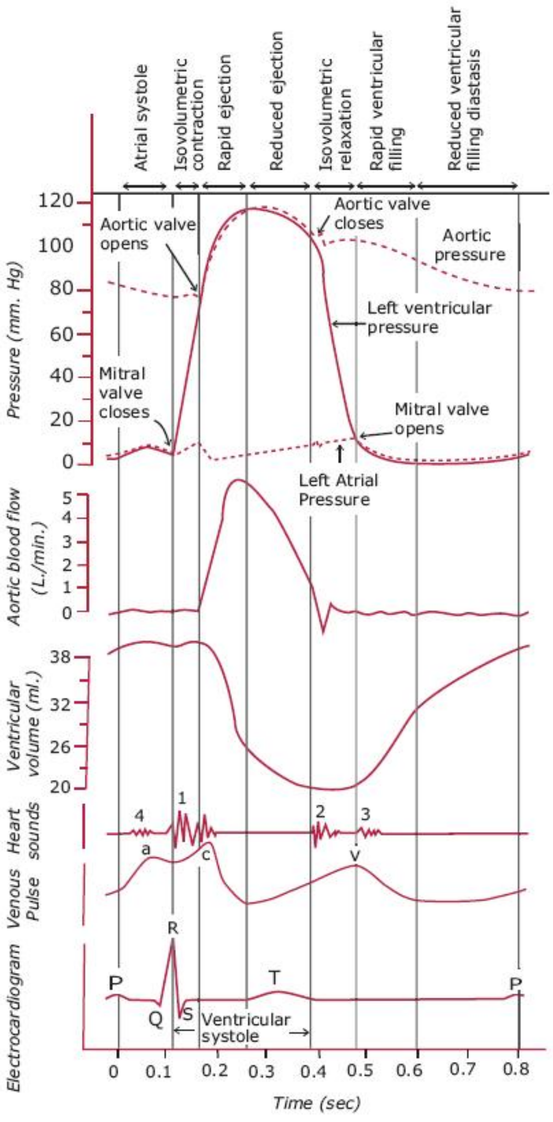

Figure 1-4: Left atrial, aortic, and left ventricular pressure measurements with associated aortic flow, ventricular volume, heart sounds, venous pulse, and electrocardiogram for a complete cardiac cycle in the dog. Adapted from [29].

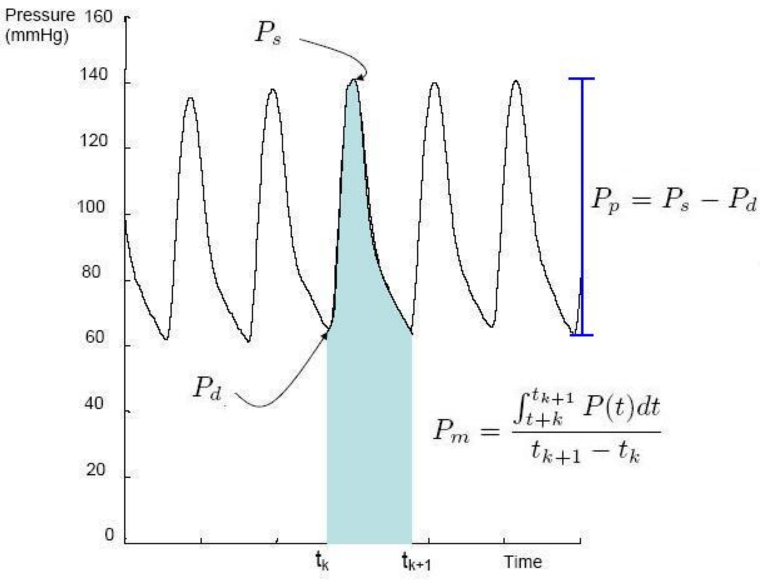

Figure 1-5: Arterial blood pressure from a MIMIC II patient. Adapted from [32].

1.4 MIMIC II Database

The MIT Laboratory of Computational Physiology (LCP) currently collaborates with Philips Healthcare and Beth Israel Deaconess Medical Center in an ongoing effort to collect, develop, and evaluate ICU patient monitoring systems that will improve clinical decision-making. As part of this collaboration, the lab has developed the Multi-Parameter Intelligent Patient Monitoring for Intensive Care (MIMIC) II database, an online database that contains more than 30,000 de-identified records from patients hospitalized at the Beth Israel Deaconess Medical Center in Boston, Massachusetts [34] [5]. More than 4,000 of these records contain physiological data including bedside waveform and physiological trend data. Waveform data are sampled at 125 Hz with 8 or 10 bit resolution and typically include multichannel electrocardiogram traces, arterial blood pressure measurements, central venous pressure waveforms, and pulmonary artery pressure waveforms. Trend data, which are derived from the waveforms, are collected only intermittently and are usually recorded at a rate of 1 sample/min. Derived trends include heart rate, mean, systolic, and diastolic arterial pressure, mean, systolic, and diastolic pulmonary artery pressure, and cardiac output (using thermodilution). Currently, the public MIMIC II database includes 1710 ICU stays with arterial blood pressure waveform and derived measurements, totaling approximately 104,000 hours of data. The database contains 282 trend records with thermodilution measurements, which are measured intermittently. Of these data, 265 patient records contain both arterial blood pressure and thermodilution measurements, totaling 2754 TCO measurements.

1.5 ABP Signal Quality Index

ABP waveform data are prone to artifacts due to patient movement, sensor disconnections, arterial line blockage, or mechanical devices such as intra-aortic balloon pumps. Because the accuracy of CO estimates based on analysis of ABP waveforms is a function of the quality of the ABP waveform, a systematic method needs to be used to remove artifacts or abnormal (non-sinus rhythm) ABP beats. Previous literature has defined signal quality indices (SQI) for both blood pressure and heart rate based on MIMIC II data [25, 24, 37, 44]. For blood pressure signal quality, Li et al combined two independent signal quality assessment methods, $jSQI$ [38] and $wSQI$ [44] to form ABPSQI. For both signal quality metrics, beat extraction is performed using *wabp*, an open-source ABP onset detection algorithm [43].

The $jSQI$ algorithm examines each beat, extracting a series of inter- and intra-beat features and comparing them to a set of maximum or minimum values that are beyond the physiological range. Beats that fail any one of these criteria are flagged as “bad”. Table 1.1 provides a list of these features and associated thresholds beyond which a beat is considered abnormal. For each beat, systolic and diastolic pressures are the local maximum and minimum values within the duration of the beat, while the beat duration is the time difference between adjacent onsets. The first 4 criteria in Table 1.1 impose bounds on the physiologic ranges of each feature. For example, systolic pressures above 300 mmHg are flagged as abnormal. The noise level, w, is defined as the average of all negative slopes in each beat, so high frequency noise, which often contains large negative slopes, is detected. This method of noise detection does not identify low frequency noise such as baseline wander and is dependent on the sampling frequency (125 Hz for the MIMIC II database), since this is a gradient calculation for each sample in a beat. The last 3 criteria in Table 1.1 examine variations between adjacent beats.

Feature	Abnormality criteria
P_s	$P_s > 300$ mmHg
P_d	$P_d < 20$ mmHg
P_m	$P_m < 30$ or $P_m > 200$ mmHg
HR	$HR < 20$ or $HR > 200$ bpm
P_p	$P_p < 20$ mmHg
w	$w <$ -40 mmHg / 100 ms
$P_s[k] - P_s[k-1]$	$\lvert\Delta P_s\rvert > 20$ mmHg
$P_d[k] - P_d[k-1]$	$\lvert\Delta P_d\rvert > 20$ mmHg
$T[k] - T[k-1]$	$\lvert\Delta T\rvert > 2/3$ sec

Table 1.1: jSQI criteria. P_m, mean arterial pressure; P_d, diastolic arterial pressure; P_s, systolic arterial pressure; T, beat duration; HR, instantaneous heart rate as calculated by $60/T$; P_p, pulse pressure; w, noise: mean of negative slopes. Adapted from [38].

$jSQI$ is an *abnormality* index and produces a binary number for each beat with 0 equating to normality and 1 abnormality. Note that an abnormal rating may be due to artifacts or pathophysiology such as an arrhythmia or balloon pump. In Fig.1-6, for example, the abnormal regions are indicated by the two red shaded regions on the x-axis. The final beat in the second abnormal section ending at approximately 25 seconds is labeled as abnormal even though it appears normal because *jSQI* compares this beat to the previously detected beat and looks for similarities. Compared to human annotation, $jSQI$ has a sensitivity of 1.00 and a positive predictivity of 0.91 [38].

The *wSQI* algorithm extracts beat by beat features from ABP, expresses the features using fuzzy representation, and uses a fuzzy reasoning procedure, outlined in Fig.1-7, to produce a continuous SQI between 0 and 1, where 1 is the best signal quality. The features used for this algorithm are systolic blood pressure, diastolic blood pressure, mean blood pressure, maximum positive pressure slope, maximum negative pressure slope, maximum up-slope duration (the maximum duration that the ABP signal continues to rise), maximum duration above threshold (the maximum

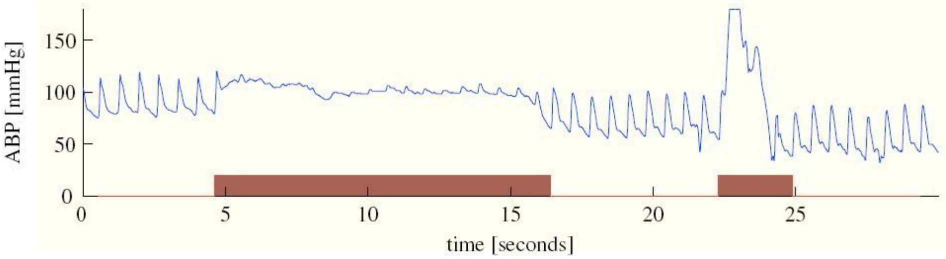

Figure 1-6: A clinical ABP waveform with jSQI designated at the bottom, flagging regions of abnormality. Adapted from [38].

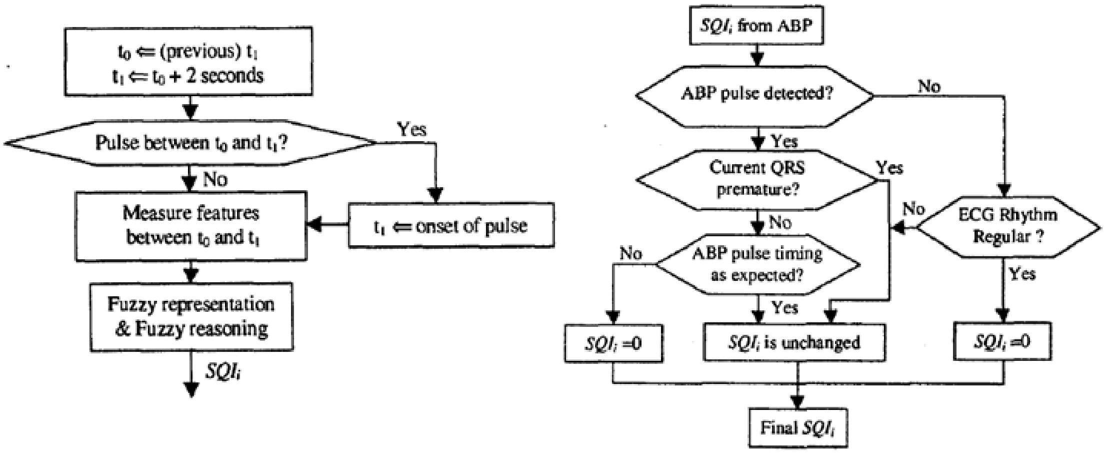
$t_0 \Leftarrow$ (previous) t_1
$t_1 \Leftarrow t_0$ + 2 seconds
Pulse between t_0 and t_1?
Yes
No
Measure features between t_0 and t_1
$t_1 \Leftarrow$ onset of pulse
Fuzzy representation & Fuzzy reasoning
SQI_i
SQI_i from ABP
ABP pulse detected?
No
Yes
Current QRS premature?
Yes
No
ECG Rhythm Regular ?
No
ABP pulse timing as expected?
No
Yes
Yes
SQI_i =0
SQI_i is unchanged
SQI_i =0
Final SQI_i

Figure 1-7: Outline of wSQI procedure. wSQI uses fuzzy logic and fuzzy reprentation to determine a continuous signal quality index for blood pressure. t_0 and t_1 are the start and end times of each blood pressure pulse. Adapted from [44].

duration that the ABP signal stays above a threshold), pulse-to-pulse interval, pulse pressure, and ECG-ABP delay time (the interval between the QRS onset in the ECG and the onset of the following ABP pulse). Fig.1-8 illustrates the output from this algorithm. If an electrocardiogram (ECG) signal is available, detected ABP beat onset times are compared to those extracted from the ECG signal and thresholded. The $wSQI$ algorithm has been shown to have a sensitivity of 99.8% and a positive predictivity of 99.3% on data from the MIMIC I Database, an earlier multiparamter ICU database. $wSQI$ values above 0.5 correspond to good ABP signal quality [44].

To form a signal quality metric for ABP (ABPSQI), Li et al combined $jSQI$ and $wSQI$ using the following method:

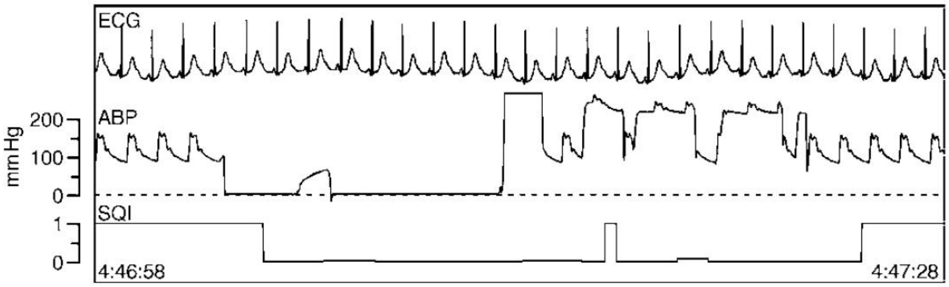

Figure 1-8: Clinical ABP and ECG waveforms with wSQI designated at the bottom. Note that wSQI lags one beat behind waveforms. Adapted from [44].

$$ABPSQI = \begin{cases} wSQI & \text{if } jSQI = 0; \\ wSQI * \eta & \text{if } jSQI = 1. \end{cases}$$

where η is an arbitrary weight that was set to be 0.7.

1.6 HR Estimation and HRSQI

For the CO estimators analyzed in this thesis, blood pressure features are used to estimate stroke volume, which is then is multiplied by heart rate to derive cardiac output. Therefore, reliable heart rate measurements are also an integral component for deriving reliable CO estimates.

Li et al [25] developed a method for robust heart rate estimation by fusing heart rate estimates derived from ABP and ECG. Heart rate is extracted from multiple ECG leads using a weighted Kalman filter to produce a robust heart rate estimate. Meanwhile, ABP heart rate is calculated from ABP waveforms based on beat onset times from *wabp*. HR estimates from both ECG and ABP are tracked with separate Kalman filters that used SQI-weighted update sequences. A fused heart rate is derived by weighting each HR estimate by the SQI-weighted residual errors of each Kalman filter for each HR time series.

For each fused segment, a corresponding signal quality (HRSQI) is computed to indicate its reliability. HRSQI is composed of 2 SQIs: ABPSQI (described in Section

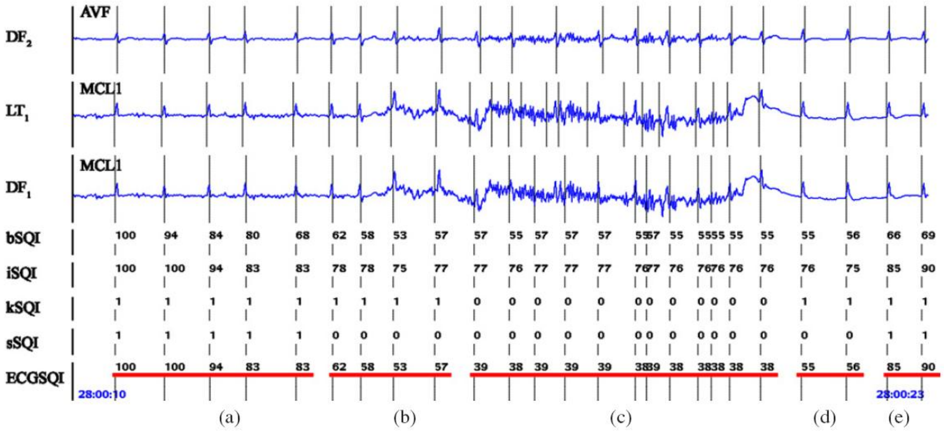

Figure 1-9: A two-lead ECG waveform and corresponding ECG SQI. ECGSQI is derived from combining several quality indices related to beat detecton (bSQI), inter-channel agreement (iSQI), Gassianity (kSQI), and spectral coherence (sSQI). Adapted from [25].

1.5) and ECGSQI. ECGSQI is the signal quality of the ECG heart rate estimation method used to derive the heart rate component from ECG. ECGSQI is formed based on a variety of factors: the comparison of multiple beat detection algorithms on a single lead, beat detection comparison using different ECG leads, kurtosis of the ECG, and spectral distribution of ECG. Fig.1-9 illustrates the ECGSQI on a short section of multi-lead ECG. An ECGSQI value between between 0 and 1 is assigned to the corresponding HR estimates as a metric for the reliability of the ECG-derived HR. ECGSQIs greater than 0.5 indicate a signal from which a fair estimate of HR can be derived, with ECGSQIs greater than 0.7 generally providing an excellent HR estimate.

The reliability of the fused HR is indicated by a composite signal quality measure HRSQI using the following method:

$$HRSQI = \max(ABPSQI, ECGSQI)$$

1.7 Project Scope and Goals

This thesis compares and evaluates the accuracy of CO estimators that use ABP waveform data, using thermodilution measurements of CO as the gold standard. Trends in CO are then related to physiological changes to determine the clinical usefulness of the estimates. The first part of this thesis evaluates and compares the performance of 6 CO estimators on data from MIMIC II, incorporating heart rate, blood pressure, and their corresponding signal quality indices in the estimation process. The accuracies of CO estimates are then compared with thermodilution measurements in the MIMIC II database. Estimated CO errors as a function of estimated CO, heart rate, mean blood pressure, and pulse pressure are also explored.

The second part of this thesis attempts to evaluate the clinical usefulness of CO estimates by analyzing correlations between the administration of vasoactive pressors and the measured and calculated hemodynamics. That is, cardiac output, peripheral resistance (R), and mean arterial blood pressure should change over time following drug delivery. Administration of vasoconstrictors results in an increased peripheral resistance, which is the ratio between mean ABP and cardiac output, while vasodilators result in a decreased peripheral resistance. Estimated peripheral resistance ($\hat{\mathrm{R}}$) is calculated by dividing the mean ABP by estimated CO. By examining changes in $\hat{\mathrm{R}}$ at the vicinity of a stop, start, or significant change in pressor dose, we may evaluate the utility of these estimates in a real-world setting.

Chapter 2

Cardiac Output Estimation

The goal of this section is to produce reliable cardiac output estimates based on blood pressure waveform data. This requires 3 essential components:

1. Reliable ABP measurements
2. Reliable HR measurements
3. An accurate CO estimator method

The CO estimates were evaluated on records from the MIMIC II database [5] with simulataneous ABP waveform & TCO recordings. Patients with intra-aortic balloon pumps or fewer than 5 TCO measurements were not included in the analysis, as consistent with previous literature [37] [39] to provide sufficient calibration points. These restrictions provide 1,497 thermodilution measurements from 121 records for calibration. Thermodilution was used as the gold standard against which the estimated CO was compared.

2.1 Cardiac Output Estimation Theory

A variety of cardiac output estimators have been developed over the past hundred years. The estimators evaluated in this thesis rely on circuit models or pressure-area methods to estimate stroke volume and use heart rate to obtain cardiac output.

A superset of these cardiac output estimators have been evaluated by Sun [37] but focused solely on the use of jSQI for a signal quality metric. The CO estimators evaluated in this study are listed in Table 2.1. The proportionality constant reflects arterial compliance and peripheral resistance factors that may not be calculated using arterial blood pressure waveforms without additional calibration data. The estimators are broken into two general groups by a horizontal line. The first set of estimators are based on lumped-parameter models for cardiovascular circulation. The second set of estimators are based on systolic-area methods.

i	CO estimator	$CO = k_i \cdot below$
1	Mean arterial pressure	P_m
2	Windkessel [10]	$P_p \cdot h$
3	Liljestrand nonlinear compliance [26]	$\left(\frac{P_p}{P_s+P_d}\right) \cdot h$
4	Herd [16]	$(P_m - P_d) \cdot h$
5	Systolic area [40]	$A_s \cdot h$
6	Wesseling [41]	$(163 + h - 0.48 \cdot P_m) \cdot A_s \cdot h$

Table 2.1: Cardiac output estimators indexed by i. P_m, mean arterial pressure; P_p, pulse pressure; P_d, diastolic arterial pressure; P_s, systolic arterial pressure; h, heart rate; A_s, area during systole.

2.1.1 Lumped-Parameter Models

Electrical circuits have been used to model the relationship between CO and ABP, and a number of lumped-parameter models of various complexities have been developed to model circulation. Current is analogous to flow (Q), while voltage is analogous to pressure (P). In the case of circulation, flow is equal to CO, so Q and CO can be used interchangeably.

Method 1: Mean arterial pressure (MAP)

The viscous flow of blood through blood vessels contributes resistance to blood flow, and the determinants of resistance include blood viscosity and radius of the blood vessel. The blood vessels throughout the body can be modeled as resistors in parallel or series. Peripheral resistance (R) is the total equivalent resistance of blood flow

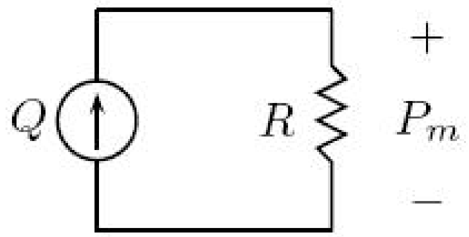

Figure 2-1: Mean arterial pressure model. P_m, mean arterial pressure; R, peripheral resistance; Q cardiac output.

throughout the body. The mean arterial pressure model takes into account peripheral resistance, mainly contributed from arterioles, and models the heart using a current source Q as illustrated in Fig.2-1. This circuit analogy is valid only for time-averaged flow and not intra-beat fluctuations. CO is computed using Ohm's law as follows:

$$Q = k_1 \cdot P_m$$

where P_m is the mean arterial pressure, R is the peripheral resistance, and $k_1 = \frac{1}{R}$.

Method 2: Windkessel

The Windkessel model [10], shown in Fig.2-2, describes the pulsatile phenomenon of arterial blood pressure. As with the mean arterial pressure model, the resistor component corresponds to the resistance of the systemic blood vessels. The capacitor models the compliance of the arteries, which inherently store some blood during the cardiac cycle. Compliance (C) is a measure of the distensibility of the blood vessels, and the capacitor represents the aggregate elastic properties of the systemic peripheral system:

$$C = \frac{\Delta V}{\Delta P}$$

where V represents the volume of blood and P the transmural pressure across the wall of the blood vessel. The heart is modeled by a time-varying current source $Q(t)$ representing blood flow, and each beat of the heart corresponds to an impulse with an area equal to the stroke volume (SV), the amount of blood pumped per beat, such

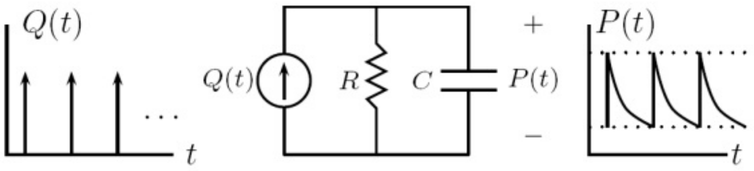

Figure 2-2: Windkessel model. $P(t)$, arterial pressure; R, peripheral resistance; $Q(t)$ cardiac output; C compliance.

that:

$$Q(t) = \sum_n SV_n \cdot \delta(t - t_n)$$

where n is the n^{th} beat over which Q is calculated, t_n is the time of the n^{th} beat, and SV_n is the stroke volume due to the n^{th} beat. The resulting pressure waveform exhibits an exponential decay after each beat within the RC time constant and resembles the physiological arterial pressure waveform, particularly during diastole. The state space equation for the Windkessel model is:

$$C\frac{dP(t)}{dt} + \frac{P(t)}{R} = Q(t)$$

where C is the arterial compliance. By circuit analysis, stroke volume is proportional to the pulse pressure, P_p (the amplitude range of the ABP waveform); heart rate, h; and the compliance, C in steady state such that:

$$Q = k_2 \cdot P_p \cdot h$$

where $k_2 = C$.

Method 3: Liljestrand nonlinear compliance

Compliance varies throughout the cardiac cycle and is dependent on arterial pressure. When pressure increases during systole, blood vessels expand and become stiffer, decreasing incremental compliance. This CO estimator uses a pressure-varying capacitor

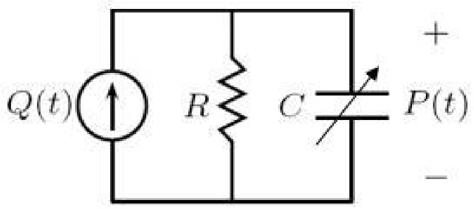

Figure 2-3: Liljestrand nonlinear compliance model. Compliance varies according to systolic and diastolic pressure. $P(t)$, arterial pressure; R, peripheral resistance; $Q(t)$ cardiac output; C compliance.

$C = \frac{k_3}{P_s+P_d}$ to correct for this nonlinearity, as seen in Fig.2-3 [26]:

$$Q = \frac{k_3}{P_s + P_d} \cdot P_p \cdot h$$

where k_3 is an arbitrary constant derived from a measurement of cardiac output using an independent method such as Fick's or thermodilution.

Method 4: Herd

Herd empirically observed that $P_m - P_d$ is proportional to stroke volume [16]. There is no physiological intuition for this assumption, but it corrects for varying compliance, with decreasing compliance as pressure increases. Cardiac output is therefore:

$$Q = k_4 \cdot (P_m - P_d) \cdot h$$

2.1.2 Pressure-Area Methods

Another approach to cardiac output estimation using blood pressure is by approaching the arterial tree from a distributed systems point of view. More specifically, systolic area can be correlated with stroke volume to obtain an estimated CO.

Method 5: Systolic area

As illustrated in Fig.2-4, the area under the systole region, A_s, of the ABP waveform is proportional to the stroke volume [40]. Systolic area is proportional to the amount

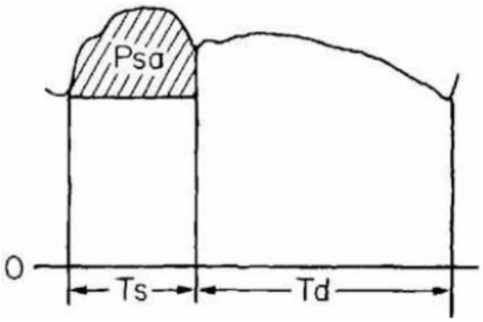

Figure 2-4: Systolic area estimation. Stroke volume is proportional to the area of the shaded region, $P_{sa} = A_s$. T_s and T_d represent the durations of the systolic and diastolic phases of the beat. Adapted from [23].

of blood drained from the peripheral vasculature; a longer systole or higher systolic pressures reflect a greater volume of blood the heart must eject. CO can be calculated as follows:

$$Q = k_5 \cdot A_s \cdot h$$

Method 6: Wesseling

Wesseling et al applied a correction factor to the systolic area method described above to take into account non-negligible contribution of fluctuations in ABP during systole [41]. Based on empirical studies and optimal linear regression analysis, impedance is corrected for to calculate CO:

$$Q = k_6 \cdot (163 + h - 0.48 \cdot P_m) \cdot A_s \cdot h$$

2.2 Evaluation Procedure

The cardiac output estimation and evaluation procedure is outlined in Fig.2-5. First, appropriate ABP data were extracted from records in the MIMIC II database, including 10-second trend files (T-files) that include a blood pressure SQI metric, fused heart rate from ABP and ECG, and a heart rate SQI metric generated by Li et al [25]. Then, appropriate blood pressure features were extracted and used to deter-

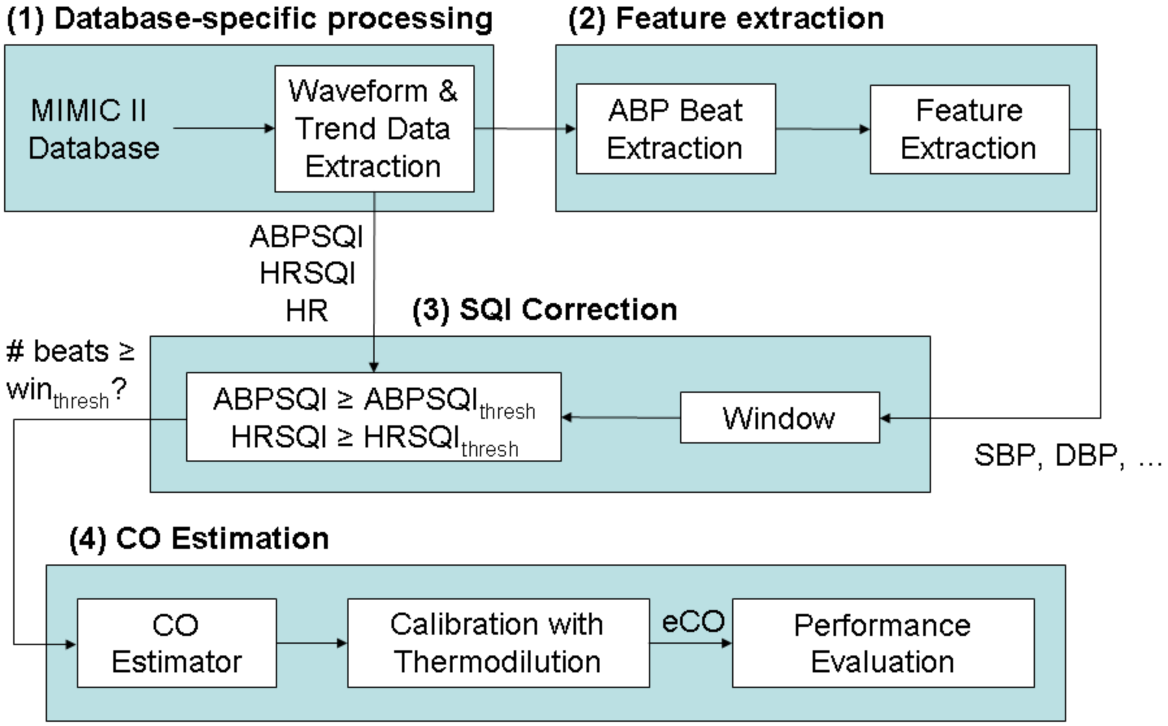
(1) Database-specific processing
MIMIC II Database
Waveform & Trend Data Extraction
(2) Feature extraction
ABP Beat Extraction
Feature Extraction
ABPSQI
HRSQI
HR
(3) SQI Correction
# beats ≥ win_{thresh}?
ABPSQI ≥ ABPSQI thresh
HRSQI ≥ HRSQI thresh
Window
SBP, DBP, ...
(4) CO Estimation
CO Estimator
Calibration with Thermodilution
eCO
Performance Evaluation

Figure 2-5: Cardiac output estimation and evaluation procedure. ABP and thermodilution data was first extracted from the MIMIC II database. Relevant features of the blood pressure waveform were extracted after segmenting the waveform into beats. The HR and ABP SQIs of each beat were compared for each window, and if the number of beats that satisfy SQI requirements was sufficient, a CO estimate was made for the window. After the estimated CO was computed for the entire record, CO was calibrated with thermodilution measurements, and the difference between the estimated CO and thermodilution was analyzed for performance evaluation.

mine whether each window contains sufficiently clean ABP and HR to generate a CO estimate. After CO estimates were generated for the record, the CO estimate was calibrated with thermodilution measurements. To evaluate the performance of the CO estimation procedure, estimated CO and measured thermodilution (TCO) were compared.

2.2.1 Database-specific processing

Relevant source code: wavex2.m, Tex.m, trendex2.m

From the MIMIC II Database, 121 records were identified with simultaneously

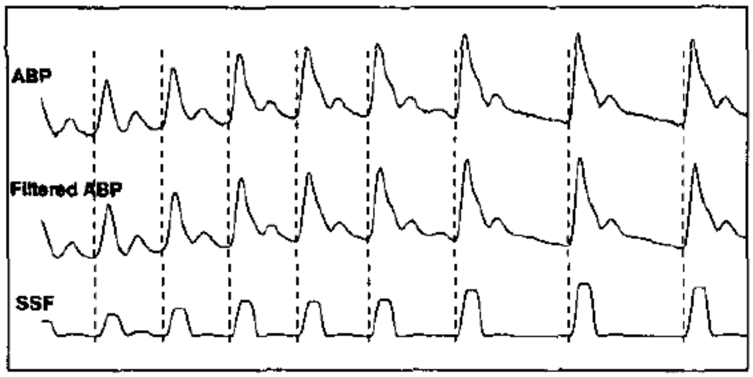

Figure 2-6: Beat extraction based on wabp. The SSF function amplifies the rising portion of each beat. Adapted from [43].

available ABP waveforms and TCO measurements. The ABP waveforms were measured from the femoral or radial arteries and sampled at 125 Hz with 8-bit quantization. TCO was available intermittently with a temporal resolution of 1 minute.

Trend files contain fused HR, HRSQI, and ABPSQI from previous analysis of heart rate estimation on MIMIC II data [25] at 10-second intervals. The derivation of the fused HR, HRSQI, and ABPSQI from ECG and ABP waveforms are described in Sections 1.5 and 1.6. From this point forward in this chapter, the fused HR developed will be referred to when mentioning heart rate.

2.2.2 Feature extraction

Relevant source code: wabp.m, abpfeature.m

Each ABP beat was extracted from the ABP waveform. A Matlab implementation of Zong et al's *wabp* algorithm [43] detects the onset of each beat using a slope sum function (SSF), which is a representation of the rising portions of each beat. An example is shown in Fig.2-6. A decision rule based on adaptive thresholds and searching strategies determines whether or not an onset is detected.

After the waveform was segmented into beats, important features for each beat were extracted. A list of features are included in Table 2.2. The feature extraction algorithm was based on previous work by Sun [37]. For each beat, the local maximum and minimum values correspond to systolic and diastolic blood pressures, respectively.

Pulse pressure is the difference between the two. Mean pressure is the time average of all pressure samples within the beat between adjacent onsets. The duration of the beat is the time difference between adjacent onsets. The time of the systolic portion of the beat is approximated as $T_s = 0.3\sqrt{\frac{60}{h}}$ [4], and pressure area during systole is calculated as the area during this time between the instantaneous blood pressure and diastolic pressure for that beat:

$$A_s = \int_{T_s} (P(t) - P_d)dt$$

Feature	Description	Units
P_s	Systolic blood pressure	mmHg
P_d	Diastolic blood pressure	mmHg
P_m	Mean blood pressure	mmHg
P_p	Pulse pressure ($P_s - P_d$)	mmHg
A_s	Pressure area during systole	mmHg · time
T	Duration of each beat	sec

Table 2.2: Extracted ABP Features.

2.2.3 SQI Correction

Relevant source code: find_goodbeats.m

A cardiac output estimate was produced for each window with reliable ABP and HR data. Each window was chosen as a minute preceding each TCO measurement, since the invasive nature of the thermodilution technique may change heart rate and blood pressure [31]. The length of the window is consistent with previous literature [37] [39] and was a trade-off between obtaining enough beats for an accurate representation of the hemodynamic condition prior to the measurement, and the nonstationarity of the patient's condition.

Signal quality indices were used as metrics to determine whether or not beats were sufficiently clean for estimation. HR, HRSQI, and ABPSQI from the T-files were linearly interpolated for each beat. For a beat to be considered "good", both heart rate and blood pressure had to pass SQI thresholds such that HRSQI $\geq$ HRSQI$_{\text{thresh}}$

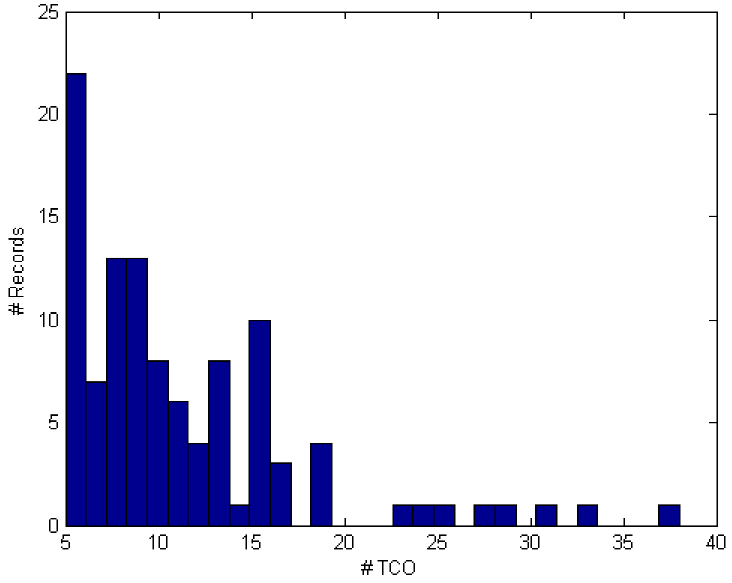

Figure 2-7: Distribution of records with thermodilution points taken during periods of clean SQI.

and ABPSQI $\geq$ ABPSQI$_{\text{thresh}}$. HRSQI$_{\text{thresh}}$ and ABPSQI$_{\text{thresh}}$ were varied, and their effects on CO estimator accuracy are discussed in Section 2.3. Likewise, the window size was also varied from 1 second to 7 minutes to examine how CO estimation accuracy changes.

Within each window preceding TCO measurement, a minimum number of clean beats were required to generate a CO estimate. This minimum was win$_{\text{thresh}}$, which was empirically set to 6 beats, or approximately 10% of the beats within a 1 minute window. The effects of varying this threshold are explored in Section 2.3. The distribution of records with thermodilution points taken during areas of clean SQI is shown in Fig.2-7, and the distribution of thermodilution values is in Fig.2-8.

2.2.4 CO Estimation

Relevant source code: est*A*_*B*.m, where A is the estimator number and B is the estimator name (such as est04_Herd.m)

If a window contained sufficient "good" beats, an uncalibrated cardiac output estimate was calculated, using the medians of the beat-by-beat HR and ABP features

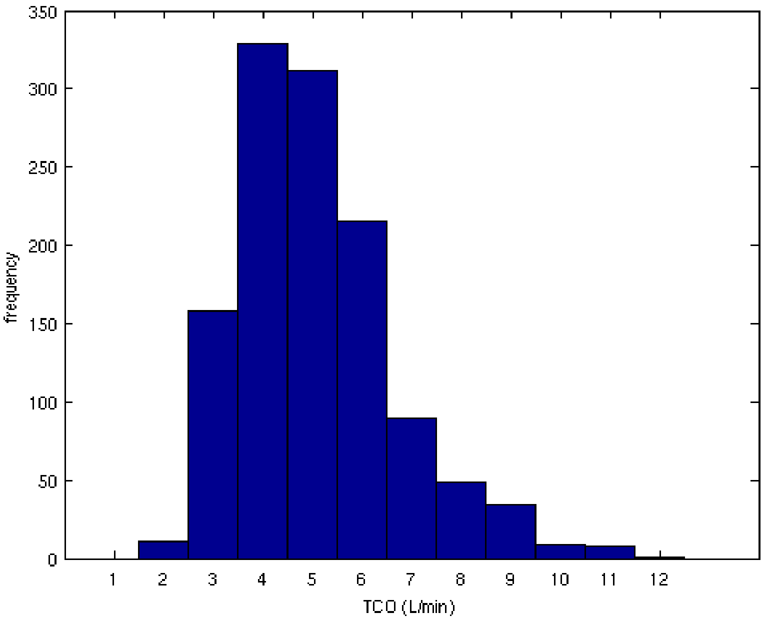

Figure 2-8: Thermodilution value distribution.

for beats passing SQI threshold tests. Beats that did not pass both the HR and ABP SQI threshold tests were not included in determining CO. The CO estimators explored were described in Section 2.1.

To account for arterial compliance and peripheral resistance factors, the CO estimate for a record needs to be calibrated with thermodilution measurements. An optimal calibration method was applied using all available thermodilution points for which CO estimates were produced, and the time between thermodilution measurements for the 121 cases considered in this study is shown in Fig.2-9. The calibration method is a least squares estimate between thermodilution and uncalibrated cardiac output. We now define x as the uncalibrated cardiac output (UCO), y as the calibrated estimated cardiac output (ECO), r as the thermodilution measurement (TCO), and k as the calibration constant. For a record containing n TCO measurements, the calibration constant was calculated as follows:

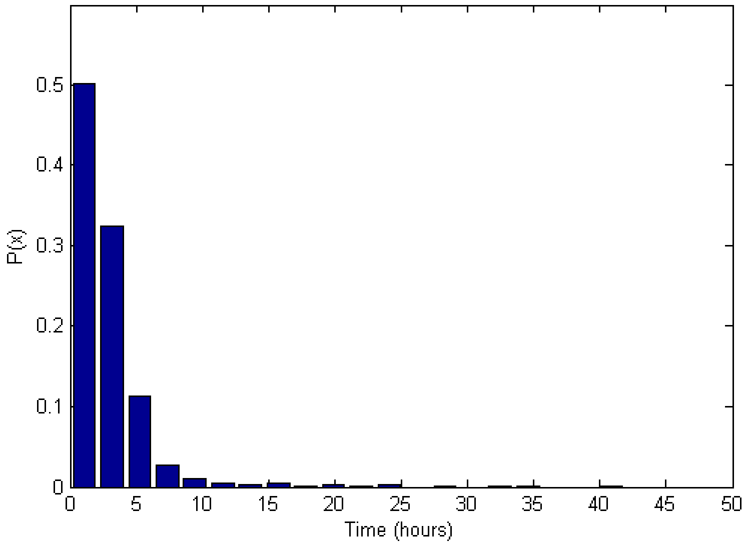

Figure 2-9: Time in hours between thermodilution measurements. Mean time is 3.1 hours, median time is 2.1 hours, and standard deviation is 8.8 hours.

$$\begin{aligned} \text{TCO} \quad & \mathbf{r} = [r_1 r_2 \cdots r_n]' \\ \text{UCO} \quad & \mathbf{x} = [x_1 x_2 \cdots x_n]' \\ \text{ECO} \quad & \mathbf{y} = k\mathbf{x} \end{aligned}$$

$$k = \frac{\mathbf{r}'\mathbf{x}}{\mathbf{x}'\mathbf{x}}$$

After calibration, the calibrated cardiac output was compared to thermodilution. An example is shown in Fig.2-10, where the beige plot is the estimated CO before SQI correction, green plot is estimated CO after SQI correction, the black triangles are the estimated CO within the window preceding each TCO point, and the red circles represent TCO points with error bars of 20%.

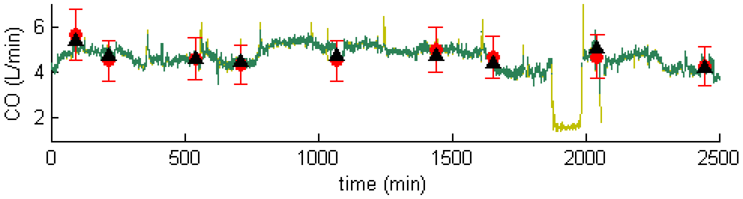

Figure 2-10: Case ID a40006 without SQI correction using the Liljestrand CO estimation method. The beige plot is the estimated CO before SQI correction, green plot is the estimated CO after SQI correction, the black triangles are the medians of the good beats within the window preceding the TCO point, and the red circles represent TCO points with error bars of 20%.

2.3 Results

2.3.1 Error Criteria

CO estimates were compared to thermodilution measurements to determine the accuracy of the estimates. A root mean square normalized error (RMSNE) criterion was used, consistent with other CO evaluation studies [32]. Errors were calculated when at least 5 TCO were made during areas of good SQI. For each subject s with $\mathrm{n_s}$ comparable thermodilution points, the RMSNE for the ECO for the subject, $\mathrm{RMSNE_s}$, is:

$$\mathrm{RMSNE_s} = \sqrt{\frac{1}{\mathrm{n_s}}\sum_{\mathrm{i}=1}^{\mathrm{n_s}}\left(\frac{100(\mathrm{TCO_i}-\mathrm{ECO_i})}{\mathrm{TCO_i}}\right)^2},\quad 1 \le \mathrm{s} \le \mathrm{S}$$

where S is 121, the total number of records.

To evaluate the accuracy of the estimates across all subjects, the $\mathrm{RMSNE_s}$s were averaged to obtain an *average* RMSNE, $\mathrm{RMSNE_a}$. The data set has a total of N comparable thermodilution points across all records:

$$\mathrm{N} = \sum_{\mathrm{s}=1}^{\mathrm{S}} \mathrm{n_s}$$

For all S subjects, $\mathrm{RMSNE_a}$ is:

$$\mathrm{RMSNE_a} = \frac{1}{\mathrm{N}} \sum_{\mathrm{s}=1}^{\mathrm{S}} \mathrm{RMSNE_s}$$

However, $\mathrm{RMSNE_a}$ can be skewed in a particular direction if $\mathrm{n_s}$ for each subject is not taken into account, particularly if a subject has a greater $\mathrm{n_s}$ and/or is more error-prone. To account for these variations, a *gross* RMSNE measure, $\mathrm{RMSNE_g}$, is also used. This error metric is a weighted mean of the individual $\mathrm{RMSNE_s}$ according to $\mathrm{n_s}$. The gross RMSNE, $\mathrm{RMSNE_g}$, is:

$$\mathrm{RMSNE_g} = \sqrt{\frac{1}{\mathrm{N}} \sum_{\mathrm{s}=1}^{\mathrm{S}} \mathrm{n_s}(\mathrm{RMSNE_s^2})}$$

$\mathrm{RMSNE_s}$, $\mathrm{RMSNE_a}$, and $\mathrm{RMSNE_g}$ are in units of percent. Gross RMSNE essentially treats each TCO point and its associated estimated CO, rather than each record, as a data point. We therefore use the terminology *average* for errors across cases, and *gross* for errors across individual TCO measurements. If each difference between TCO and ECO in RMSNE is not normalized by TCO, a root mean square error (RMSE) can be obtained in liters per minute as follows:

$$\mathrm{RMSE_s} = \sqrt{\frac{1}{\mathrm{n_s}} \sum_{\mathrm{i}=1}^{\mathrm{n_s}} (\mathrm{TCO_i} - \mathrm{ECO_i})^2}$$

Analogous average and gross RMSEs can be calculated for each data set. However, results using both RMSNE and RMSE generally indicate the same trends and are therefore not reported for all data sets in this thesis.

2.3.2 Estimator Comparison

Using a window of 1 minute and HRSQI threshold of 50, the various CO estimators were compared at different ABPSQI thresholds. Fig.2-11 illustrates the results at each SQI level. The Liljestrand estimator yields the lowest errors at all ABPSQI thresholds, while the Herd estimator generally yields the highest errors, which is

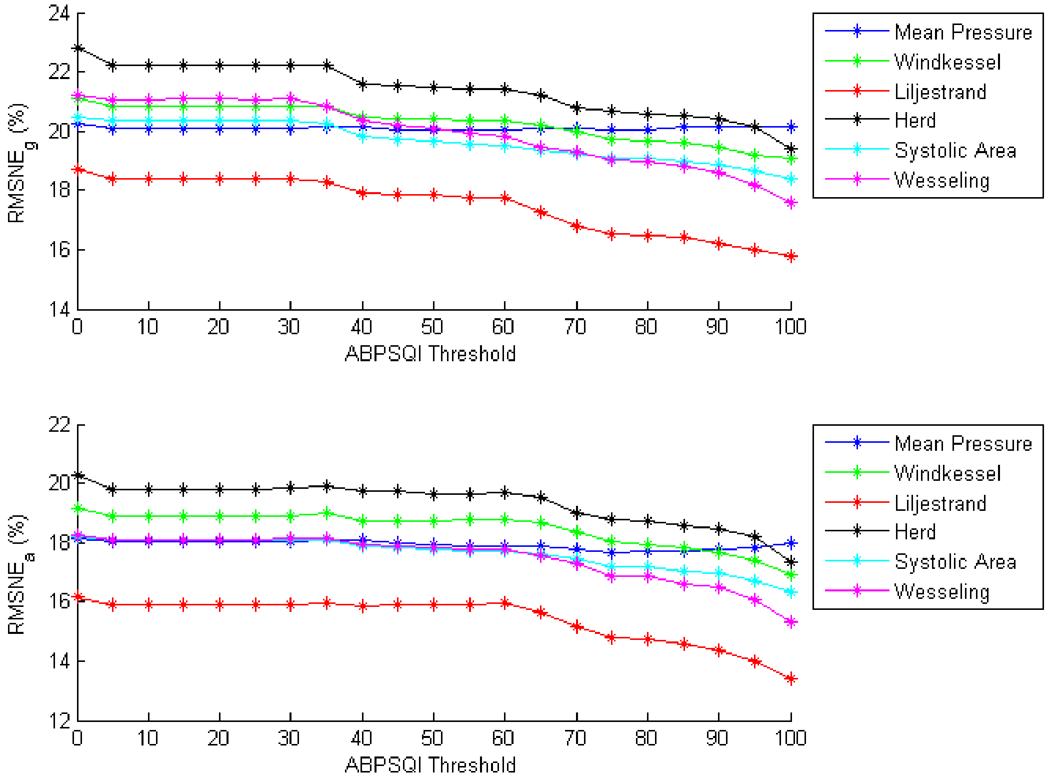

Figure 2-11: Estimator comparison at different ABPSQI thresholds.

consistent with previous CO estimation studies on MIMIC II data [37]. The mean pressure method changes little with varying ABPSQI thresholds, and considering its simplicity, yields lower errors at low ABPSQI thresholds than most estimators. The Liljestrand and Wesseling estimators are the most sensitive to ABP signal quality, with lower errors at higher ABPSQI thresholds. The Windkessel and systolic area methods show higher accuracy as ABPSQI threshold is increased as well.

2.3.3 HRSQI and ABPSQI Thresholds

Using the Liljestrand method and a window size of 1 minute, the effects of varying both ABPSQI and HRSQI thresholds were evaluated. Fig.2-12 illustrates the effect of requiring minimum ABPSQI and HRSQI values for a particular subject, in this case using an ABPSQI threshold of 90 and HRSQI threshold of 50. Sharp spikes in the CO estimate are removed or reduced with signal quality thresholding, as these are most likely due to artifacts in the data recordings. Furthermore, sudden drops or rises are mitigated, such as in the section at 1900 to 2000 minutes. Another example is shown in Fig.2-13, where artifacts at approximately 850 minutes and 1220 minutes are reduced or eliminated.

Fig.2-14 illustrates the results using the RMSNE error criteria, while Fig.2-15 illustrates the results using the RMSE error criteria. As signal quality thresholds become more stringent, error decreases. By increasing either the HRSQI or ABPSQI threshold, a lower error for both the gross and average RMSNE is achieved. Beats that have questionable reliability are excluded from estimation, so the remaining beats should more accurately reflect the underlying physiological condition. However, as SQI requirements become more stringent, fewer thermodilution points are used in calculating RMSNE, since fewer windows pass the SQI requirements and fewer CO estimates are generated. The number of TCO-ECO pairs available for comparison are shown in Fig.2-16.

The effect of ABPSQI threshold is more evident when HRSQI threshold is lower. For ABPSQI thresholds greater than 70, the only beats that pass the threshold test are beats designated as good by jSQI *and* wSQI. Error decreased up to 14% by varying HRSQI, and as ABPSQI was increased, a similar decrease in error was also observed. As with many real-world solutions to engineering problems, a tradeoff occurs between accuracy and availability of CO estimates, since increased stringency excludes more data from participating in the estimation process. However, even at HRSQI$\geq$ 90 and ABPSQI$\geq$ 90, more than 80% of the data is still available to generate CO estimates. At HRSQI and ABPSQI thresholds of 90, the lowest gross RMSNE was found to be 15.4% (or 0.74 L/min) and average RMSNE was 13.7% (0.71 L/min), with 1216 comparison points from 109 records.

2.3.4 Window size

Window sizes of 1 minute to 7 minutes preceding the thermodilution measurements were explored using the Liljestrand method and a HRSQI threshold of 50. Fig.2-17

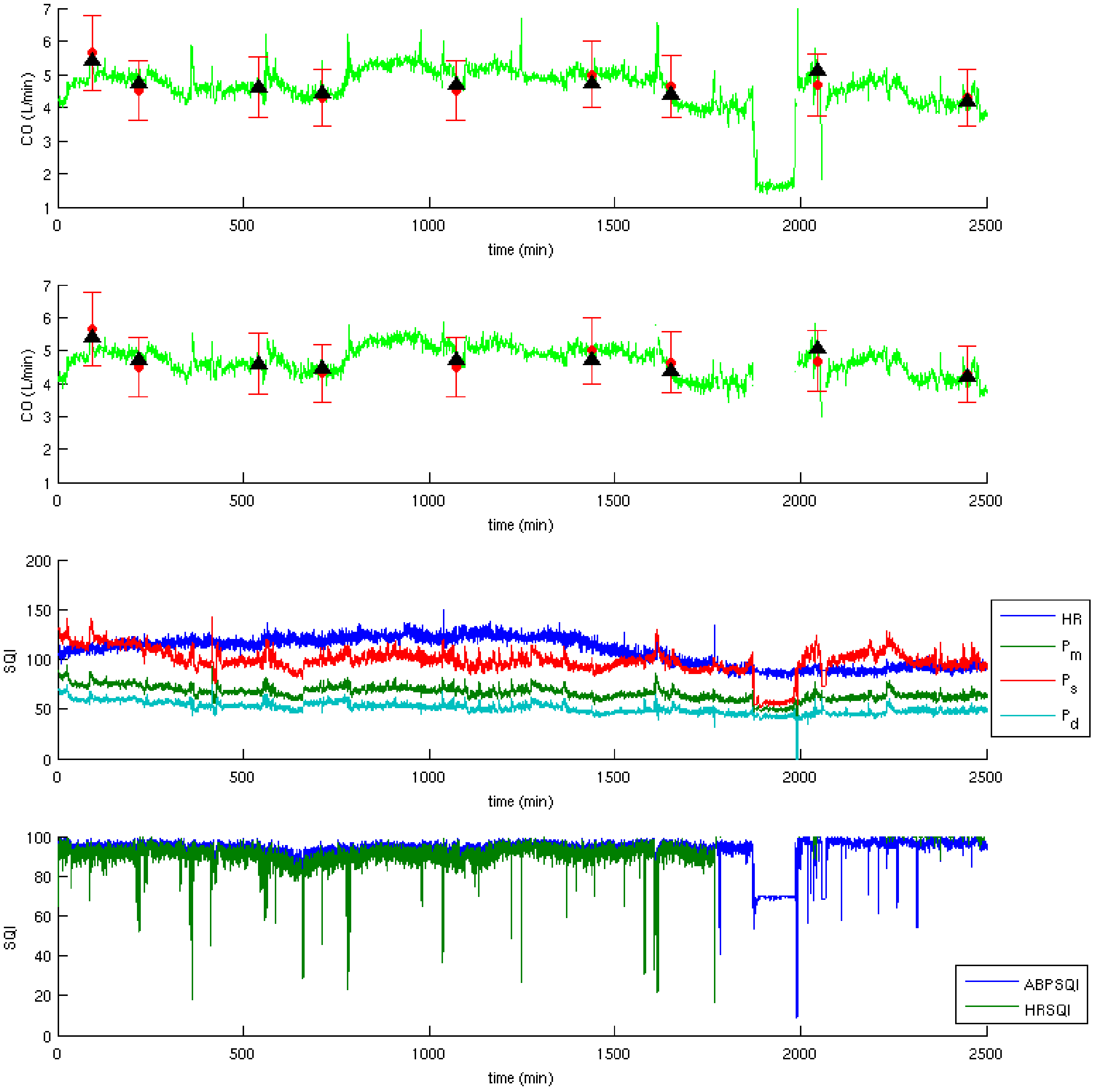

Figure 2-12: Case ID a40006 without SQI correction (a) and with SQI correction (b) using the Liljestrand CO estimation method. The green plot is the estimated CO, the black triangles are the median estimated CO of the good beats within the window preceding the TCO point, and the red circles represent TCO points with error bars of 20%. Blood pressure and fused heart rate are shown in (c), and their corresponding signal qualities are shown in (d).

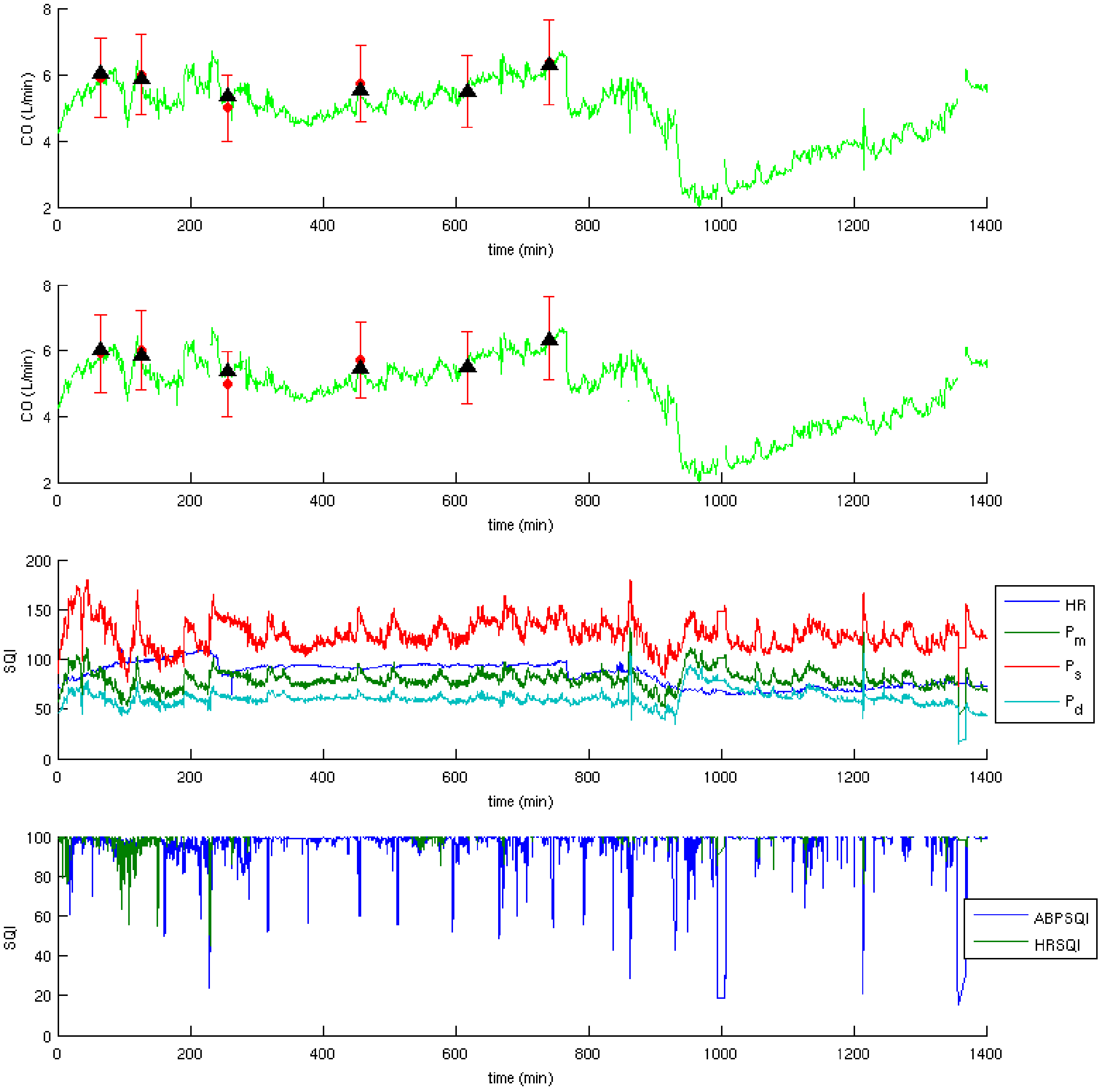

Figure 2-13: Case ID a40075 without SQI correction (a) and with SQI correction (b) using the Liljestrand CO estimation method. The green plot is the estimated CO, the black triangles are the medians of the good beats within the window preceding the TCO point, and the red circles represent TCO points with error bars of 20%. Blood pressure and fused heart rate are shown in (c), and their corresponding signal qualities are shown in (d).

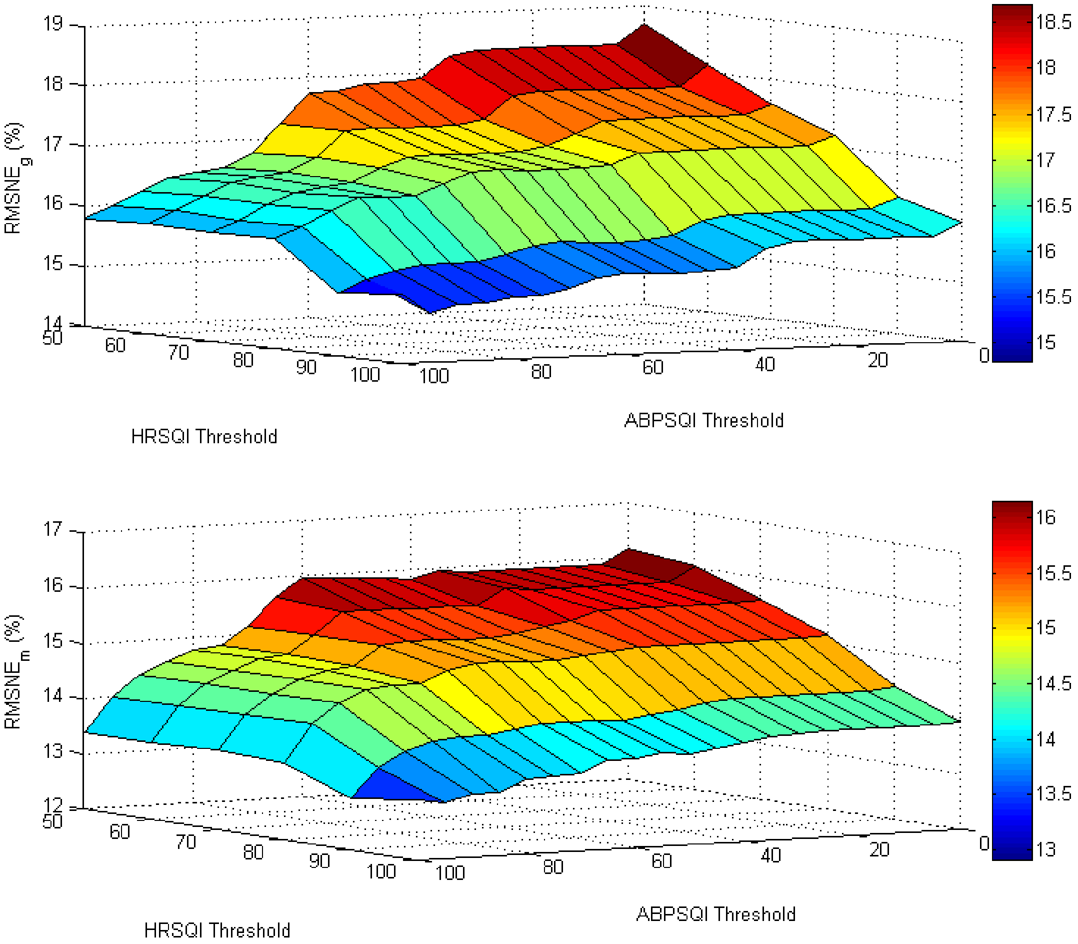

Figure 2-14: CO estimation errors at different ABPSQI and HRSQI thresholds using the RMSNE error criteria for the Liljestrand method.

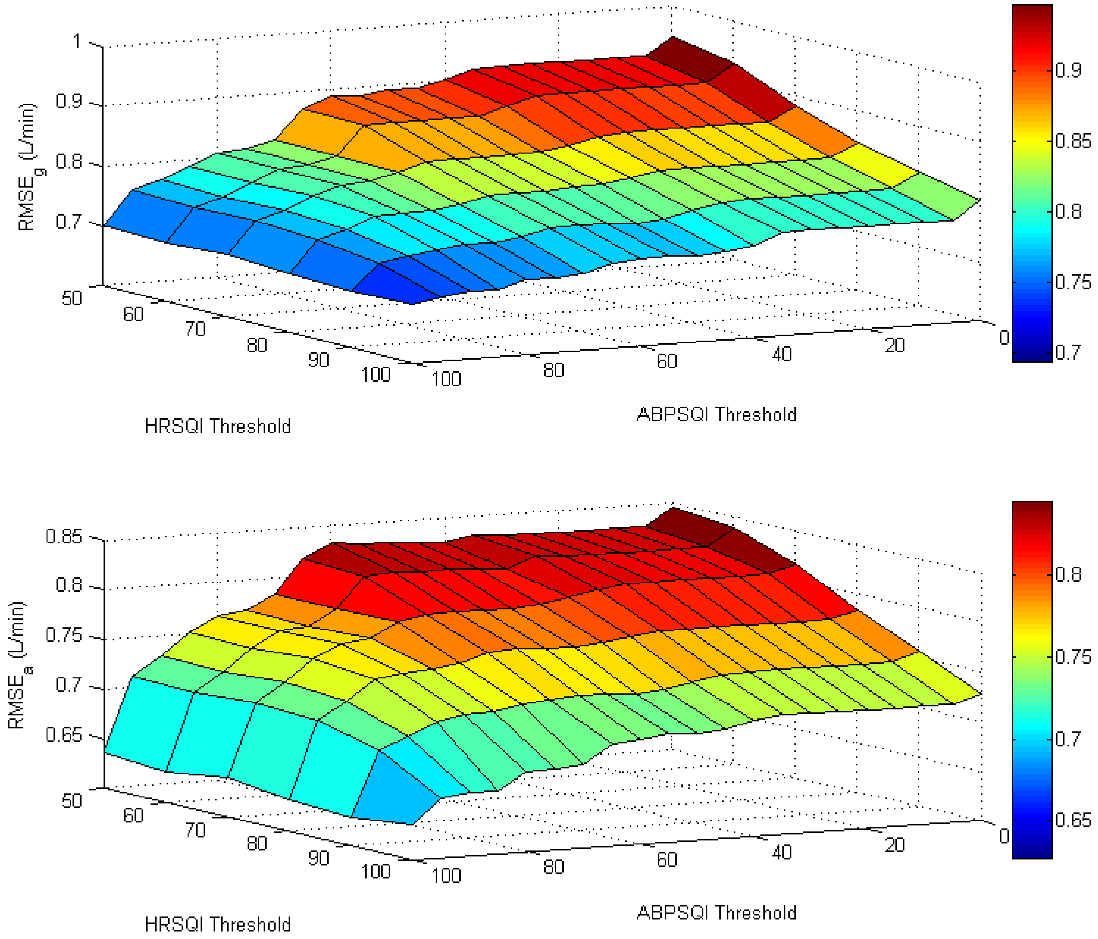

Figure 2-15: CO estimation errors at different ABPSQI and HRSQI thresholds using the RMSE error criteria for the Liljestrand method.

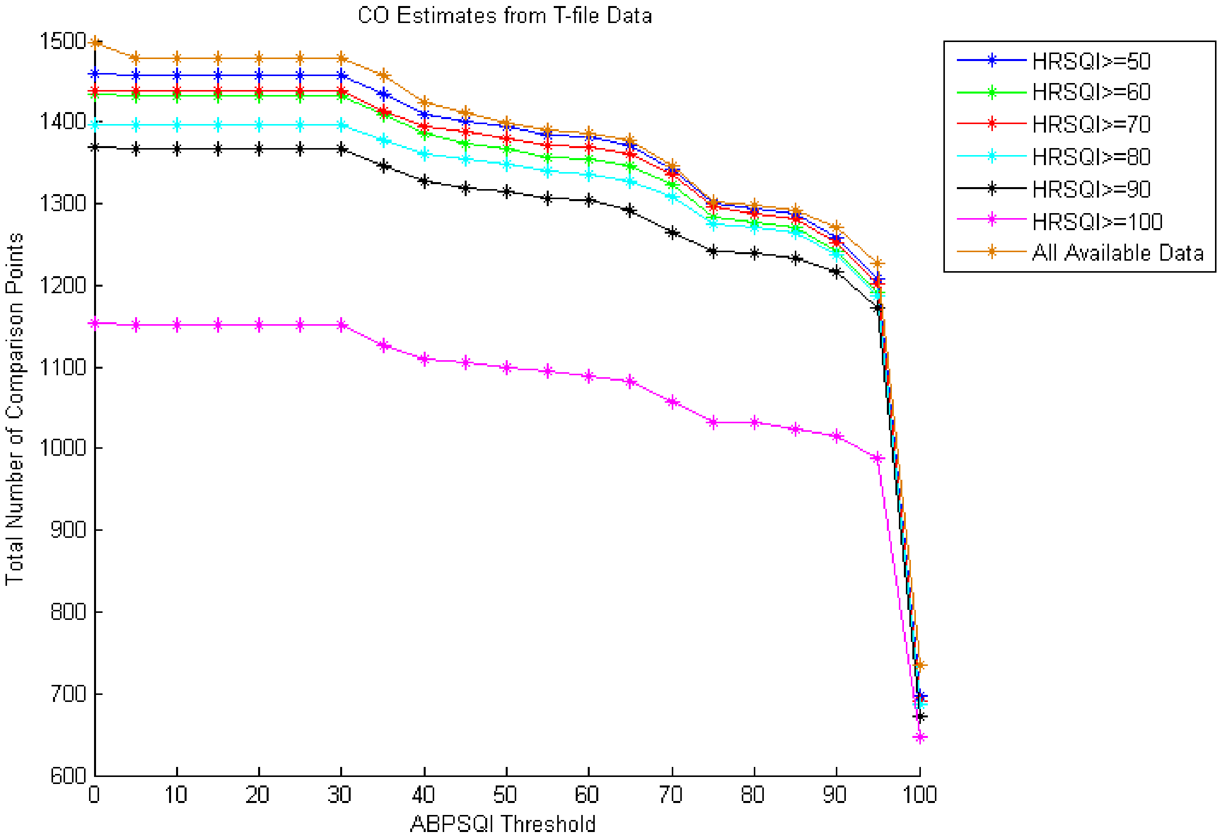

Figure 2-16: Data availability at different ABPSQI and HRSQI thresholds.

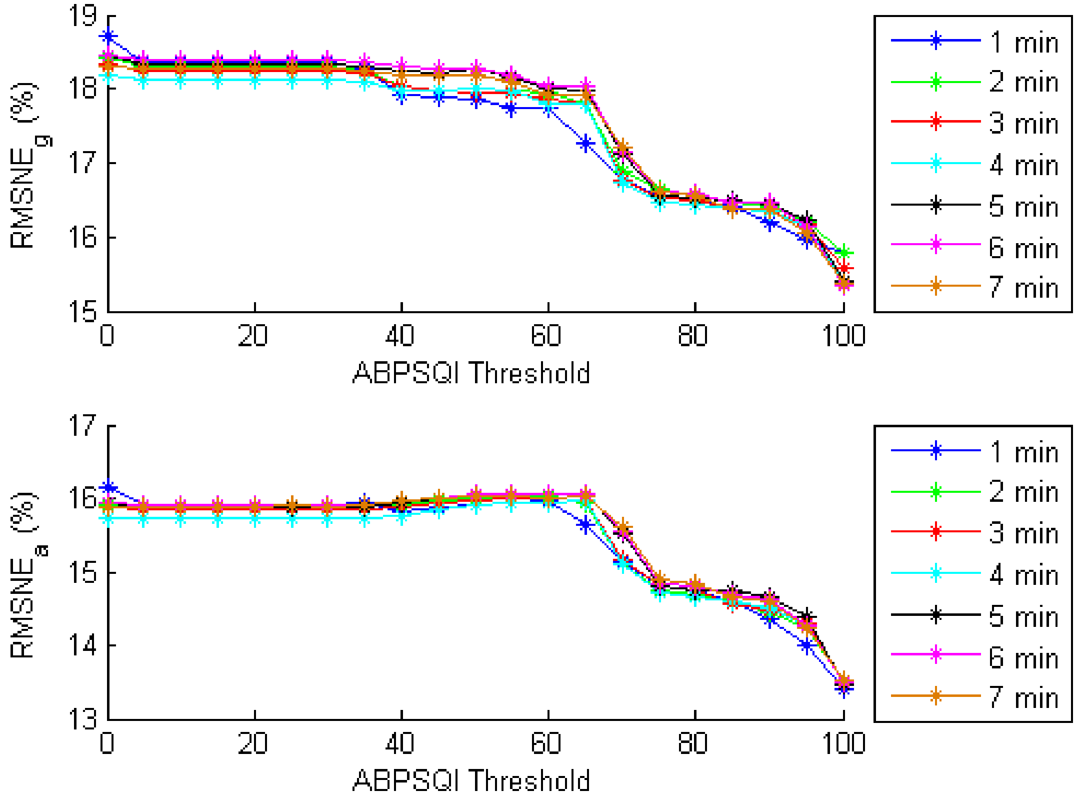

Figure 2-17: Effect of window size and ABPSQI threshold on CO estimation error using the Liljestrand method.

shows that window size has little influence on error, although the 1 minute window provides estimates with the lowest error. This is logical considering thermodilution measurements are made with 1-minute resolutions, and this window size is also preferable for clinical use since CO estimates can be generated more frequently.

2.3.5 Ordering of mean and median averaging

Instead of providing the CO estimator with the median of the good beats within the window, one could presumably also use the mean of these beats as inputs to the estimator. Also, rather than performing mean or median operations prior to CO estimation, beat-by-beat CO estimates could be generated from the good beats. The CO estimate for the window would then be the mean or median of these beat by beat CO estimates. These variations in the ordering of performing the mean or

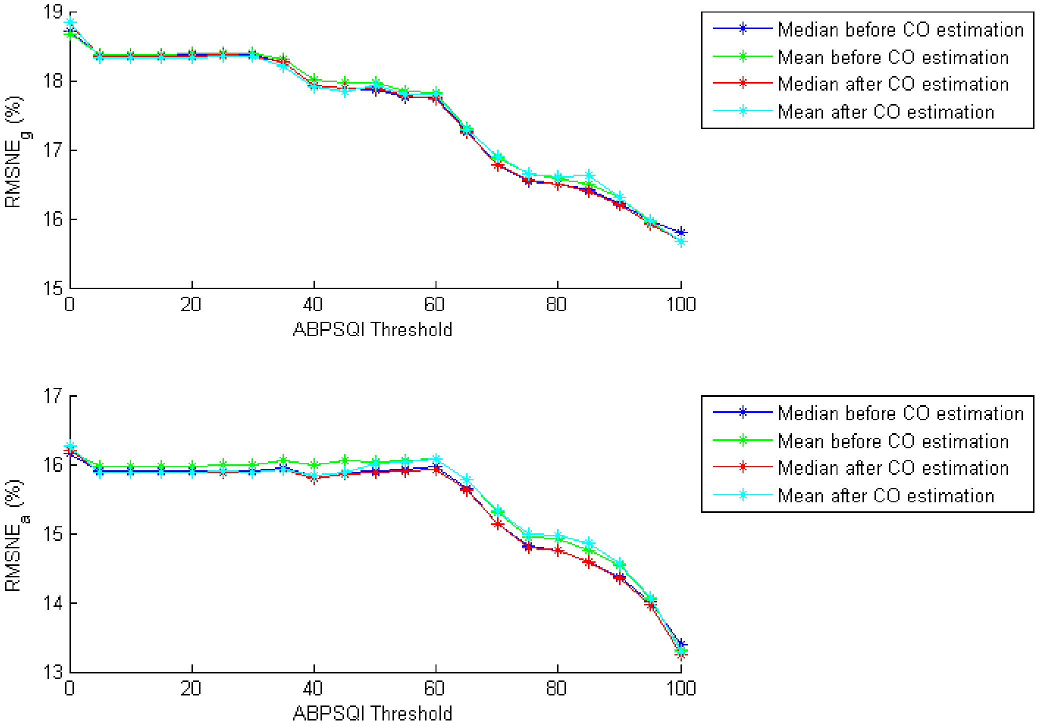

Figure 2-18: Effect of performing mean or median operation before and after CO estimation using the Liljestrand method.

median operations were evaluated for a 1 minute window with HRSQI threshold of 50 using the Liljestrand method, and results are shown in Fig.2-18. As shown, the order of performing mean or median operations in CO estimation has little effect on the accuracy of estimated CO, and hence we chose to use median before CO estimation, since mean or median before CO estimation yields marginally lower errors.

2.3.6 Window threshold

The minimum number of beats needed that pass the SQI requirements in each window to generate a CO estimate, $\text{win}_{\text{thresh}}$, was set to be 6 beats, or approximately 10% of a 1 minute window. Using the Liljestrand method with HRSQI of 50 and 1 minute windows, the error for varying $\text{win}_{\text{thresh}}$ was computed and shown in Fig.2-19. Generally, error decreases with increasing minimum number of beats, and the most significant reduction in error is between 6 and 15 beats. After a minimum of 15

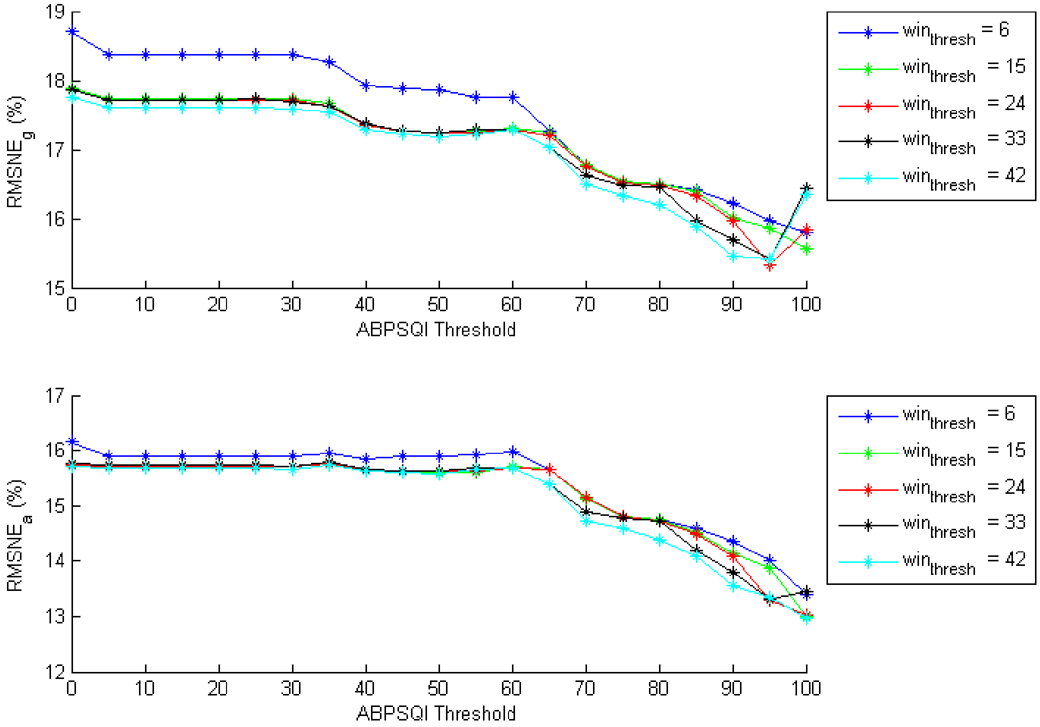

Figure 2-19: Effect of minimum number of good beats in a window.

beats, increasing the minimum number of beats further has little effect on error. At these higher values of $\text{win}_{\text{thresh}}$, increasing ABPSQI threshold does not monotonically decrease the error, most noticeably at ABPSQI threshold of 100. This effect may be due to the fact that fewer segments preceding thermodilution measurements are available that meet the minimum number of beats to generate a CO estimate.

2.3.7 Analysis at recommended parameters

Out of the parameters explored, the most important factors in generating accurate CO estimates were ABPSQI threshold, HRSQI threshold, and estimator method. For all signal quality thresholds investigated, the Liljestrand method yielded the lowest error. We recommend using the Liljestrand estimator with 1-minute windows, making estimates when 6 or more beats have HRSQIs and ABPSQIs greater than 90. Using these parameters, RMSNE_g is 15.4% and RMSNE_a is 13.7%, while RMSE_g

is 0.74 L/min and $\mathrm{RMSE_s}$ is 0.71 L/min. In comparison with the gold standard thermodilution method, which has an error of 10-20% (0.5-1 L/min for a standard 5 L/min CO), the accuracy of CO estimation using ABP falls in the same range. Note that since windows of 1 minute are good estimators, we are free to ignore low quality sections, such as throwing away a 1-minute window every 4 minutes to generate a CO estimate for every 5 minutes.

At these recommended SQI thresholds at 1 minute windows, statistics for the calibration constant k_i of each estimator is shown in Table 2.3, where i is an index from 1 through 6 corresponding to each estimator. The histogram of k_is obtained is shown for each estimator in Fig.2-20 through Fig.2-25. Calibration constants appear to follow a long-tailed Gaussian distribution. A linear regression of TCO and k_i are shown for each estimator in Fig.2-26 through Fig.2-31. As shown, k_i increases as TCO increases for each estimator i, and the R^2 values of the regressions for each estimator are listed in Table 2.3. A possible explanation for the positive correlation between k_i and TCO could be from nonlinear behaviors at high pressures. As blood vessels become stiffer at large pressures, k_i increases due to changes in compliance. Because TCO measurements are typically within a limited range for each record, the global calibration method, which employs a least squares estimate between TCO and uncalibrated CO, may yield higher k_is at higher pressures and lower k_is at lower pressures.

i	Estimator	μ_{k_i}	$\tilde{\mu}_{k_i}$	σ_{k_i}	R^2
1	Mean arterial pressure	0.072	0.070	0.026	0.60
2	Windkessel	0.0010	0.00097	0.00036	0.49
3	Liljestrand nonlinear compliance	0.18	0.17	0.059	0.54
4	Herd	0.0033	0.0032	0.0012	0.46
5	Systolic area	0.0063	0.0060	0.0023	0.50
6	Wesseling	0.000030	0.000028	0.000011	0.50

Table 2.3: Statistics for calibration constants k_i for different estimators at recommended SQI thresholds to remove noisy data. μ_k is mean of k, $\tilde{\mu}_k$ is median of k, σ_k is standard deviation of k.

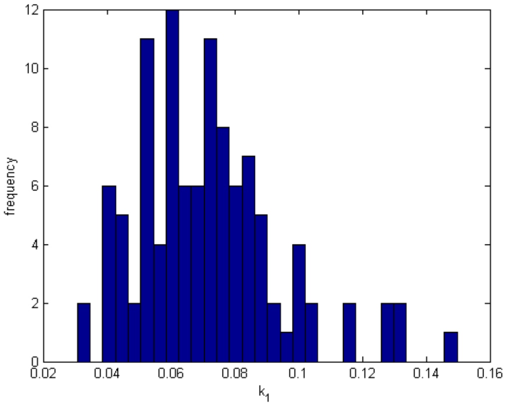

Figure 2-20: Calibration constant histogram for Mean Arterial Pressure.

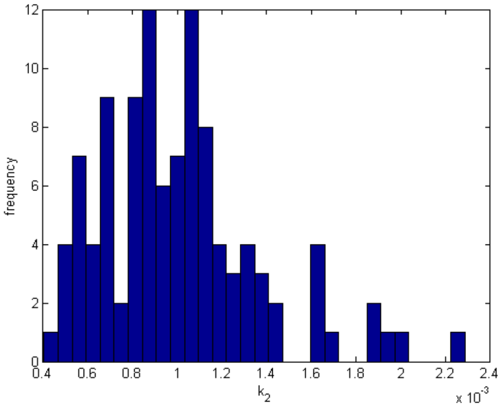

Figure 2-21: Calibration constant histogram for Windkessel.

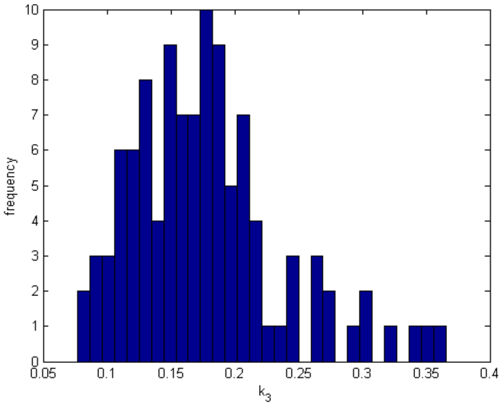

Figure 2-22: Calibration constant histogram for Liljestrand nonlinear compliance.

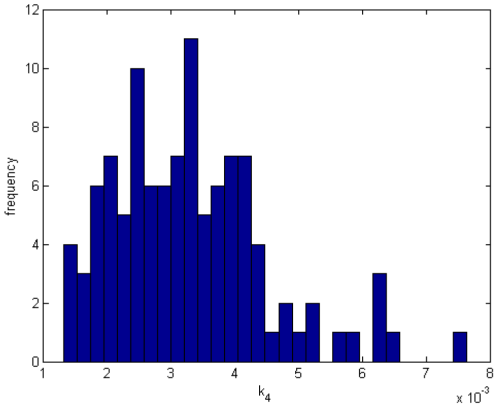

Figure 2-23: Calibration constant histogram for Herd.

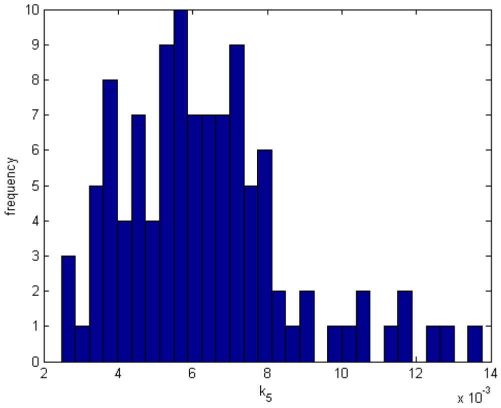

Figure 2-24: Calibration constant histogram for Systolic area.

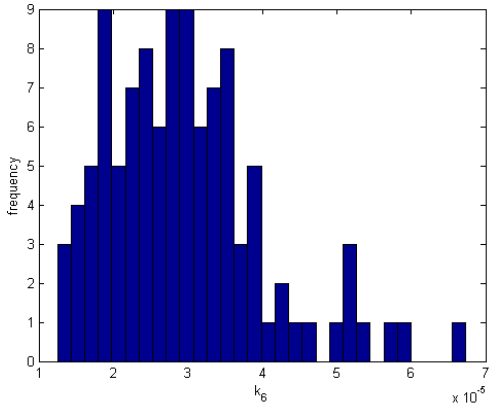

Figure 2-25: Calibration constant histogram for Wesseling.

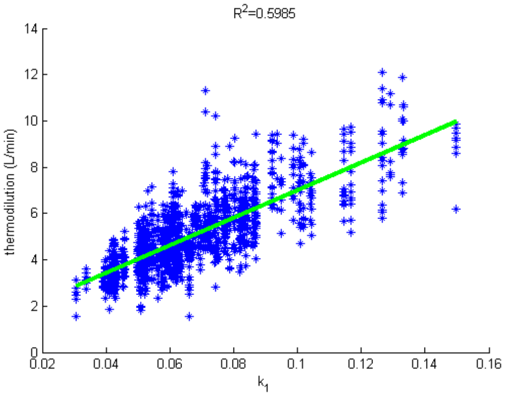

Figure 2-26: Calibration constant linear regression with thermodilution for Mean Arterial Pressure.

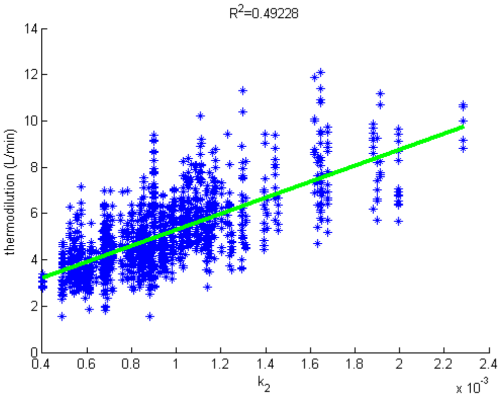

Figure 2-27: Calibration constant linear regression with thermodilution for Windkessel.

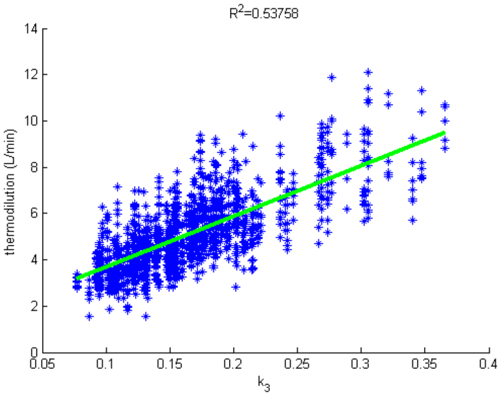

Figure 2-28: Calibration constant linear regression with thermodilution for Liljestrand nonlinear compliance.

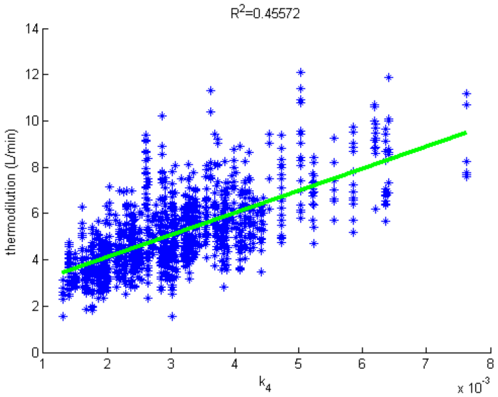

Figure 2-29: Calibration constant linear regression with thermodilution for Herd.

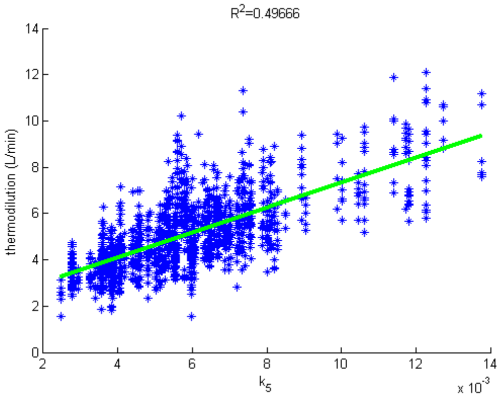

Figure 2-30: Calibration constant linear regression with thermodilution for Systolic area.

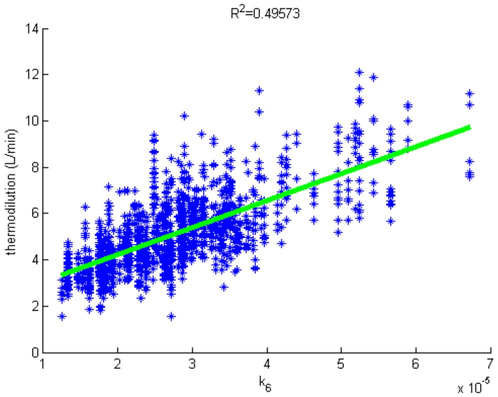

Figure 2-31: Calibration constant linear regression with thermodilution for Wesseling.

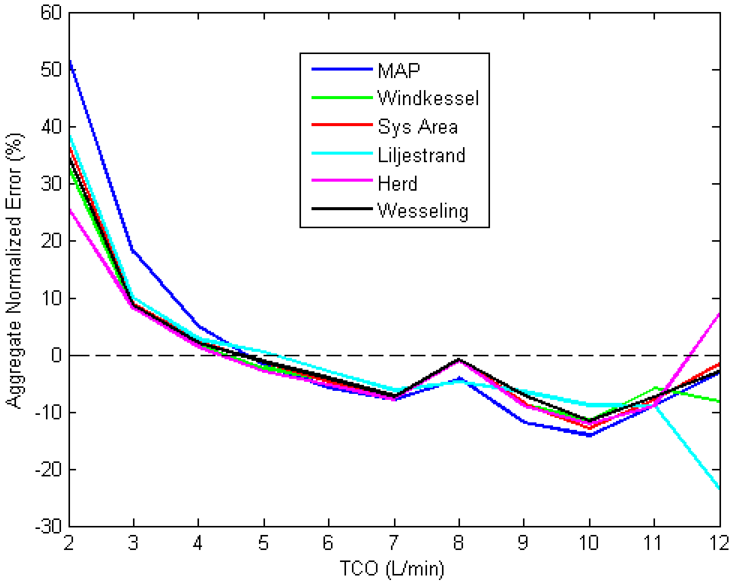

Figure 2-32: Normalized error, $\left(\frac{\text{ECO}-\text{TCO}}{\text{TCO}}\right)$ (100%), at a range of thermodilution values.

CO estimation errors were analyzed at different CO estimate levels to determine whether or not estimates were systematically overestimating or underestimating CO at different physiological operating points. As shown in Fig.2-32 and Fig.2-33, for both normalized and absolute errors, all estimators tended to overestimate at COs under 4 L/min and underestimate at COs greater than 4 L/min, indicating a more constrained range of estimated COs compared to that obtained from TCO. Note that most of the TCO values were clustered from 3 L/min to 8 L/min, as seen in Fig.2-8, and therefore errors beyond this range have less statistical significance. Out of the estimators, the MAP estimator was the most likely to overestimate at low COs and underestimate at high COs, while the Herd estimator was least likely to overestimate at low COs. The Liljestrand estimator performed only adequately in avoiding overestimation at low COs and but was generally less likely to underestimate under at high COs.

Estimation error, both RMSNE and RMSE, were examined to determine whether estimators were inclined to have high errors over a range of heart rates, mean ABPs, and pulse pressure. The results for relating error with heart rate are shown in Fig.2-34 and Fig.2-35, with P_m in Fig.2-36 and Fig.2-37, and with P_p in Fig.2-38 and

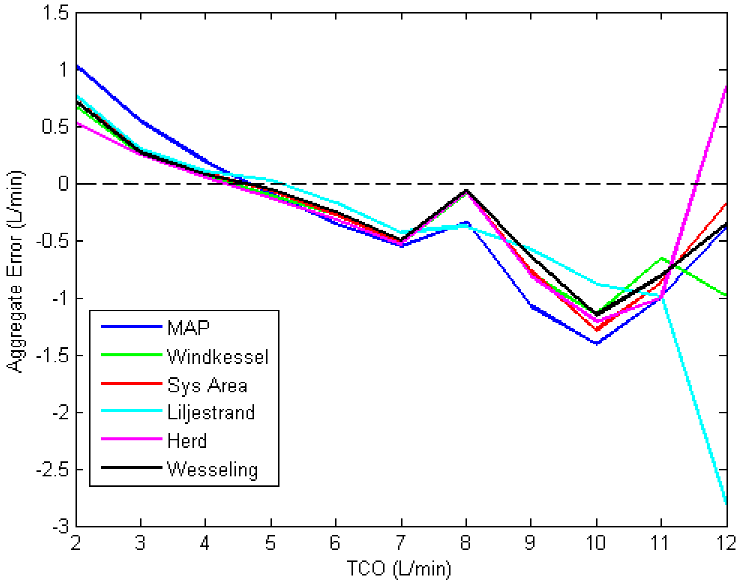

Figure 2-33: Absolute error, ECO − TCO, at a range of thermodilution values.

Fig.2-39. For various heart rates, mean ABPs, and pulse pressures, the Liljestrand estimator generally yielded the lowest errors. For a range of mean ABPs, Herd and MAP estimators yielded the highest errors, while for a range of pulse pressures, MAP, Windkessel, and Herd were generally the estimators with the highest errors. Note that at extremely low or high values of each of these parameters, fewer points are available to draw conclusions from and are therefore less statistically significant.

2.4 Discussion

CO estimators were evaluated using HRSQI and ABPSQI to eliminate ABP and HR of poor quality. At all SQI thresholds explored, the Liljestrand method yielded the lowest error in the sense of using the RMSNE and RMSE gross and average errors. CO estimates made at 1-minute intervals were recommended using HRSQI and ABPSQI thresholds of 90. Window size had little effect, while increasing $\text{win}_{\text{thresh}}$ had limited utility in generating CO estimates with higher accuracy. The difference between performing a mean or median operation in the estimation process also made little change in the accuracy of the CO estimates. At recommended thresholds, the

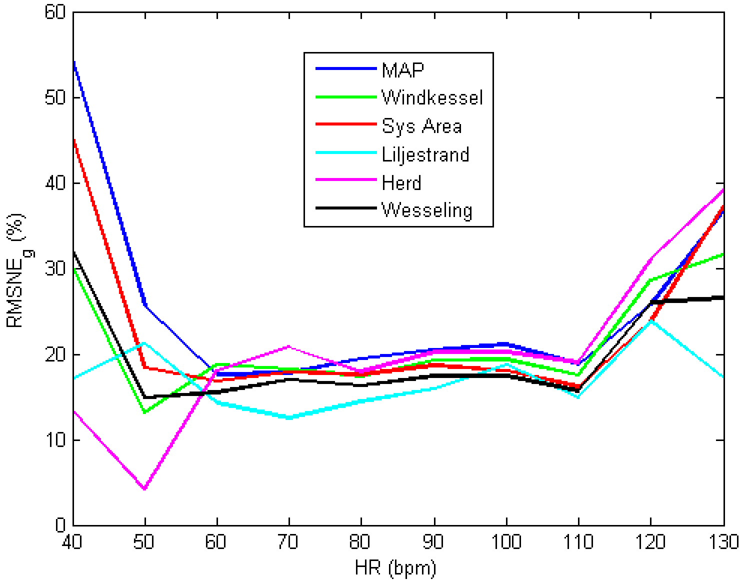

Figure 2-34: RMSNE as a function of heart rate.

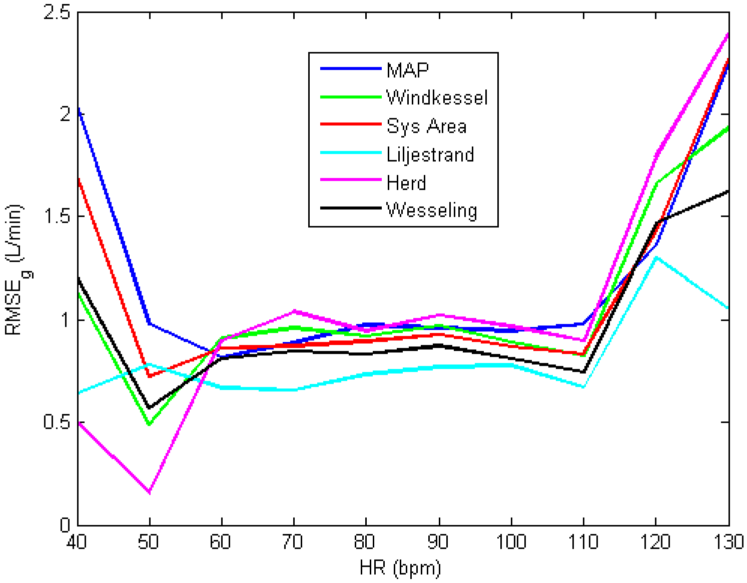

Figure 2-35: RMSE as a function of heart rate.

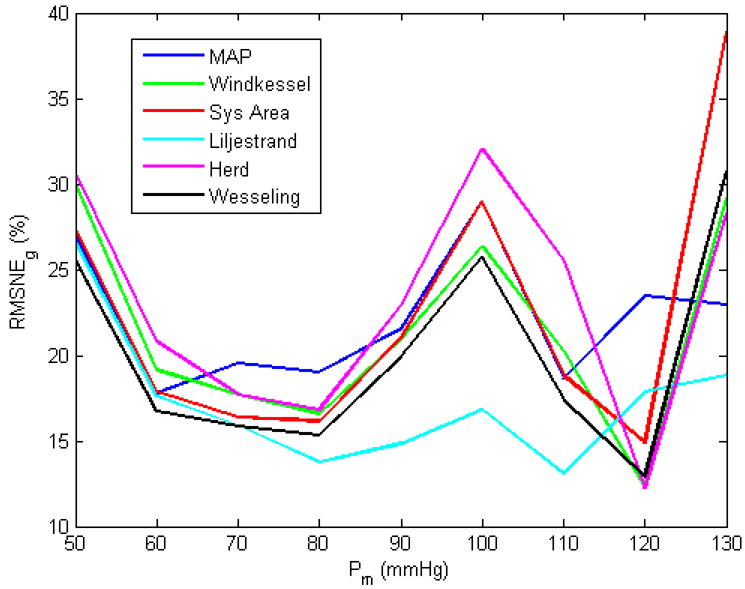

Figure 2-36: RMSNE as a function of mean ABP.

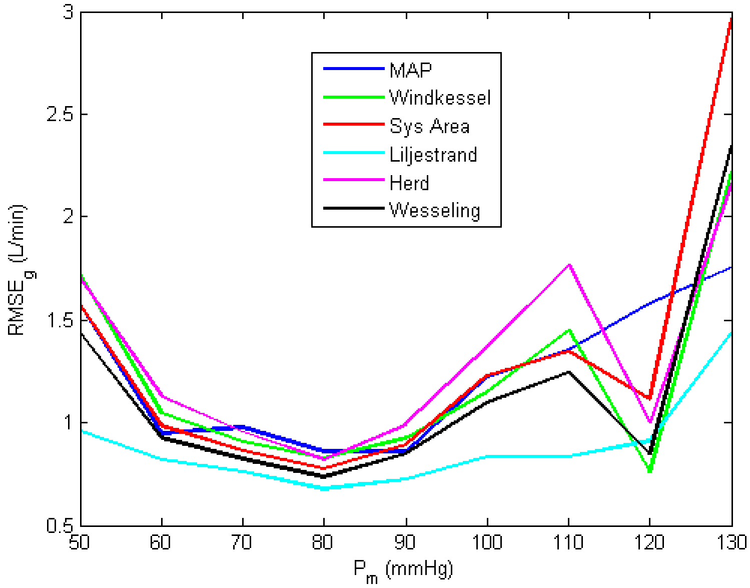

Figure 2-37: RMSE as a function of mean ABP.

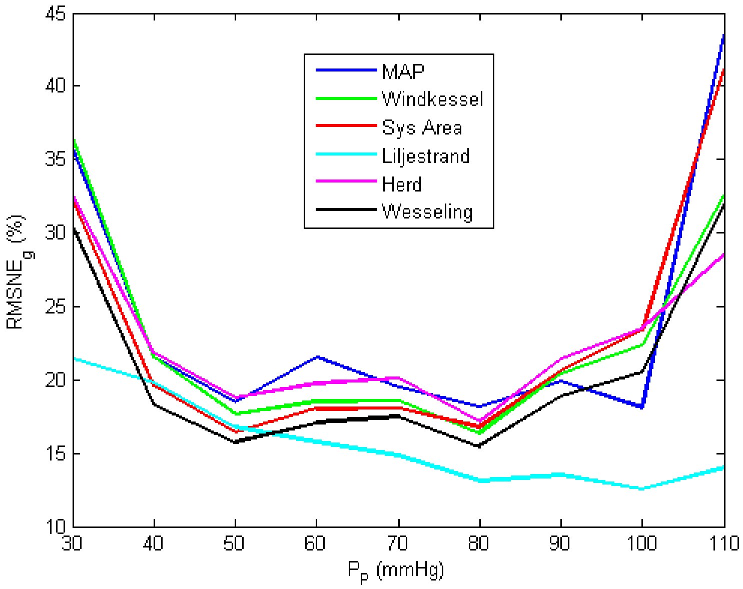

Figure 2-38: RMSNE as a function of pulse pressure.

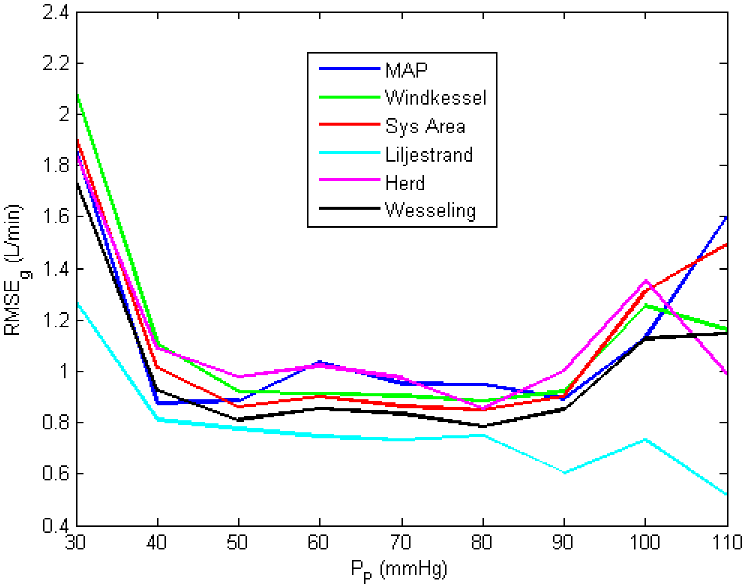

Figure 2-39: RMSE as a function of pulse pressure.

Liljestrand estimator generally outperformed all other estimators examined, with the least error over a range of heart rates, mean blood pressures, and pulse pressures and having the least tendency to underestimate at high COs and overestimate at low COs.

The results in this chapter are comparable to CO estimators developed elsewhere. At HRSQI and ABPSQI thresholds at 90, the Liljestrand estimator yielded a 15.4% gross RMSNE and 13.7% average RMSNE. Parlikar [32] achieved a gross RMSNE of 14.8% on a set of 12 human patients from the MIMIC I database, a previous database of clinical information collected for the Beth Israel Deaconess Medical Center.

Based on the groundwork set by these results, additional research was performed in collaboration with Abdala et al [1], using a linear combination (LC) of the 6 estimators examined in this thesis. The rationale for this approach was to see if a weighted "voting" of each estimator could correct for the underestimating and overestimating of COs at high and low CO levels, respectively. An online calibration method was used rather than the global calibration technique employed so far, and the data was divided to perform boostrap testing [9]. A 5% holdout was performed, and the mean square error (MSE) was evaluated 20 times, holding out a different 5% of data each time. Mean and standard deviations were calculated over these 20 sets.

The LC method yielded lower errors than any of the individual estimators, including Liljestrand, at both high and low estimated CO levels. Comparison of the LC estimator at HRSQI and ABPSQI thresholds of 90 with the other estimators are shown in Fig.2-40, with the LC estimator achieving the lowest error. Performance of estimators were also evaluated as a function of the number of available calibration TCO points, and results indicate that error decreased as the number of calibration points increased. In fact, error from the LC estimator was lower than all other estimators up until 13 training points, after which the Liljestrand method outperformed the rest. Therefore, we recommended the use of the combined estimator when fewer than 13 TCO points are available for calibration, after which the Liljestrand estimator provides a better estimate.

The clinical utility of the Liljestrand CO estimator and the LC estimator at rec-

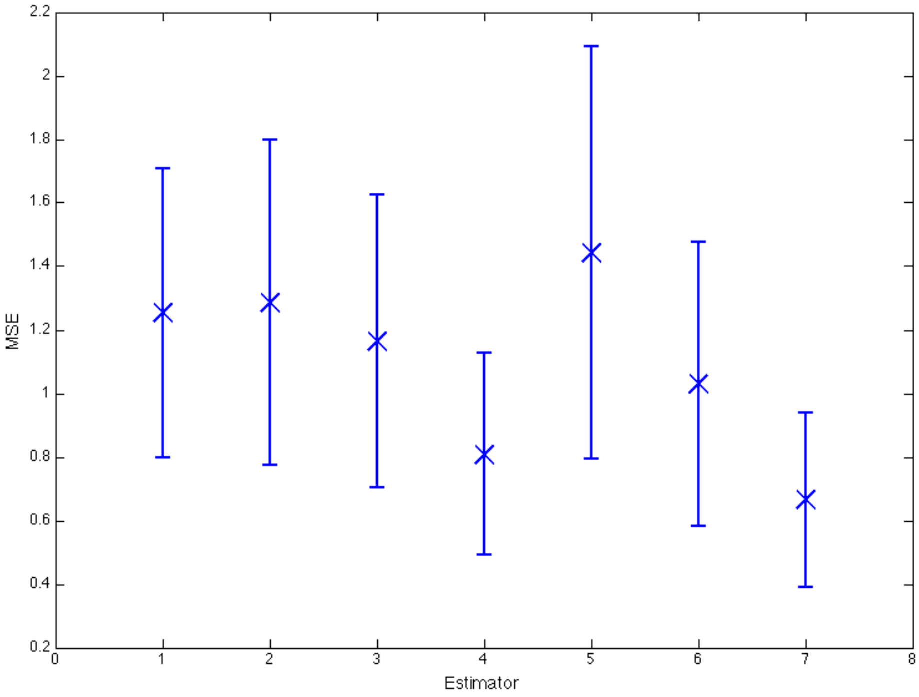

Figure 2-40: 5% bootstrap Mean Square Error (MSE) with raw estimations. The estimators are in the following order: 1) mean arterial pressure, 2) Windkessel, 3) Herd, 4) Liljestrand, 5) Systolic Area, 6) Wesseling, and 7) LC. Errors bars indicate standard deviations over 20 runs.

ommend SQI thresholds are explored in the following chapter.

Chapter 3

Estimated Peripheral Resistance & Vasoactive Drugs

Few studies have documented the utility of estimated CO or peripheral resistance in relation to how well they reflect medications administered. Although many have examined the effects of vasoactive medications on measured peripheral resistance, a literature search indicates that all of these studies have been performed in controlled settings rather than real-world clinical settings. The goal of this section is to determine how well estimated peripheral resistance derived from CO estimation techniques described in Section 2.2 correspond to pressors given in an ICU setting. Estimated peripheral resistance was derived from CO estimates using the Liljestrand and LC estimators with SQI correction for ABP and HR. Changes in estimated peripheral resistance ($\hat{R}$) were correlated with changes in vasoactive medications to determine if there is potentially any clinical utility of such estimates.

3.1 Vasoactive Drugs

Table 3.1 lists the drugs considered in this study and their vasoactive effects. Note that for some drugs, the nature of the drug is dose-dependent, and can switch from vasodilation to vasoconstriction and vice versa [28].

Medication	Vasodilator	Vasoconstrictor
Dobutamine	x	
Dopamine, $< 10\mu$g/kg/min	x	
Dopamine, $\geq 10\mu$g/kg/min		x
Levophed		x
Neosynephrine		x

Table 3.1: List of vasoactive medications and their effects on peripheral resistance.

3.1.1 Dobutamine

Dobutamine is a synthetic catecholamine used to increase cardiac output primarily in patients with decompensated heart failure due to systolic dysfunction who also have a normal blood pressure [28]. As a β_1-receptor agonist, dobutamine produces positive inotropic and chronotropic effects, while as a weak β_2-receptor agonist, dobutamine also produces peripheral vasodilation. Dobutamine causes a dose-dependent increase in stroke volume, decrease in cardiac filling pressures, and decrease in systemic vascular resistance. Because dobutamine does not usually raise the blood pressure, it is not recommended in patients with cardiogenic shock.

3.1.2 Dopamine

Dopamine is an endogenous catecholamine that activates a variety of receptors depending on the dosage. At low dose rates (up to 10 μg/kg/min), dopamine innervates the β-receptors in the heart and peripheral circulation, resulting in an increase in myocardial contractility, increase in heart rate, and peripheral vasodilation [30]. This results in an increase in cardiac output. At high dose rates ($>$10 μg/kg/min), dopamine progressively activates α-receptors in the systemic and pulmonary circulations, resulting in pulmonary and systemic vasoconstriction. Cardiac output decreases at these dose rates. Dopamine is often used to perform cardiac stimulation and peripheral vasoconstriction, such as during cardiogenic shock. Dopamine can also be used to correct hypotension in septic shock.

3.1.3 Levophed

Levophed, also known as norepinephrine, is a vasopressor often used to correct hypotension, particularly in septic shock [28]. Levophed stimulates α-receptors, resulting in dose-dependent increase in systemic vascular resistance. Levophed stimulates cardiac β-receptors as well, but the effects on cardiac output vary.

3.1.4 Neosynephrine (Phenylephrine)

Neosynephrine, often used as a decongestant in nasal passages, is a α-receptor agonist and acts as a vasoconstrictor. It also stimulates β-receptors in the heart to a lesser extent. Cardiac output slightly decreases, while blood pressure is increased [18].

3.2 Experimental Procedure

3.2.1 Patient selection

A total of 89 cases with ABP waveforms during the administration of vasoactive drugs listed in Table 3.1 were found in the MIMIC II Database. Those with intra-aortic balloon pumps or poor quality ABP or HR during the periods of interest were excluded, resulting in 76 cases. Each case was classified using primary and secondary ICD-9 codes listed in Table 3.2 into 3 conditions: septic shock, cardiogenic shock, and/or hemorrhage.

3.2.2 Estimated resistance

For each record, uncalibrated CO estimates (UCO) were made on non-overlapping 1-minute windows at ABPSQI and HRSQI thresholds of 90. A global calibration constant was chosen using the median of k_i, $\tilde{\mu}_{k_i}$, obtained from the 121 records used in Chapter 2, where i denotes the estimator method as listed in the order shown in Table 2.3. Calibration was performed to obtain estimated CO (ECO) for estimator i such that:

Septic Shock
85.52 Septic shock 995.92 Severe sepsis
Cardiogenic Shock
785.51 Cardiogenic shock
Hemorrhage
578.9 Hemorrhage of gastrointestinal tract, unspecified 569.3 Hemorrhage of rectum and anus 431 Intracerebral hemorrhage 430 Subarachnoid hemorrhage

Table 3.2: List of ICD-9 codes used to identify patients with septic shock, cardiogenic shock, and hemorrhage.

$$ECO_i = \tilde{\mu}_{k_i} \cdot UCO$$

The Liljestrand ($i = 3$) and LC estimators were analyzed in this chapter. In the case of the LC estimator, scaling each contribution was particularly important in preserving the weighting effect of each estimator. The individual estimators were weighted according to the coefficients and an offset determined by the LC estimator:

$$ECO_{LC} = 0.6277 + \mathbf{a}\mathbf{b}'$$

where

$$\mathbf{a} = [0.2317 \quad -0.4372 \quad -0.3232 \;\; 0.5669 \quad -0.2921 \;\; 1.1471]$$

$$\mathbf{b} = [ECO_1 \quad ECO_2 \cdots ECO_6]$$

A mean pressure (P_m) trend, sampled at 1-minute intervals, was obtained by taking the median of beat-by-beat mean pressures with an ABPSQI of at least 90. By applying Ohm's law to the lumped-parameter model described in Section 2.1.1, $\hat{R}$ can be calculated as the ratio of P_m in mmHg and ECO in L/min and multiplied by a constant to convert into peripheral resistance units (PRU) as follows:

$$\hat{R} = \left(\frac{P_m}{ECO}\right)\left(\frac{60}{1000}\right)$$

To remove sudden changes in $\hat{R}$ due to artifacts or non-physiological measurements not rejected by ABPSQI and HRSQI, a 31-point median filter was applied. Since the $\hat{R}$ is calculated for each 1-minute interval, this is equivalent to filtering over 31 minutes to obtain each $\hat{R}$ point.

3.2.3 Event identification

For each case, times when only one vasoactive drug was being administered were identified. Times when vasopressin and epinephrine were also being administered at the same time as the drugs in Table 3.1 were not considered in this study. An event was identified as a change in pressor dose after at least 90 minutes of stable drug levels, or a *region of drug stability*. If dopamine was administered, dopamine levels above $\geq 10\mu$g/kg/min were not included in the analysis such that only doses with vasodilating effects were considered. Furthermore, $\hat{R}$ had to be available within the vinicity of the dose changes, as detailed in Section 3.2.4. As an example, Fig.3-1 shows the mean ABP, estimated CO, $\hat{R}$, and levophed dose levels. Regions of drug stability are indicated in red in the levophed plot, and events occur at approximately 1000 min, 1215 min, and 1785 min. Although medication levels were adjusted at approximately 1500 min, insufficient $\hat{R}$ data were available to characterize the effect of the medication.

With these restrictions, 132 dose change events were selected from 37 cases.

3.2.4 Estimated resistance changes

For each event, $\hat{R}$ before and after the change in pressor dose was examined. The median $\hat{R}$ 15 minutes prior to the dose change was defined as the baseline, $\hat{R}^-$. $\hat{R}$ levels after the next region of drug stability was reached was characterized using the median of $\hat{R}$ during the 6th to 20th minutes of the stable region following the change,

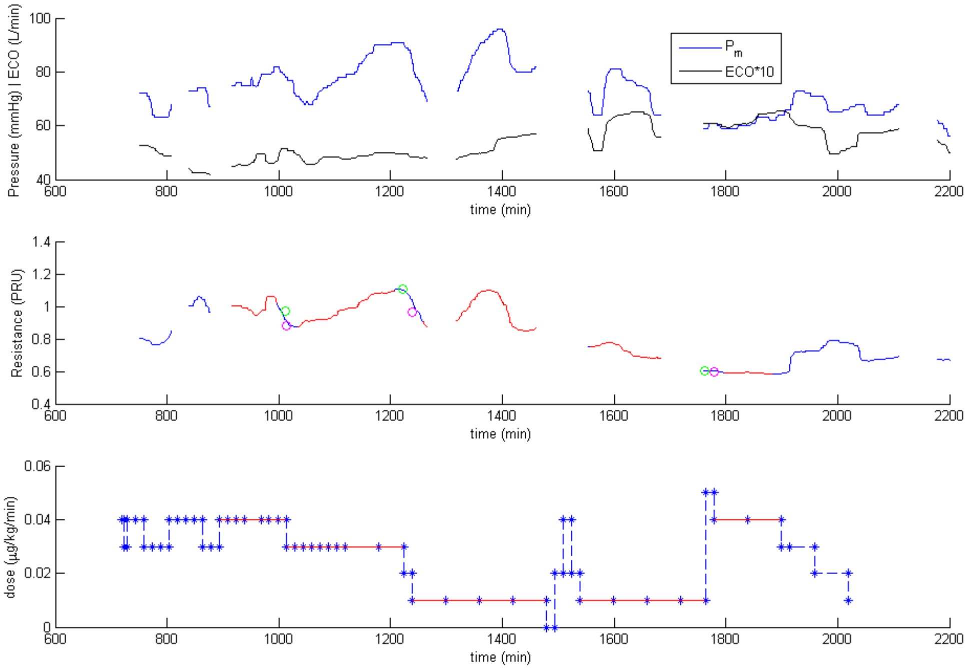

Figure 3-1: P_m, ECO, $\hat{R}$, and levophed doses for a41244. Record starts on March 23, 2017 at 00:21:39. Regions of hemodynamic stability are marked in red on resistance and levophed plots. Green circles represent $\hat{R}^-$, and magenta circles represent $\hat{R}^+$.

such that 5 minutes was allotted for the drug to take effect. This level of $\hat{R}$ after the event was defined as $\hat{R}^{+}$. In Fig.3-1, $\hat{R}^{-}$ for each event is shown in green circles, and $\hat{R}^{+}$ is shown in magenta circles. The percent change in $\hat{R}$ is defined as follows:

$$\Delta\hat{R} = (100)\left(\frac{\hat{R}^{+} - \hat{R}^{-}}{\left(\frac{1}{2}\right)\left(\hat{R}^{+} + \hat{R}^{-}\right)}\right)$$

Rate of change in $\hat{R}$ was also analyzed. The time in minutes elapsed between regions of drug stability for each event was determined. For each event, the duration of resistance change was calculated as the time (t^{-}) between the minute before the end of one region of drug stability to the start of the following one (t^{+}). t^{-} was assigned to be a minute before the end of the region of drug stability to prevent dividing by infinity if the event was at the intersection of two regions of drug stability, such as the event at 1000 minutes in Fig. 3-1. Clinically, this also accounts for the time the ICU nurses take to change medication levels. The slope $\nabla\hat{R}$ in units of PRU/min is:

$$\nabla\hat{R} = \frac{\hat{R}^{+} - \hat{R}^{-}}{t^{+} - t^{-}}$$

3.2.5 Dose level changes

For each event, pressor dose changes were characterized. The baseline dose, D^{-}, was the drug level prior to the dose change; the new dose level, D^{+}, was the drug level of the following region of drug stability. The percent change of dose level is defined as follows:

$$\Delta D = (100)\left(\frac{D^{+} - D^{-}}{\left(\frac{1}{2}\right)(D^{+} + D^{-})}\right)$$

For gradient comparison, t_{-} and t_{+} were defined for dose level changes in the same manner as for $\hat{R}$. The slope ∇D in units of μg/kg/min^2 is:

$$\nabla D = \frac{D^{+} - D^{-}}{t^{+} - t^{-}}$$

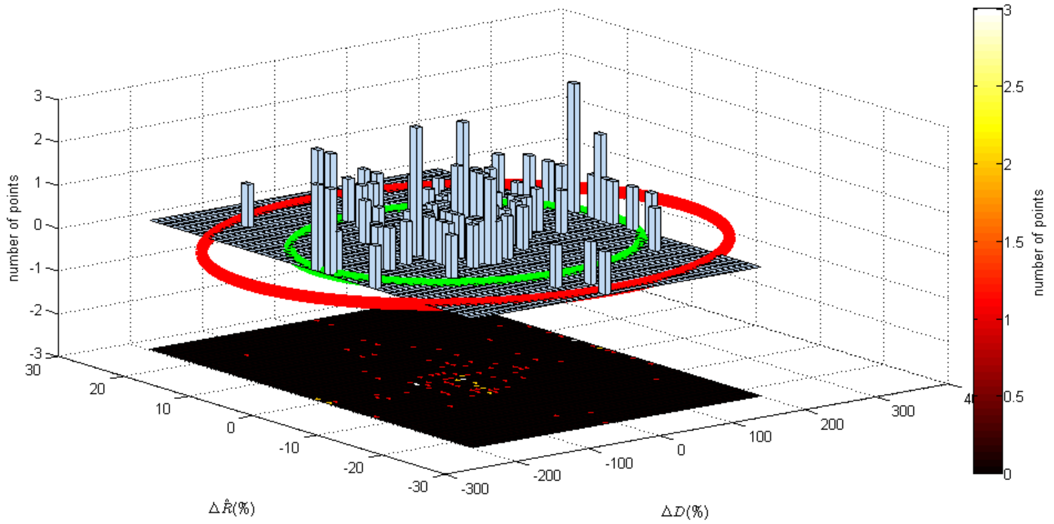

Figure 3-2: Distribution of $\Delta\hat{R}$ and ΔD for vasoconstrictors for the Liljestrand estimator. The green and red ellipses represent the 2 and 3 standard deviation boundaries of the joint distribution.

3.2.6 Outlier rejection

For vasoconstrictors and vasodilators, a joint probability mass function (PMF) was estimated for each from a histogram of $\Delta\hat{R}$ and ΔD. For the Liljestrand estimator, the distributions for vasoconstricting medications for $\Delta\hat{R}$ and ΔD analysis is shown in Fig.3-2 and for vasodilating medications in Fig.3-3. The means (μ) and standard deviations (σ) of $\Delta\hat{R}$ and ΔD were calculated to define an ellipse with a semimajor axis of $2\sigma_{\Delta D}$ and semiminor axis of $2\sigma_{\Delta\hat{R}}$, centered at $\mu_{\Delta D}$ and $\mu_{\Delta\hat{R}}$. This ellipse is shown in green, while an analogous ellipse with a semimajor axis of $3\sigma_{\Delta D}$ and semiminor axis of $3\sigma_{\Delta\hat{R}}$ is shown in red. Points that occurred outside of the 2σ region were considered outliers and were not considered in the correlation analysis. An analogous procedure was conducted for $\nabla\hat{R}$ and ∇D to exclude outliers. The distributions for vasoconstrictors are shown in Fig.3-4 and for vasodilators in Fig.3-5.

The same method of outlier rejection was performed for the LC estimator. The histograms of $\Delta\hat{R}$ and ΔD are shown in Fig.3-6 for vasoconstrictors and Fig.3-7 for vasodilators. The histograms of $\nabla\hat{R}$ and ∇D are shown in Fig.3-8 for vasoconstrictors and Fig.3-9 for vasodilators.

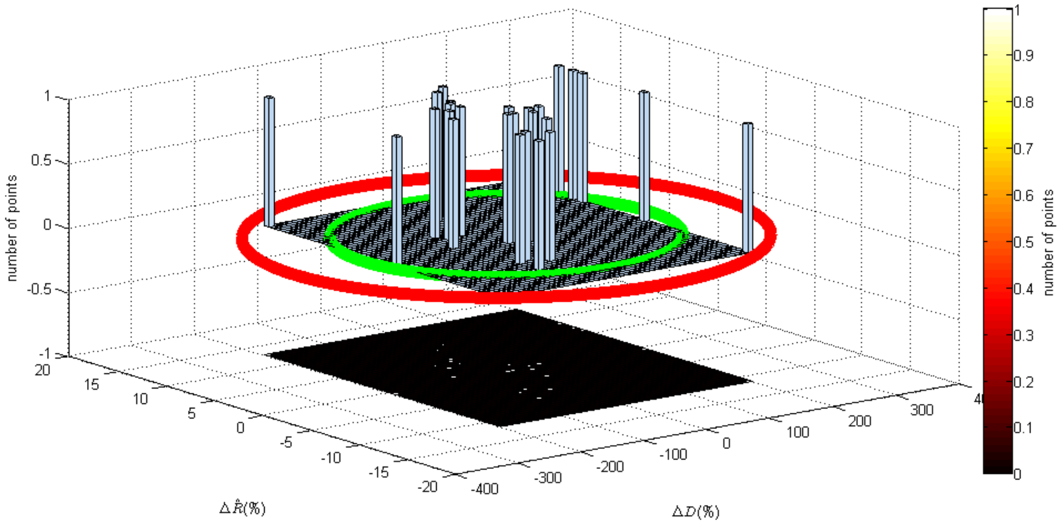

Figure 3-3: Distribution of $\Delta\hat{R}$ and ΔD for vasodilators for the Liljestrand estimator. The green and red ellipses represent the 2 and 3 standard deviation boundaries of the joint distribution.

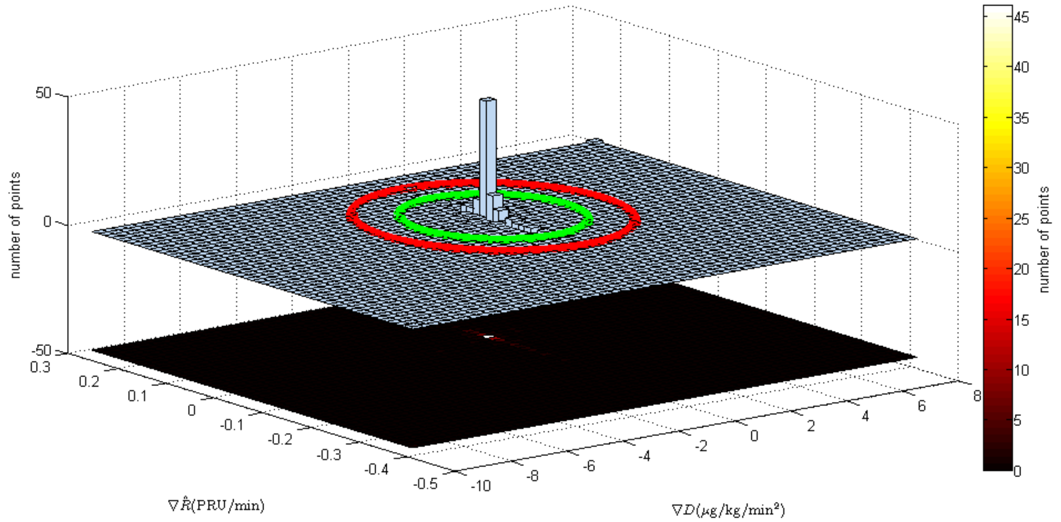

Figure 3-4: Distribution of $\nabla\hat{R}$ and ∇D for vasoconstrictors for the Liljestrand estimator. The green and red ellipses represent the 2 and 3 standard deviation boundaries of the joint distribution.

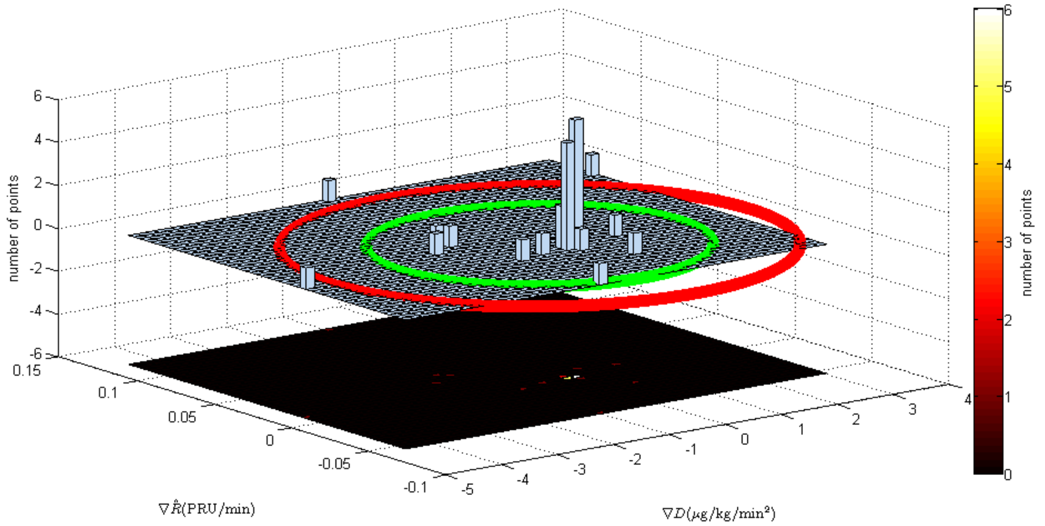

Figure 3-5: Distribution of $\nabla\hat{R}$ and ∇D for vasodilators for the Liljestrand estimator. The green and red ellipses represent the 2 and 3 standard deviation boundaries of the joint distribution.

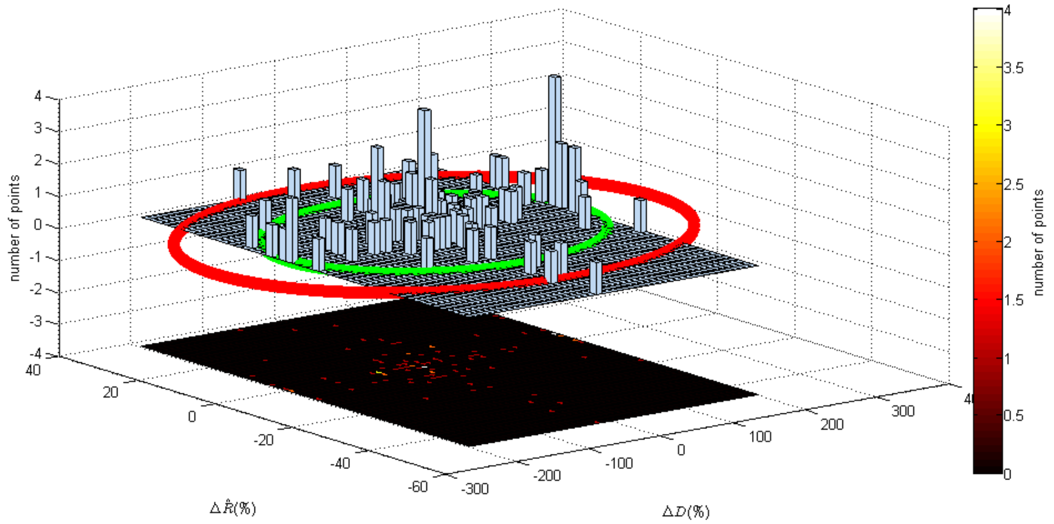

Figure 3-6: Distribution of $\Delta\hat{R}$ and ΔD for vasoconstrictors for the LC estimator.

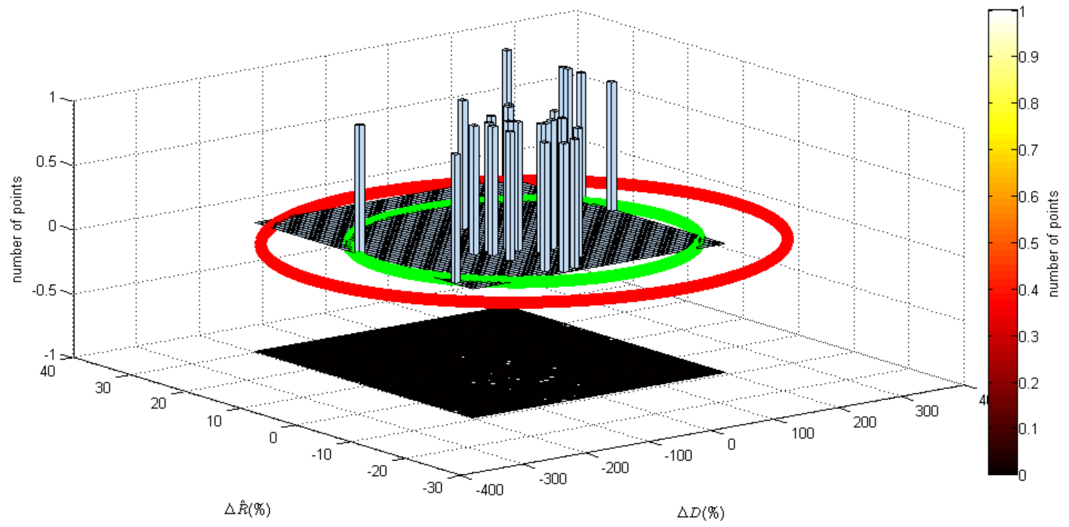

Figure 3-7: Distribution of $\Delta\hat{R}$ and ΔD for vasodilators for the LC estimator.

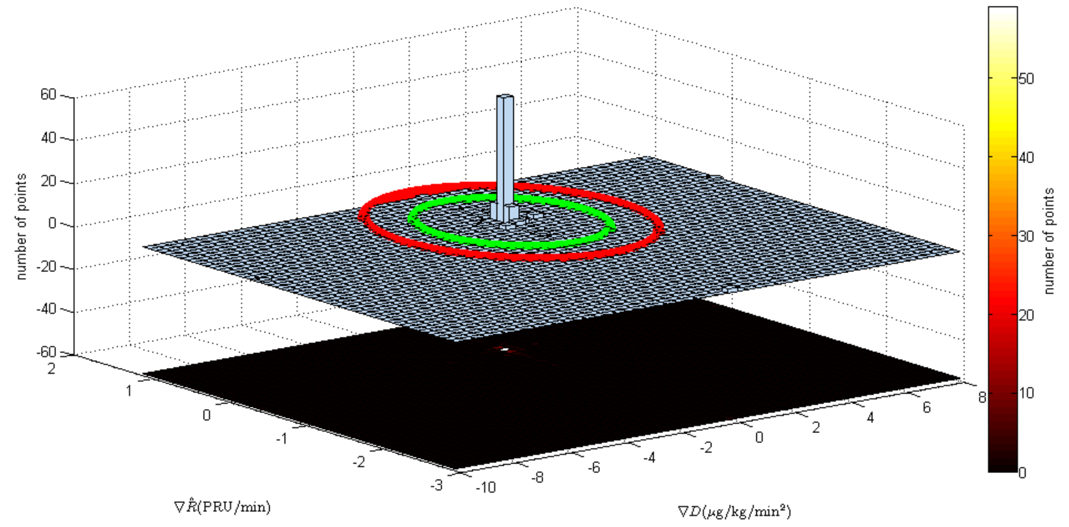

Figure 3-8: Distribution of $\nabla\hat{R}$ and ∇D for vasoconstrictors for the LC estimator.

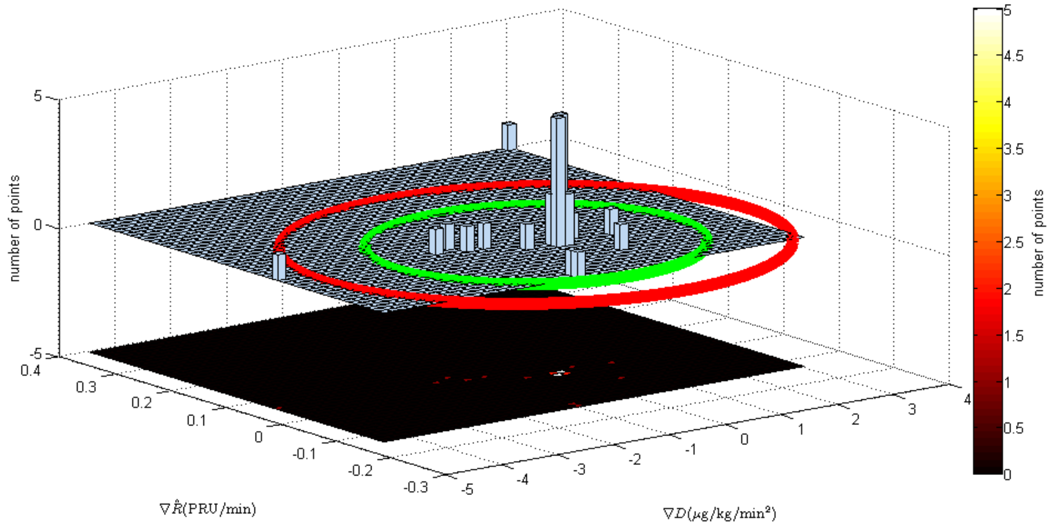

Figure 3-9: Distribution of $\nabla\hat{R}$ and ∇D for vasodilators for the LC estimator.

3.3 Results

3.3.1 Proportion of expected events

The expected changes in $\hat{R}$ were matched with their corresponding changes in drug level for each event. For vasodilators, increase in medication would theoretically result in a decrease in estimated resistance, and vice versa. Likewise, for vasoconstrictors, increase in medication would result in increased estimated resistance, and a decrease in the former would also result in a decrease in the latter. The proportion of $\hat{R}$ changes that follow these medication level changes, or the proportion of *expected events*, are listed in Table 3.3 for $\hat{R}$ based on the both the Liljestrand and LC estimators. For most medications, the expected changes in $\hat{R}$ correspond to changes in medication levels, but dopamine performed poorly in matching medication changes to $\hat{R}$ for resistance estimates based on both CO estimators. The LC estimator had a lower proportion of resistance estimates in their expected directions for all medications except dopamine.

Medication	Correct expected changes (%)	Correct expected slopes
Liljestrand		
Vasoconstrictors	67.9	67.3
Levophed	65.5	64.1
Neosynephrine	72.4	73.0
Vasodilators	45.5	45.5
Dobutamine	66.7	80.0
Dopamine	37.5	35.4
LC		
Vasoconstrictors	64.0	62.4
Levophed	59.6	61.3
Neosynephrine	72.4	64.1
Vasodilators	47.6	37.5
Dobutamine	50.0	50.0
Dopamine	46.7	33.3

Table 3.3: Expected estimated resistance and medication changes.

3.3.2 Regression analysis for $\Delta\hat{R}$ and ΔD

For each event, $\Delta\hat{R}$ was plotted against ΔD, as shown in Fig.3-10 for the Liljestrand estimator. Quadrants are separated by red dashed lines. For vasoconstrictors, the events that behave as expected are located in the first and third quatrants, while for vasodilators, the events that behave as expected are located in the second and fourth quatrants. To quantify the relationship between $\Delta\hat{R}$ and ΔD for each, a linear best fit was performed on the changes in dose levels and estimated resistances, as shown in Fig.3-10. Vasoconstricting medications should have a positive slope, while vasodilating medications should have a negative slope. Regression was also performed for each medication analyzed; results are shown in Fig.3-11. The best fit is shown with a green line in each plot, with regression coefficients and R^2 values listed in Table 3.4.

The same analysis was performed for the LC estimator. Results for linear regression of vasoconstrictors and vasodilators are shown in Fig.3-12, and regressions according to medication are shown in Fig.3-13. Regression coefficients and R^2 values are listed in Table 3.5.

For Liljestrand estimator $\Delta\hat{R}$ and ΔD analysis, while levophed, neosynephrine,

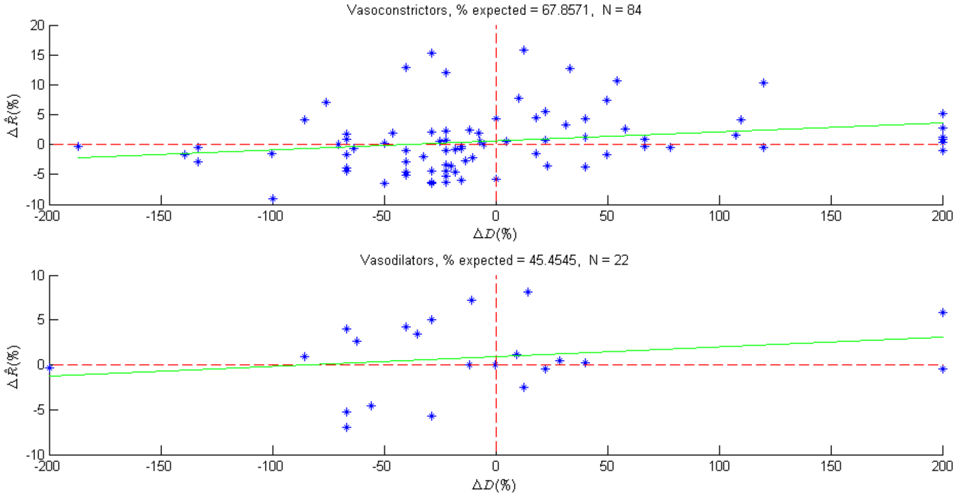

Figure 3-10: Medication changes and corresponding resistance changes for each event, organized by drug effect, for Liljestrand estimator.

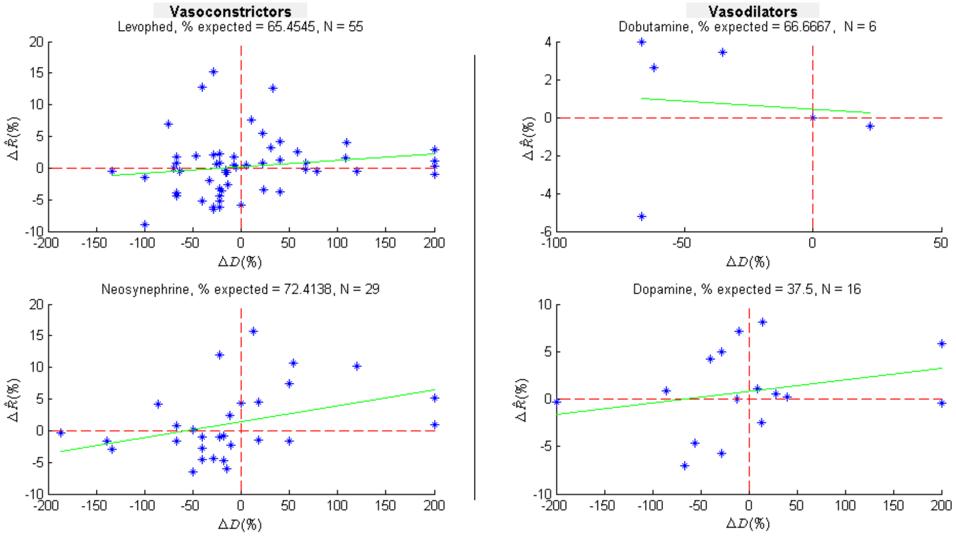

Figure 3-11: Medication changes and corresponding resistance changes for each event, organized by medication, for Liljestrand estimator.

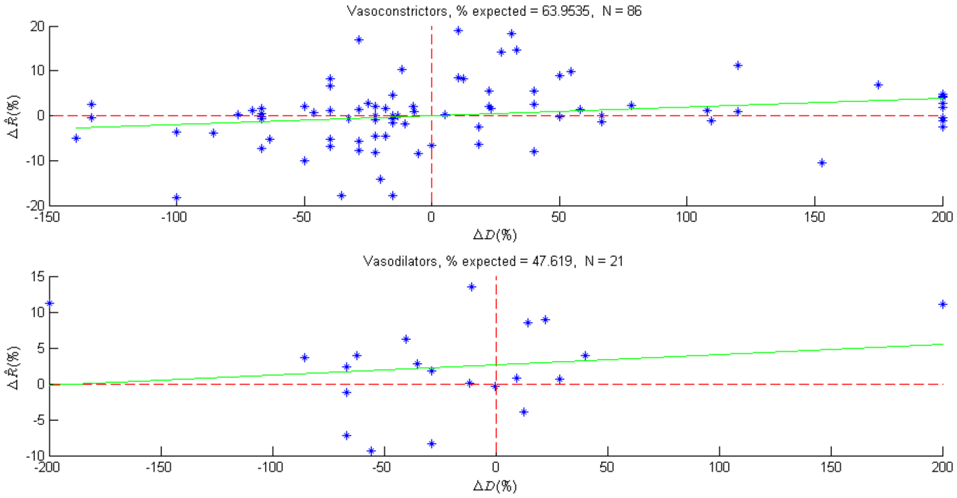

Figure 3-12: Medication changes and corresponding resistance changes for each event, organized by drug effect, for LC estimator.

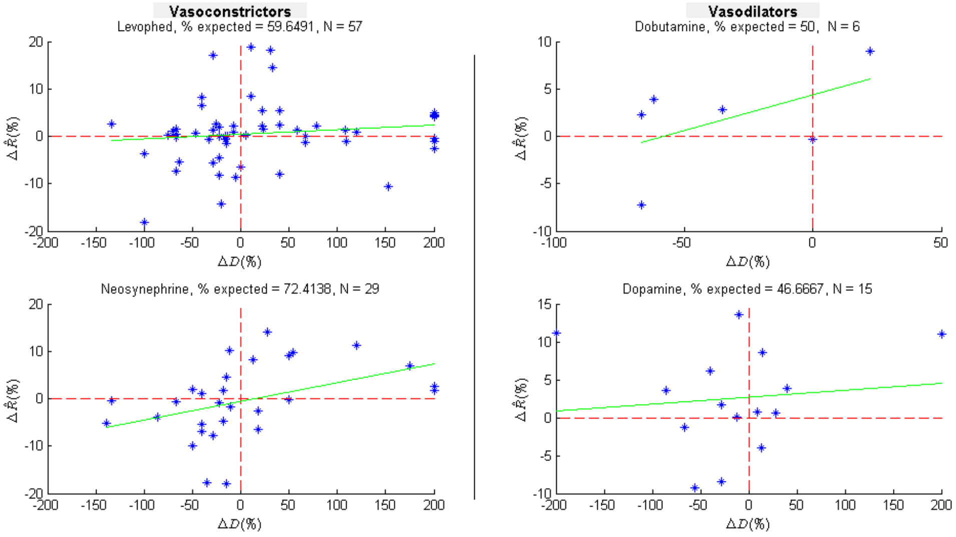

Figure 3-13: Medication changes and corresponding resistance changes for each event, organized by medication, for LC estimator.

Medication	a	b	R^2
Vasoconstrictors	0.0152	0.5815	0.051
Levophed	0.0100	0.2002	0.026
Neosynephrine	0.0252	1.4755	0.14
Vasodilators	0.0108	0.8729	0.057
Dobutamine	-0.0084	0.4303	0.0086
Dopamine	0.0121	0.7905	0.070

Table 3.4: $\Delta\hat{R}$ and ΔD regression results for the Liljestrand estimator. Linear regression line in the form of $y = ax + b$.

Medication	a	b	R^2
Vasoconstrictors	0.0195	0.0373	0.027
Levophed	0.0099	0.4548	0.016
Neosynephrine	0.0394	-0.4652	0.18
Vasodilators	0.0141	2.6135	0.055
Dobutamine	0.0761	4.3915	0.29
Dopamine	0.0090	2.6898	0.012

Table 3.5: $\Delta\hat{R}$ and ΔD regression results for the LC estimator. Linear regression line in the form of $y = ax + b$.

and dobutamine had expected linear regression slopes, dopamine events displayed a positive slope relationship, indicating that increasing dopamine tends to *increase* estimated resistance. The low R^2 values for the linear regressions suggest that the effect of change in medication level on change in estimated resistance is weak. For the LC estimator, all regressions indicate a positive slope relationship; that is, for all medications, regardless of whether it be a vasodilator or vasoconstrictor, tend to increase estimated resistance. In particular, for dobutamine, the R^2 value for the LC estimator is higher than that of the Liljestrand estimator, indicating that the constricting effect of dobutamine is a stronger relationship than the dilating relationship found using the Liljestrand estimator. However, the sparsity of dobutamine events used for the regression analysis indicate that this conclusion is very weak and should be further examined using additional data points.

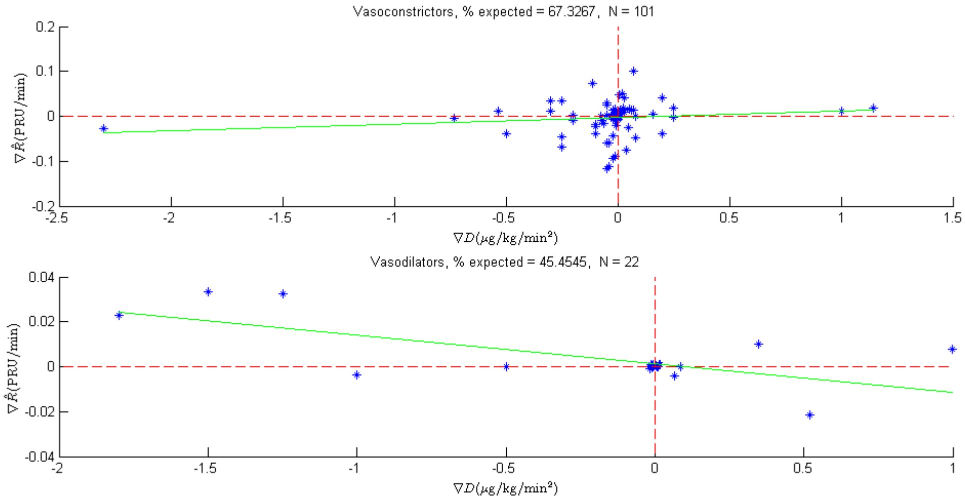

Figure 3-14: Medication slopes and corresponding resistance slopes for each event, organized by drug effect for the Liljestrand estimator.

3.3.3 Regression analysis for $\nabla\hat{R}$ and ∇D

An analogous analysis was performed for $\nabla\hat{R}$ and ∇D; $\nabla\hat{R}$ and ∇D were matched for each change for vasoconstrictors and vasodilators in Fig.3-14 and for each drug in Fig.3-15 for the Liljestrand estimator. Linear regression results are shown in Table 3.6.

Medication	a	b	R^2
Vasoconstrictors	0.0145	-0.0034	0.47
Levophed	0.0185	-0.0046	0.0063
Neosynephrine	0.0148	-0.0013	0.079
Vasodilators	-0.0127	0.0013	0.019
Dobutamine	-0.0177	-0.0017	0.80
Dopamine	0.0015	-0.0005	0.0090

Table 3.6: $\nabla\hat{R}$ and ∇D regression results for the Liljestrand estimator. Linear regression line in the form of $y = ax + b$.

The same slope analysis was performed for the LC estimator. Results for linear regression of vasoconstrictors and vasodilators are shown in Fig.3-16, and regressions according to medication are shown in Fig.3-17. Regression coefficients and R^2 values are listed in Table 3.7.

For Liljestrand estimator analysis, like regression analysis for $\Delta\hat{R}$ and ΔD, dobu-

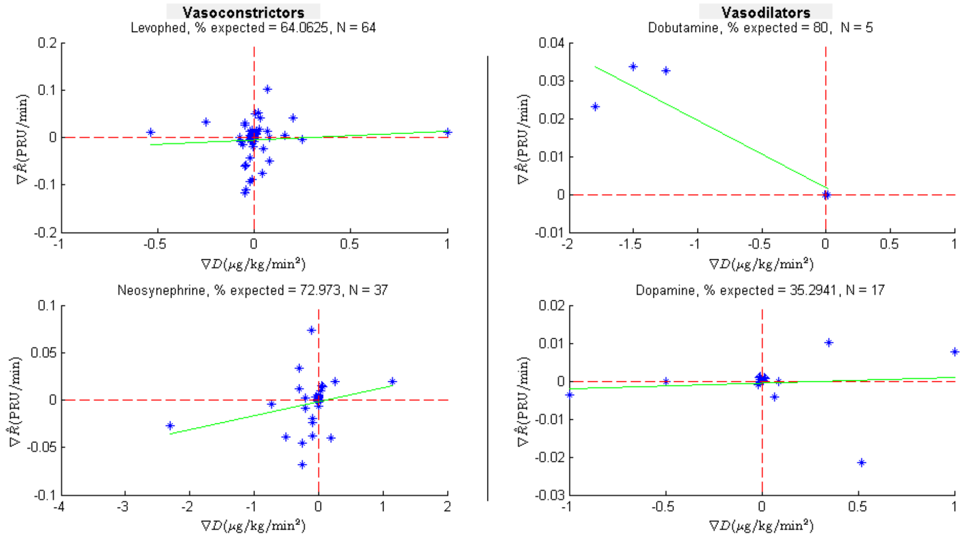

Figure 3-15: Medication slopes and corresponding resistance slopes for each event, organized by medication for the Liljestrand estimator.

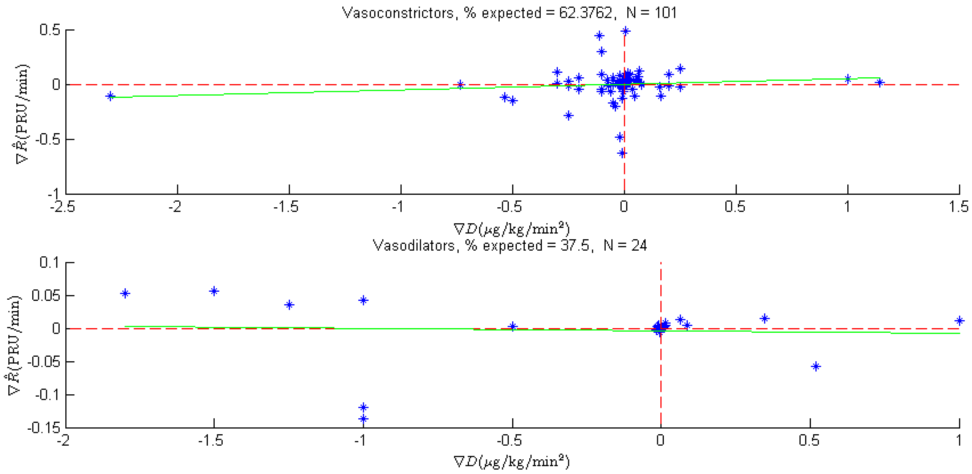

Figure 3-16: Medication slopes and corresponding resistance slopes for each event, organized by drug effect for the LC estimator.

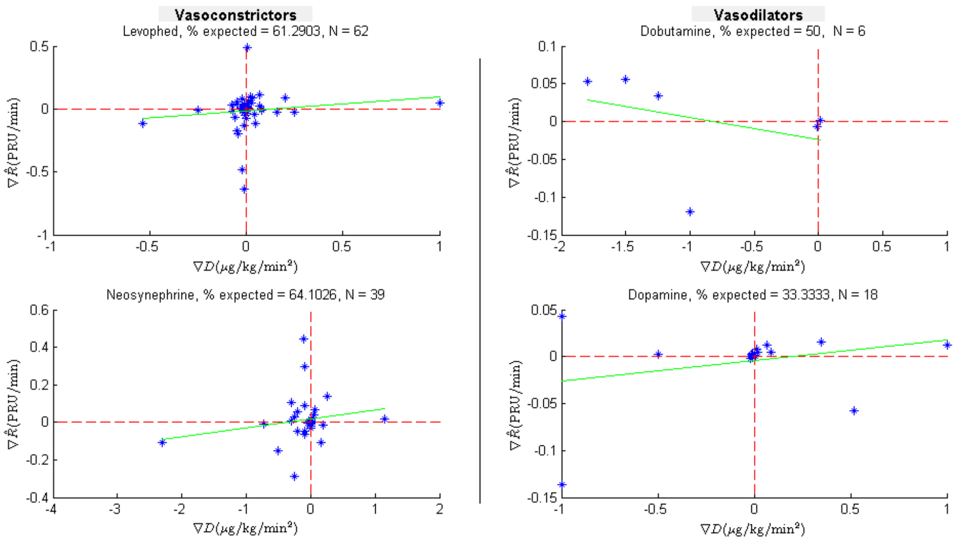

Figure 3-17: Medication slopes and corresponding resistance slopes for each event, organized by medication for the LC estimator.

Medication	a	b	R^2
Vasoconstrictors	0.0499	-0.0018	0.0033
Levophed	0.1126	-0.014	0.018
Neosynephrine	0.0473	-0.0163	0.036
Vasodilators	-0.0039	0.0038	0.015
Dobutamine	-0.0291	-0.0235	0.12
Dopamine	0.0217	-0.0043	0.071

Table 3.7: $\nabla\hat{R}$ and ∇D regression results for the LC estimator. Linear regression line in the form of $y = ax + b$.

tamine, levophed, and neosynephrine exhibited the expected slope sign, whereas dopamine changes were positively correlated rather than negatively correlated as predicted. The R^2 values for the linear regressions were low, indicating the weak effect of slope of medication level on slope of estimated resistance. For the LC estimator, unlike the analysis for the percent change regressions, slope of dobutamine level was negatively correlated with estimated resistance slope, as expected. Both Liljestrand and LC estimators indicate a positive correlation between dopamine level slopes and estimated resistance slopes, with this relationship stronger for the LC estimator. Dobutamine generally exhibits a higher R^2 value but is confounded by the few number of points used in regression.

3.4 Discussion

Little correlation was found between changes in estimated resistance and medication dose, whether that be by examining changes ($\Delta\hat{R}$ and ΔD) or taking into account temporal factors using slopes ($\nabla\hat{R}$ and ∇D) using either the Liljestrand or LC estimator. In particular, the effect of dopamine was inconsistent with the known vasodilating action the drug has at low doses, although this discrepency may be due to the low number of samples available. Rosenthal et al [33] described the strength of a model by the magnitude of R^2. A "medium effect size" is when $R^2 \approx 0.1$, a "large effect size" is when $R^2 \approx 0.25$, and a "very large effect size" is when $R^2 \approx 0.4$. Following these guidelines, for the Liljestrand estimator, we can see that changes in vasoactive medication had little effect on $\Delta\hat{R}$, although neosynephrine change had a medium effect on $\Delta\hat{R}$. The R^2 value between neosynephrine ΔD and $\Delta\hat{R}$ increased when using the LC estimator, suggesting that the LC estimator produces a better representation of estimated CO than Liljestrand. ∇D for vasoconstrictors had a very large effect on $\nabla\hat{R}$, but the remaining vasoactive variables examined had little effect on $\nabla\hat{R}$. While some regressions for dobutamine yielded high R^2 values, this result was confounded by the small number of points used in regression analysis and is therefore inconclusive.

The lack of clear correlation between changes in and slopes of medications on estimated resistance can be attributed to the variations in the effects of drugs on various patients. The extent of resistance change may vary between patients, so a same increase in pressor levels may result in different degrees of resistance changes for different patients, leading to a low R^2 value when performing regression analysis. In particular, for dopamine, which can have vasodilating or vasoconstricting effects depending on the dose, the 10μg/kg/min threshold beyond which the drug becomes vasoconstricting may depend on the patient and his/her hemodynamic condition at the time of the intervention. Therefore, all the dopamine events for which medication level was below 10 μg/kg/min may not have have been administered to lower peripheral resistance.

Furthermore, additional medical procedures or conditions may have occurred during the time pressors were administered. The deterioration of a pathology or administration of drugs beyond the scope of those considered in this chapter could have affected hemodynamics.

However, the most important confounding factor in correlating estimated resistance changes and medication level changes is that the SQI metrics used to remove artifactual or non-physiological ABP waveforms were insufficient for continuous CO estimation. Although Chapter 2 discusses using ABPSQI and HRSQI to reduce estimation error, windows of up to only 7 minutes local to thermodilution measurements were used to compare estimated CO and TCO. However, in examining continuous CO estimation necessary for correlation with medication levels, the effects of gradual non-physiological changes in ABP over longer periods of tens of minutes can be seen in the form of implausible $\hat{R}$ values that can increase or decrease beyond the limits of physiological norms. While steady changes in a patient's hemodynamic stability may also lead to these gradual changes in $\hat{R}$, examination of the ABP waveform from which CO estimation parameters were extracted, complemented with additional information at the time such as other measured signals, other medications administered, and nurse's notes, indicated corrupt signals of dubious signal fidelities. Current SQI metrics work well in detecting artifacts or changes that can occur within a few beats, but not over tens of minutes. The shortcomings in current SQI metrics are explored in the following chapter.

Chapter 4

Limitations of Signal Quality Indices

Signal quality indices, described in Sections 1.5 and 1.6, for arterial blood pressure and heart rate were used in the cardiac output estimation procedure to reject artifictual or non-physiological data. While the procedure described in Chapter 2 utilizes SQIs to ensure accurate CO estimation, examining the clinical utility of estimated CO through correlation of vasoactive medication with peripheral resistance estimates reveals that dubious estimates are still produced, as seen in Chapter 3. The limitations of estimating CO and the resulting peripheral resistance through current SQI methods are discussed in this chapter, focusing on ABP signal quality. A proposed method for detecting damping is described.

4.1 SQI for ABP

Current SQI algorithms detect changes that occur within a few beats. ABPSQI consists of $jSQI$ and $wSQI$, both of which use beat-by-beat changes in blood pressure features to determine signal quality. This metric detects artifacts with short onsets, such as sudden patient movement or sensor disconnections. However, other artifacts such as ABP damping are not well-detected. For these artifacts, the change in blood pressure occurs more gradually, up to a few hours, until ABP waveform is so implausible that it is finally designated as artifactual by ABPSQI, if it is detected at all. Possible causes for these types of non-physiological waveforms include clogging of the transducer or kinked tubing. For the Liljestrand estimator, any underestimation of pulse pressure or overestimation of systolic or diastolic pressures lead to a lower stroke volume and consequently a lower CO estimate.

Li et al classified ABP artifacts in [24] into the following categories:

1. Saturation to mean: decreased pulse pressure - the systolic pressure decreases, diastolic pressure increases, and mean pressure remains constant
2. Saturation to maximum: systolic, diastolic and mean pressure increase to the maximum value allowed by the patient monitoring system
3. Saturation to minimum: systolic, diastolic and mean pressure decrease to the maximum value allowed by the patient monitoring system
4. High frequency
5. Square wave
6. Impulse

While artifacts 4-6 are easily detected with ABPSQI, the first 3 are not, particularly when the saturations are over the course of tens of minutes. Furthermore, this ABP artifact classification scheme does not take into consideration artifacts where systolic pressure changes while diastolic pressure remains constant, or vice versa. At other times, examining ABP waveform while taking into consideration HR reveals suspicious behavior that would not have otherwise been obvious by only following ABP.

4.1.1 Saturation

Saturation artifacts are typically a gradual convergence of systolic, diastolic, and mean pressures to a common value. An example is shown in Fig.4-1, where the estimated CO, fused HR, and resulting estimated peripheral resistance are shown.

Estimated CO procedure and R calculations were derived as explained previously in chapters 2 and 3, calculated over one-minute intervals only when 6 or more beats satisfied ABPSQI $\geq$ 90 and HRSQI $\geq$ 90. The extracted systolic, diastolic and mean pressures are also displayed at one minute intervals only when sufficient beats satisfied SQI requirements. These pressures are overlaid with the raw blood pressure waveform. Periods of signal quality greater than 90 for HRSQI and ABPSQI are flagged on their respective plots. Impulse artifacts at approximately 1525 min are readily detected, but the blood pressure waveform gradually saturates to the mean blood pressure starting at 1560 min, with systolic pressure decreasing and diastolic pressure increasing. Damping is not detected until the narrowing of the signal has already begun and is not detected until approximately 1610 minutes - almost an hour after the onset of abnormality. Consequently, underestimation of pulse pressure lowers the CO estimate and, along with a drop in HR, leads to a large increase in estimated resistance to twice of its initial value.

A saturation artifact with a shorter onset time is shown Fig.4-2 at approximately 1730 min. Although the saturation artifact is detected by ABPSQI, the narrowing of the ABP waveform that follows up to the saturation artifact is not, as shown in Fig.4-3. The pulse pressure rapidly decreases, and diastolic pressure increases while systolic pressure decreases. This ABP distortion leads to a sharp downswing in the estimated CO and sharp upswing in estimated R.

4.1.2 Systolic or diastolic pressure jumps

For some artifacts, either systolic or diastolic pressure is significantly altered but is still within physiological limits and thus not detected by current SQI methods. In addition to the saturation artifacts discussed previously, Fig.4-2 also illustrates a weakness of current SQI metrics not accounted for in Li et al's artifact classification scheme [24]. At approximately 1640 min to 1670 min, diastolic pressure increases despite little change in systolic pressure. Although the high diastolic pressure is detected prior to 1650 min, SQI metrics fail to detect the artifactual segment after 1650, resulting in an underestimation of CO and an overestimation of R.

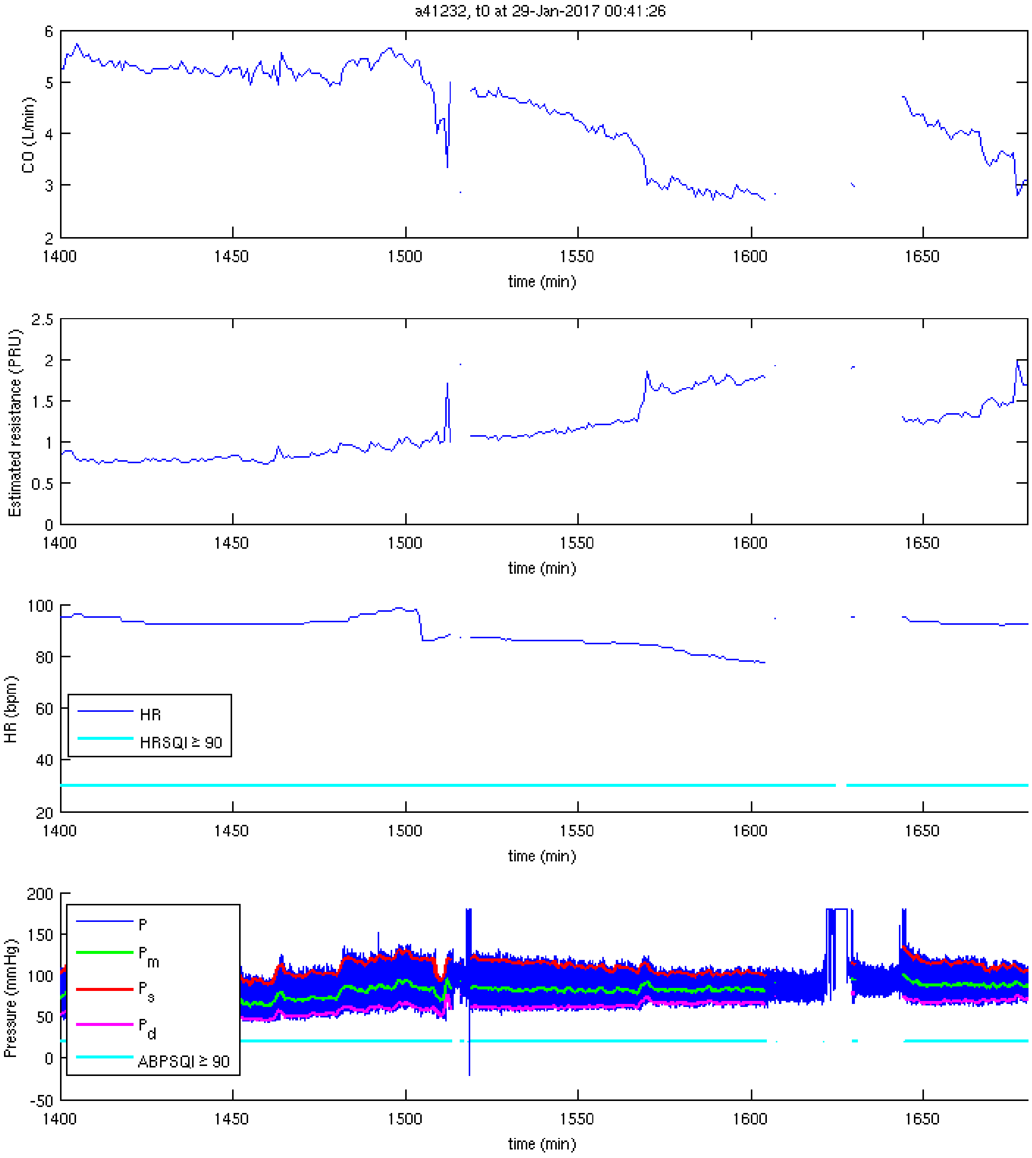

Figure 4-1: Estimated CO, estimated R, HR, and ABP for a41232. Periods of signal quality greater than 90 for HRSQI and ABPSQI are flagged on their respective plots.

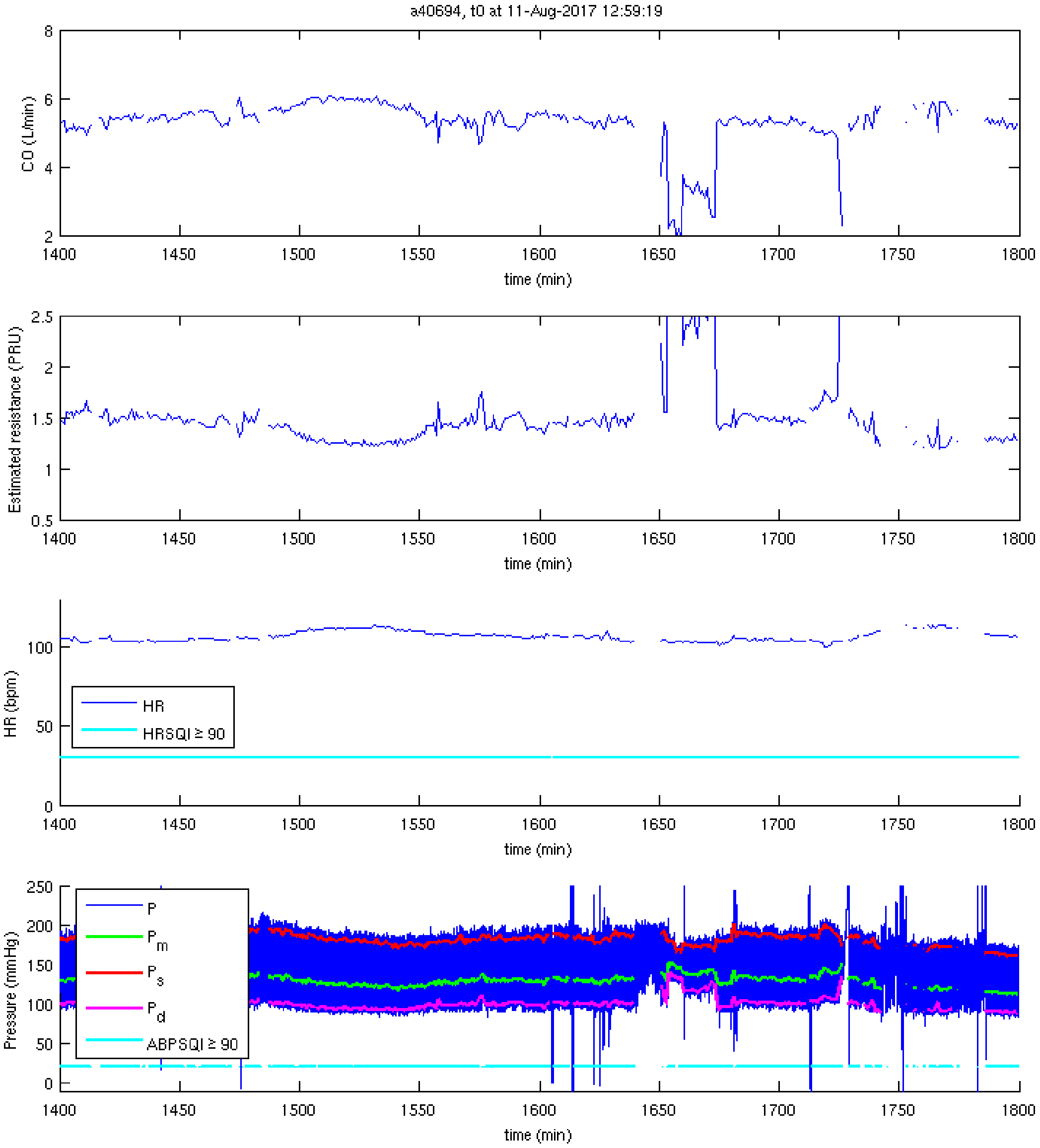

Figure 4-2: Estimated CO, estimated R, HR, and ABP for a40694. Periods of signal quality greater than 90 for HRSQI and ABPSQI are flagged on their respective plots.

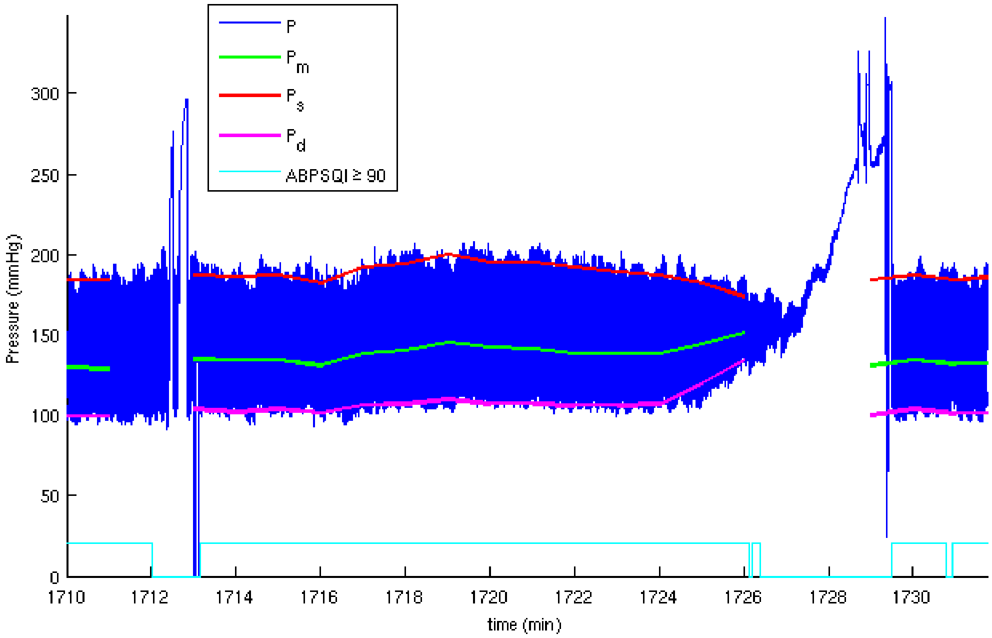

Figure 4-3: Example of artifact from a40694: saturation to mean.

Systolic pressure jumps can occur within the same vicinity as diastolic jumps in the same record. In Fig.4-4, diastolic pressure increases at about 2230 min to 2250 min, while systolic pressure remains stable. At 2470 minutes, the opposite occurs: systolic pressure decreases while diastolic pressure is relatively constant. We also see that at 2300 minutes, diastolic pressure slowly increases until the systolic pressure also decreases such that SQI metrics detect the non-physiological pressures. During each of these artifacts, estimated CO decreases dramatically, leading to corresponding increases in estimated resistance. If these periods were indeed a reflection of the patient's underlying hemodynamics, systolic, diastolic, and mean pressures would tend to change in the same direction.

4.1.3 Gradual artifacts requiring HR examination

Even by expert examination, some slow-moving changes are difficult to distinguish between artifactual and physiological. Fig.4-5 illustrates a case with a gradual decrease in systolic, diastolic, and mean blood pressures starting just before 600 min

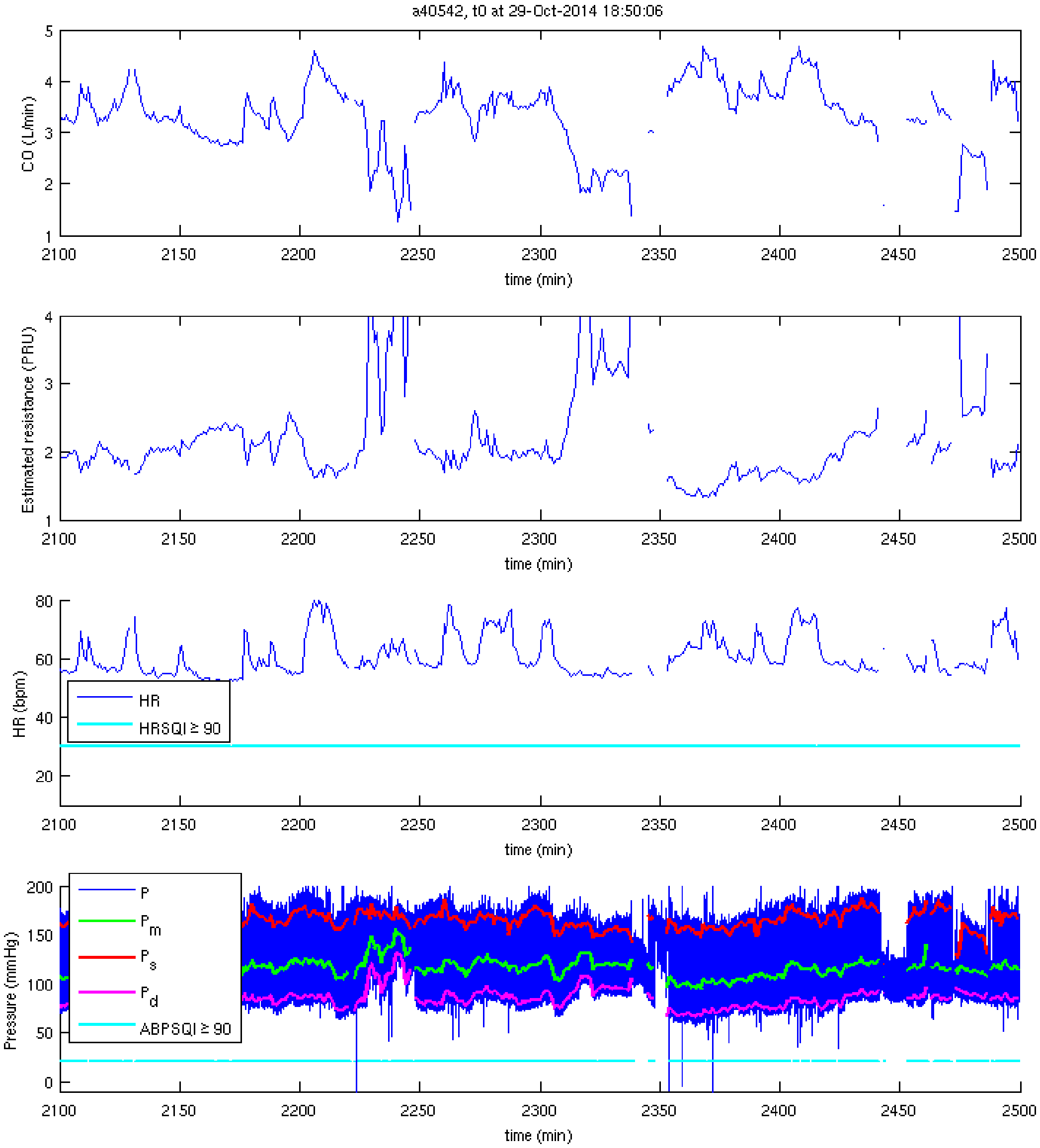

Figure 4-4: Estimated CO, estimated R, HR, and ABP for a40542. Periods of signal quality greater than 90 for HRSQI and ABPSQI are flagged on their respective plots.

and is restored to normal levels after over an hour. Although this type of artifact does not have a large impact on CO estimates, the resulting resistance estimate changes with the drop and rise in mean blood pressure. While this may be a plausible physiologic variation in blood pressure, the stable heart rate makes this hemodynamic fluctation suspicious. Further verification may be needed using other patient data such as medications administered, nurse's notes, or other sources of data.

A similar example is shown in Fig.4-6, where a gradual decrease in systolic, diastolic, and mean blood pressures occur at approximately 1260 min and is accompanied by a slight decrease in heart rate. Blood pressure and heart rate are restored at 1350 min. The gradual decrease in blood pressure may not appear to be an artifact, but an accompanying increase in heart rate, which would be a baroreceptor response, would appear more physiologically plausible unless the patient was severely compromised. Therefore, additional data would need to be reviewed to examine the blood pressure quality.

Other cases with varying systolic, diastolic, and mean pressures with relatively constant heart rates are shown in Fig.4-7 and Fig.4-8. In the case of Fig.4-8, thermodilution measurements are available, which indicate a gradual rise in CO. However, the fluctuations in estimated CO and estimated R with a relatively constant HR puts suspicion on the hemodynamic estimates.

4.2 Proposed damping detection method

Of these slow-changing artifacts, damping is one that can be potentially detected using simple signal processing techniques. The resulting ABP waveform often leads to an underestimation of pulse pressure and systolic pressure and an overestimation of diastolic pressure. Upon the onset of damping, systolic pressure slowly drops and diastolic pressure rises while the mean pressure remains constant until the signal fidelity deteriorates to a point in which the condition is brought to the attention of the ICU nurse. The tubing is then manually flushed, resulting in a sharp increase in pressure to the maximum level allowed by the bedside monitor, as shown in Fig.4-9.

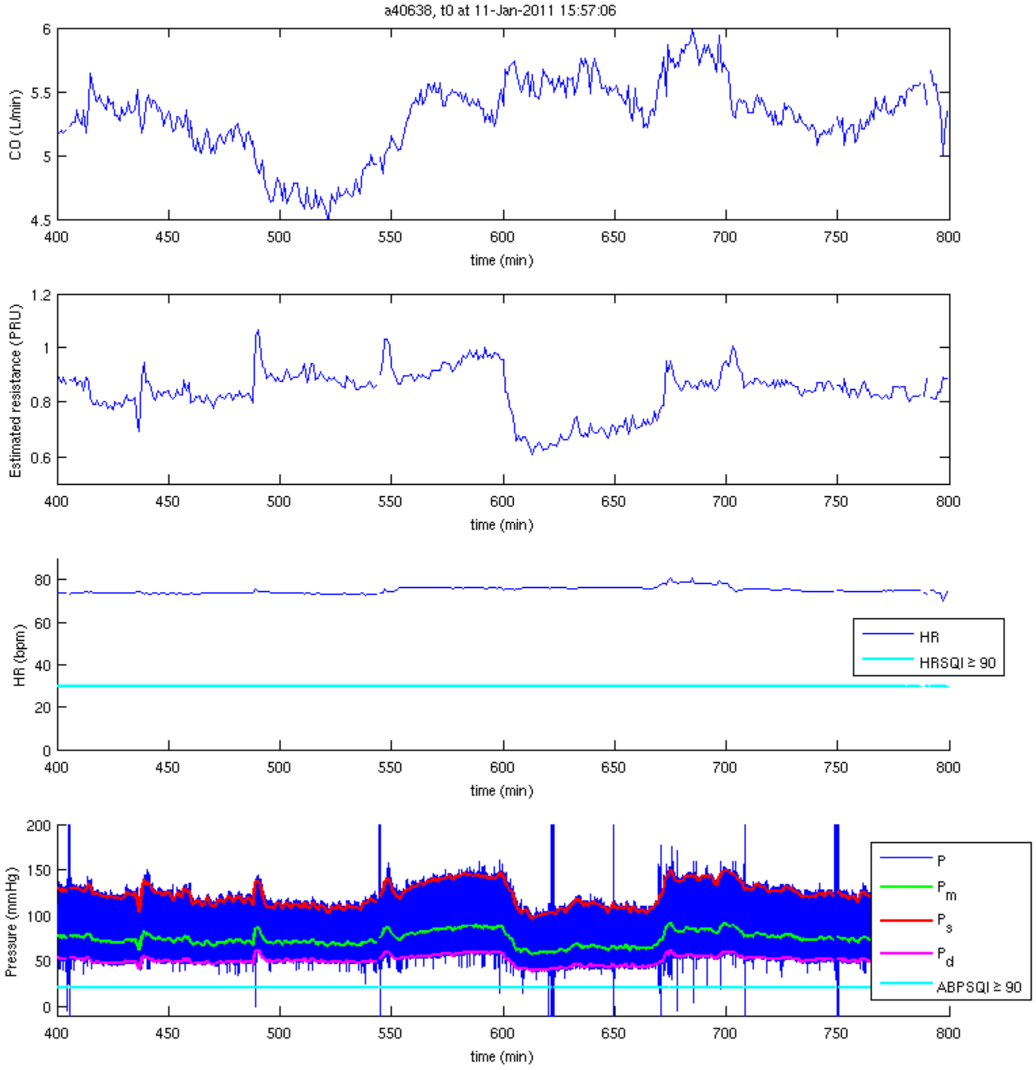

Figure 4-5: Estimated CO, estimated R, HR, and ABP for a40638. Periods of signal quality greater than 90 for HRSQI and ABPSQI are flagged on their respective plots.

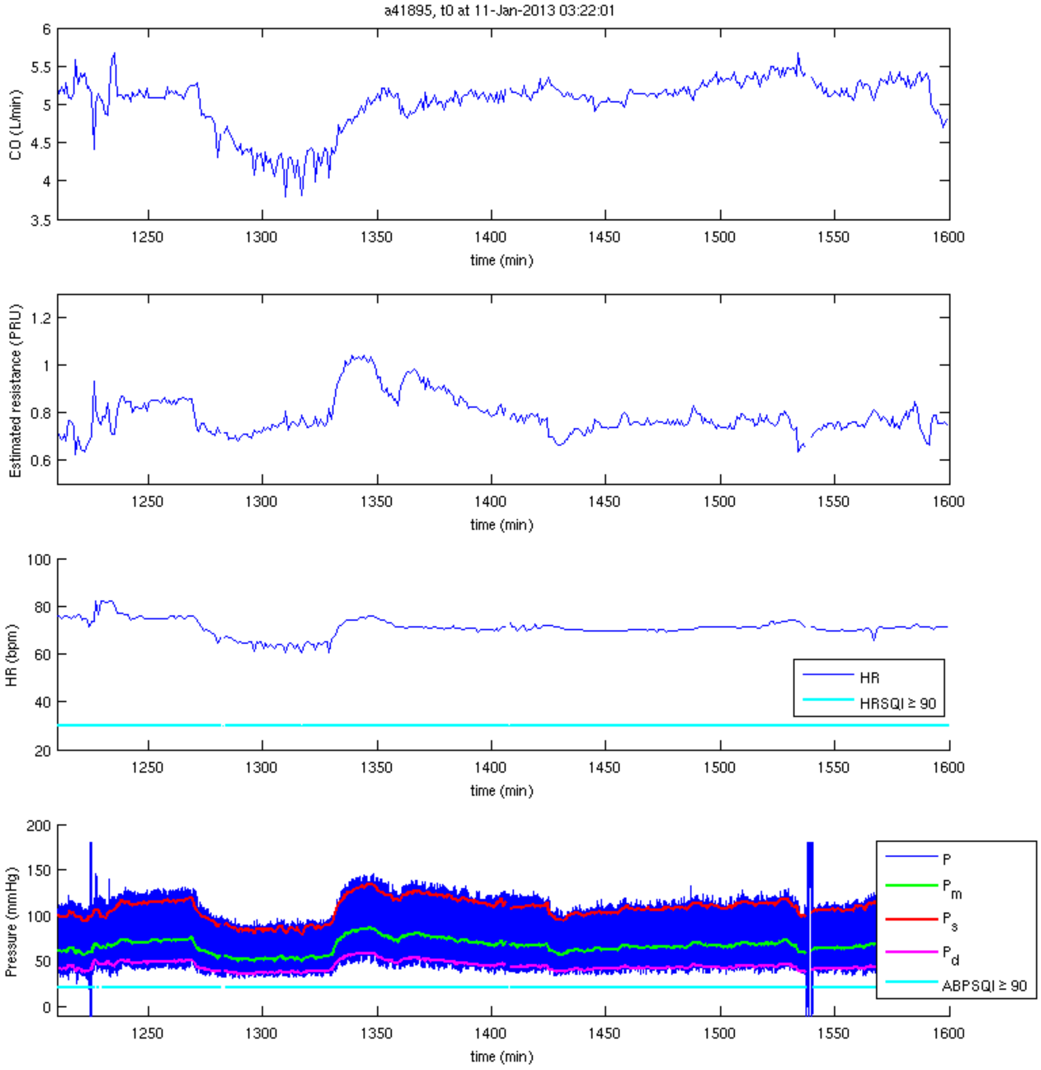

Figure 4-6: Estimated CO, estimated R, HR, and ABP for a41895. Periods of signal quality greater than 90 for HRSQI and ABPSQI are flagged on their respective plots.

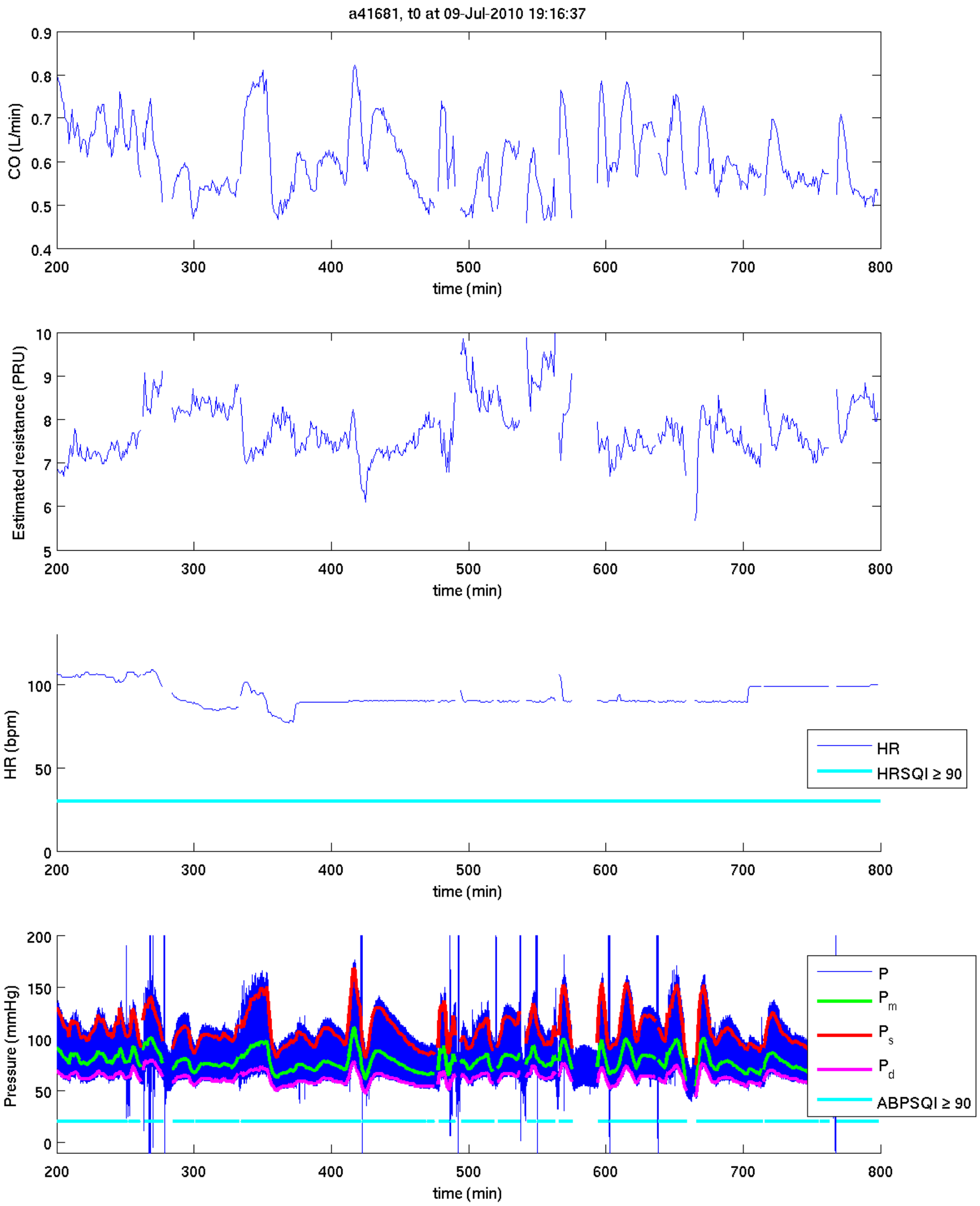

Figure 4-7: Estimated CO, estimated R, HR, and ABP for a41681. Periods of signal quality greater than 90 for HRSQI and ABPSQI are flagged on their respective plots.

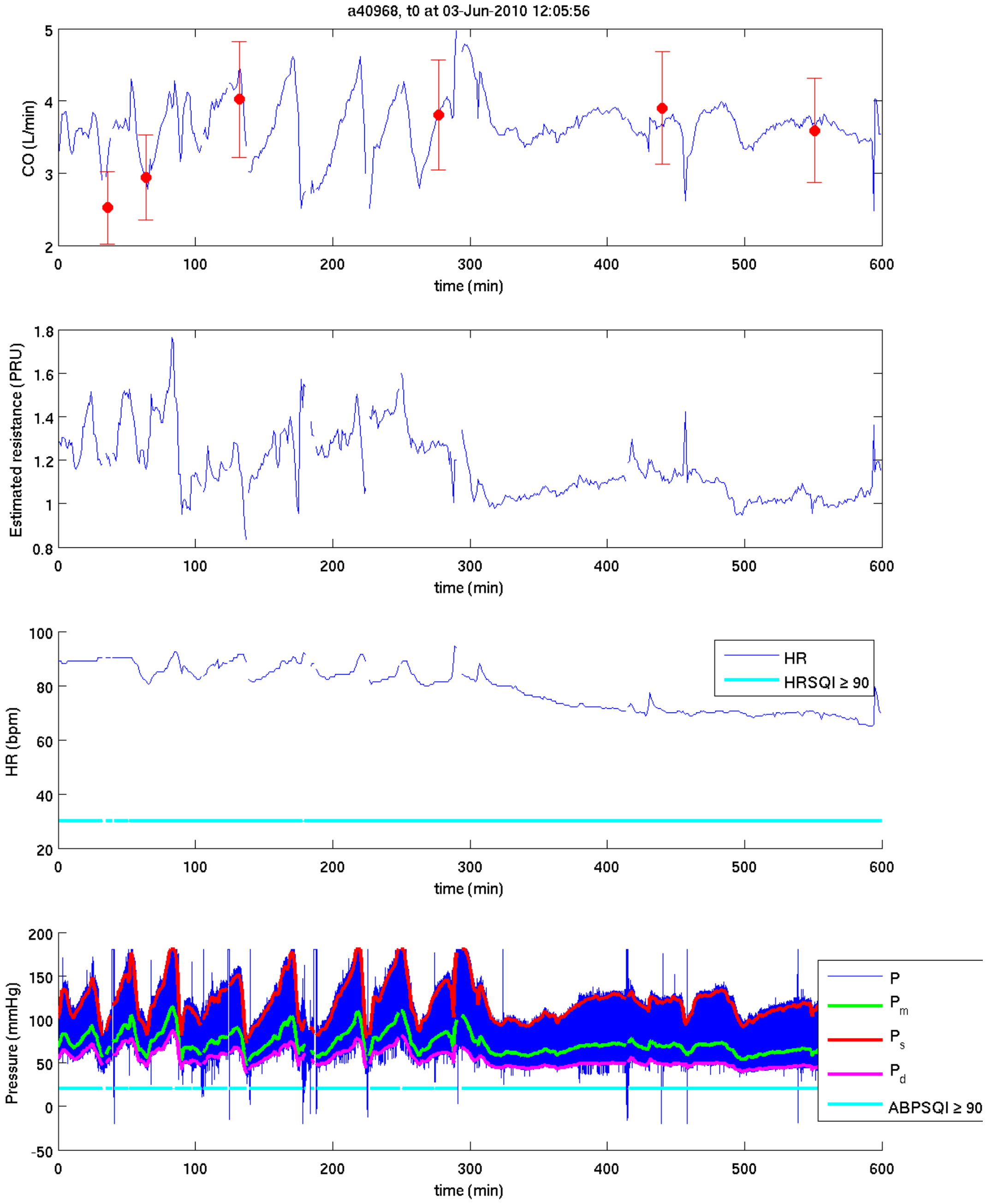

Figure 4-8: Estimated CO, estimated R, HR, and ABP for a40968. Thermodilution is shown in red with error bars of 20%. Periods of signal quality greater than 90 for HRSQI and ABPSQI are flagged on their respective plots.

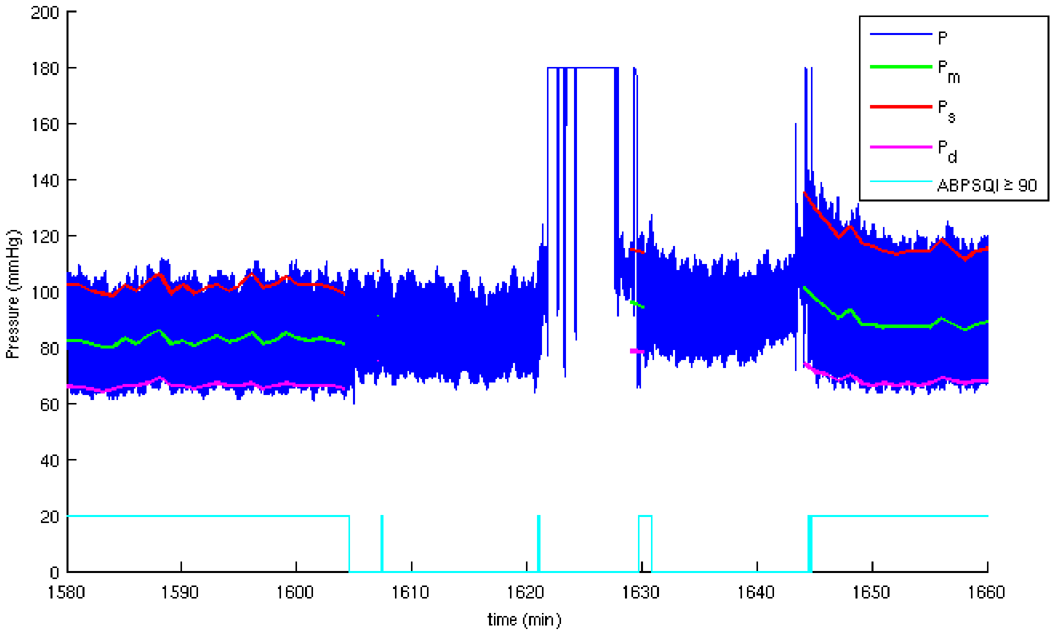

Figure 4-9: Example of artifact from a41232: damping and consequent flush.

After flushing, the ABP signal returns to its previous amplitude prior to damping, as seen in 4-1.

A proposed method of detecting damping is described in the following sections and outlined in Fig.4-10. Instantaneous ABP is denoted as $P[n]$.

4.2.1 Flushing detection

During flushing, blood pressure saturates to the maximum readings allowed by the patient monitoring system. The flushing artifact resembles a square wave, denoted as $\Pi_N[n]$:

$$\Pi_N[n] = \begin{cases} 1, & |n| \leq N \\ 0 & |n| > N. \end{cases}$$

N, in units of samples, would be determined by examining a large number of flushing artifacts and finding the average duration in number of samples of each flushing. To detect flushing, a convolution operation can be performed on the ABP

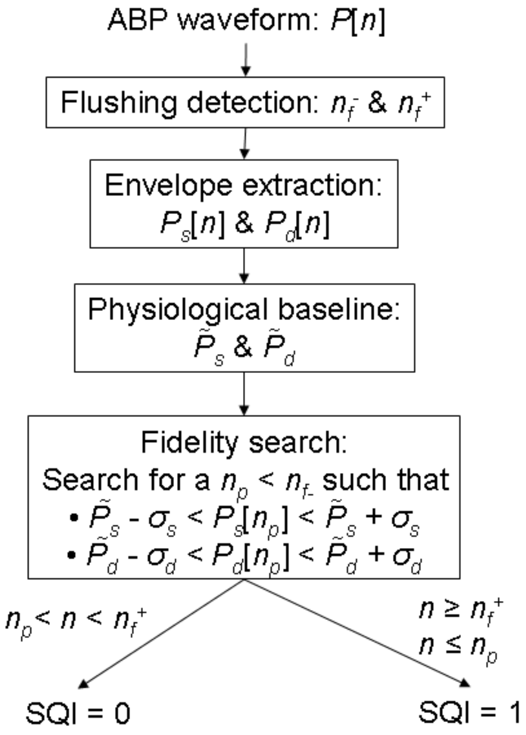
ABP waveform: P[n]
Flushing detection: n_f^- & n_f^+
Envelope extraction: $P_s[n]$ & $P_d[n]$
Physiological baseline: $\tilde{P}_s$ & $\tilde{P}_d$
Fidelity search: Search for a $n_p < n_{f-}$ such that
• $\tilde{P}_s - \sigma_s < P_s[n_p] < \tilde{P}_s + \sigma_s$
• $\tilde{P}_d - \sigma_d < P_d[n_p] < \tilde{P}_d + \sigma_d$
$n_p < n < n_f^+$
$n \geq n_f^+$
$n \leq n_p$
SQI = 0
SQI = 1

Figure 4-10: Proposed damping detection method.

waveform:

$$x[n] = P[n] * \Pi_N[n]$$

Areas where $x[n]$ exceeds an empirically determined threshold would correspond with flushings in the ABP waveform. The sample after blood pressure is restored after flushing is designated as n_f^+, while the sample immediately before the flushing is designated as n_f^-, as shown in Fig.4-14.

4.2.2 Envelope extraction

To monitor the progression of damping, the upper and lower envelopes of the ABP waveform need to be extracted. The systolic and diastolic pressures represent the upper and lower envelopes, respectively, and can be obtained using beat extraction algorithm *wabp* and selecting the maximum and minimum pressures within each beat.

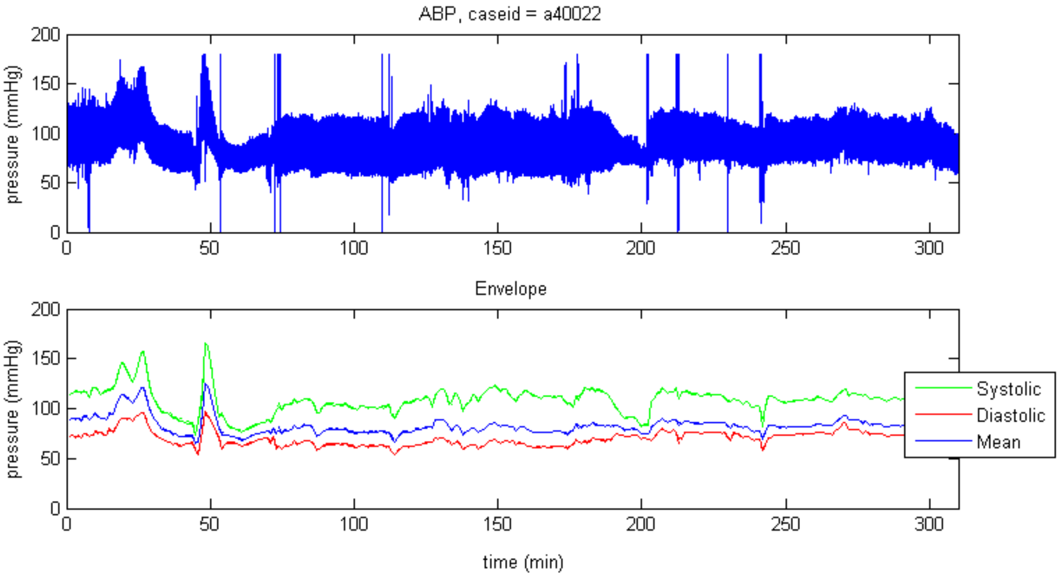

Figure 4-11: Envelope extraction for a40022.

Presumably, these pressures would have to be extracted for any cardiac output or resistance estimation, thereby adding little additional computation for envelope extraction. By applying a median filter to the systolic and diastolic beat-by-beat pressures, the upper and lower envelopes can be computed, designated as $P_s[n]$ and $P_d[n]$ respectively. The length of the filter can be determined empirically but should be high enough to remove sudden artifacts. An example is shown in Fig.4-11, whereby a one-minute median filter was applied to the maximum and minimum pressures within each detected beat. The mean pressure is also shown.

Other envelope extraction methods, such as the RMS or Hilbert methods [14], can be used for a computationally more efficient way of computing upper and lower envelopes if systolic and diastolic pressures are not readily available. The results of these methods are shown in Fig.4-12 and Fig.4-13 for RMS and Hilbert methods respectively. Median filters can be applied to the upper and lower envelopes to eliminate sudden spikes in blood pressure.

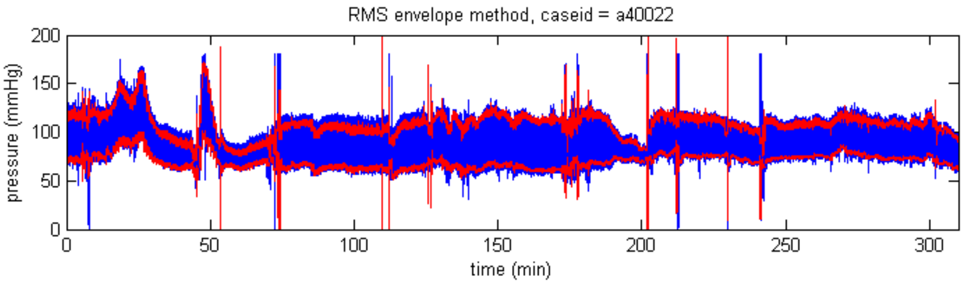

Figure 4-12: Envelope extraction for a40022 using the RMS method.

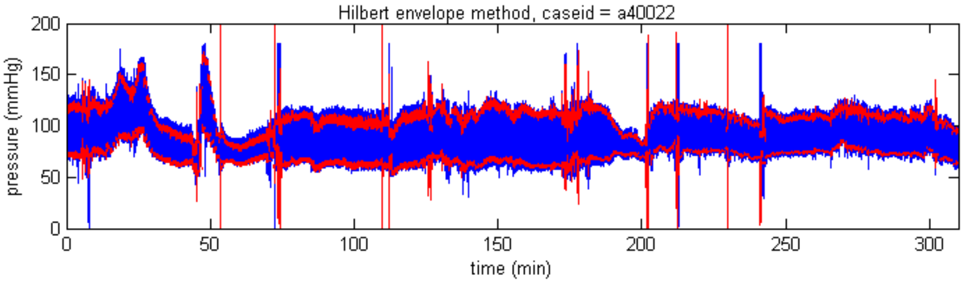

Figure 4-13: Envelope extraction for a40022 using the Hilbert method.

4.2.3 Fidelity search

ABP after the characteristic flush of a damped waveform is often restored to normal levels. A baseline level of physiological systolic, diastolic, and mean pressures can be obtained by taking the median of a segment of ABP after flush. These baseline levels are designated as $\tilde{P}_s$, $\tilde{P}_d$, and $\tilde{P}_m$ for systolic, diastolic, and mean pressures respectively. The length of the segment W should be determined empirically. Let $f(x[n], x[n+1], ...x[n+W])$ denote the median operation of the n to $n+W$ points in x. The baseline levels are:

$$\tilde{P}_s = f\left(P_s[n_f^+], P_s[n_f^+ + 1], ...P_s[n_f^+ + W]\right)$$

$$\tilde{P}_d = f\left(P_d[n_f^+], P_d[n_f^+ + 1], ...P_d[n_f^+ + W]\right)$$

$$\tilde{P}_m = \left(\frac{1}{3}\right)\left(\tilde{P}_s - \tilde{P}_d\right) + \tilde{P}_d$$

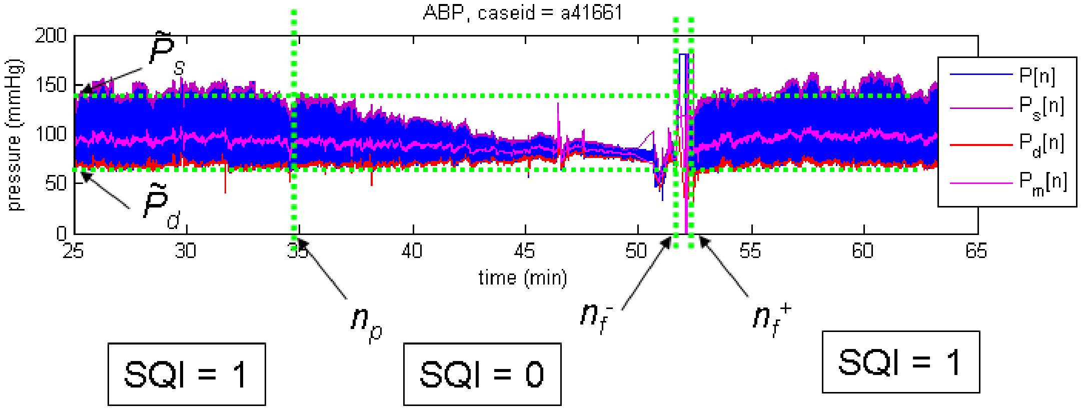

Figure 4-14: Fidelity search for a41661.

After physiological levels for ABP are established, ABP prior to the flush should be searched to locate baseline levels in order to determine when the damping started. Because of physiological fluctuations, an empirically-determined pressure interval σ_s and σ_d should be added to baseline pressures in this search for both the upper and lower envelopes. Physiological areas of ABP prior to the flush should have envelopes that be satisfy the following inequalities:

$$\tilde{P}_s - \sigma_s < P_s[n < n_f^-] < \tilde{P}_s + \sigma_s$$

$$\tilde{P}_d - \sigma_d < P_d[n < n_f^-] < \tilde{P}_d + \sigma_d$$

The last sample of the physiological segment prior to the flush that satisfies these inequalities is designated as n_p. To ensure that the label n_p is not mistakenly assigned to a segment when noisy areas between n_p and $n < n_f^-$ fulfill this inequality, n_p should be assigned only when a window prior to n_p also satisfies the above inequalities.

All n between n_p and $n < n_f^+$ should be designated as poor SQI (SQI=0). $n \geq n_f^+$ and $n \leq n_p$ should be designated as good SQI (SQI=1), subject to correction by existing ABP signal quality metrics such as $jSQI$ and $wSQI$. An example of such a fidelity search is shown in Fig.4-14.

Chapter 5

Conclusion

5.1 Summary

In this thesis, the effect of signal quality indices for both heart rate and arterial blood pressure were examined on six different cardiac output estimators. The clinical utility of the CO estimators were analyzed by estimating the peripheral resistance derived from the Liljestrand and LC estimators. Changes in vasoactive medication doses were related with changes in estimated R, revealing the limitations of current SQI methods.

Chapter 2 described estimator methods and discussed results from analyzing the accuracy of estimators after incorporating SQI metrics. SQI correction for both ABP and HR were used, as segments in the ABP waveform were ignored if they did not meet both HRSQI and ABPSQI criteria. Six CO estimators (four lumped-parameter models and two systolic area methods) were compared at HRSQI $\geq$ 50 and varying ABPSQI. At all levels of SQI, the Liljestrand estimator yielded the lowest error, with thermodilution being the gold standard. As HRSQI and ABPSQI requirements increased, estimated CO errors decreased while reducing little of the available data. A SQI threshold of 90 for both HRSQI and ABPSQI using the Liljestrand estimate was recommended for estimates over 1-minute intervals. At these thresholds, the lowest gross root mean square normalized error (RMSNE) was found to be 15.4% (or 0.74 L/min) and average RMSNE was 13.7% (0.71 L/min). Based on these results, a linear combination (LC) of the six CO estimation methods was developed and proved superior to all other methods when up to 13 TCO calibration values were used.

Chapter 3 discussed the clinical utility of CO estimates. Estimated resistance was calculated using the ratio of mean ABP and estimated CO derived using the recommended procedure from Chapter 2. Four vasoactive medications (two vasodilators and two vasoconstrictors) were extracted for 37 cases, and times when medication level changed after 90 minutes of constant dose levels were examined. For each event, the change in medication level and the corresponding change estimated resistance was examined. However, regression analysis failed to show a significant correlation between changes and slopes of dose level and estimated resistance, whether that be resistance derived from the Liljestrand estimator or the LC estimator, a linear combination of the 6 estimators examined in Chapter 2.

Chapter 4 draws upon examples that indicate the limitations of current SQI metrics, particularly for ABP. While ABPSQI, a combination of *jSQI* and *wSQI*, are useful in detecting artifacts or non-physiological changes that occur within a few beats, gradual ABP distortions that occur over the span of tens of minutes are not recognized.

5.2 Areas for future work

Various methods have been developed to calibrate CO estimates studied in this thesis. While the global calibration method is applicable for calibrating for a retrospective analysis, a first point calibration or online calibration method can be explored for its effect on estimation error. If a larger data set is available, the thermodilution points can be split into two sets: a training set on which the TCOs can be used for calibrating estimated cardiac output, and a test set on which to evaluate the CO estimation error on.

Other measures of clinical utility can be examined using an approach similar to that used to correlate vasoactive medication with estimated resistance. A similar analysis of inotropic agents can be performed to determine the relationship between medication level and cardiac output. An interesting area of research would be to see how well the cardiac output estimates, along with other clinically available data, predicts septic shock, hemorrhage, or cardiogenic shock.

However, without an additional signal quality index to detect slow-changing artifacts in the arterial blood pressure waveform, the usefulness of the CO estimation procedure used in this thesis is limited. The damping detector proposed in Chapter 4 is one step towards a more reliable CO estimate, but other types of gradually changing forms of non-physiological blood pressure waveforms need to be accounted for in any reliable CO estimate. However, it is likely that CO estimates will have to be back-corrected retrospectively when flush artifacts are detected. This constraint may prove unacceptable and clinical practice may require an independent blood pressure observation, such as that derived from a cuff. When such independent observations are compared to invasive data, large continued differences may prompt clinical teams to perform flush tests or adjust the catheter or transducer position, thereby improving the overall quality of data.

Bibliography

[1] O.T. Abdala, T. Chen, and G.D. Clifford. Combining Multiple Cardiac Output Estimators to Reduce Error. *In submission to Computers in Cardiology*, 2009.

[2] W. Banasiak, C. Telichowski, K. Kokot, and A. Telichowski. Diurnal fluctations of arterial blood pressure and heart rate in patients with atrial fibrillation. *Wiad Lek*, 45(15-16):584–588, 1992.

[3] H. Barcroft, O.G. Edholm, J. McMichael, and E.P. Sharpey-Schafer. Posthaemorrhagic fainting: study by cardiac output and forearm flow. *Lancet*, 246:489–491, 1944.

[4] H.C. Bazett. An analysis of the time-relations of electrocardiograms. *Heart*, 7:353–370, 1920.

[5] G. D. Clifford, M. Villarroel, and D. J. Scott. User guide and documentation for the MIMIC II database. http://mimic.mit.edu/documentation.html, April 2008. Rev: 179.

[6] A.F. Connors, T. Speroff, N.V. Dawson, and Thomas C. et al. The effectiveness of right heart catheterization in the initial care of critically ill patients. *JAMA*, 276:889–897, 1996.

[7] L.S. Costanzo. *Physiology*. Saunders and Company, 3rd edition, 2006.

[8] L.A.H. Critchley and J.A.J.H. Critchley. A meta-analysis of studies using bias and precision statistics to compare cardiac output measurement techniques. *J Clin Monit*, 15:85–91, 1999.

[9] B. Efron and R.J. Tibshirani. *An introduction to the bootstrap*. Chapman & Hall, 1997.

[10] J. Erlanger and B. Hooker. *Johns Hopkins Hospital Report*, 12:147–378, 1904.

[11] K. Espersen, E.W. Jensen, D. Rosenborg, J.K. Thomsen, K. Elisasen, N.V. Olsen, and I.L. Kanstrup. Comparison of cardiac output measurement techniques: thermodilution, doppler, co2-rebreathing and the direct fick method. *Acta Anaesthesiol Scand*, 39(2):245–251, 1995.

[12] G. Fegler. Measurement of cardiac output in anaesthetized animals by a thermodilution method. *Q J Exp Physiol Cogn Med Sci*, 39(3):153–64, 1954.

[13] A.C. Guyton and J.E. Hall. *Textbook of Medical Physiology.* Saunders and Company, 11th edition, 2005.

[14] S.L. Hahn. *Hilbert transforms in signal processing.* Artech House Publishers, 1996.

[15] T. Heldt. Continuous blood pressure-derived cardiac output monitoring–should we be thinking long term? *Journal of Applied Physiology*, 101(2):373, 2006.

[16] J. Herd, N. Leclair, and W. Simon. Arterial pressure pulse contours during hemorrhage in anesthetized dogs. *Journal of Applied Physiology*, 21, 1966.

[17] M.M. Hoeper, R. Maier, J. Tongers, J. Niedermeyer, J.M. Hothfield, M. Hamm, and H. Faber. Determination of cardiac output by the fick method, thermodilution, and acetylene rebreathing in pulmonary hypertension. *Am J Resp and Crit Care Med*, 160(2):535–541, 1999.

[18] S.M. Horvath and D.W. Knapp. Hemodynamic effects of neosynephrine. *American Journal of Physiology*, 178(3):387–391, 1954.

[19] L.L. Huntsman, D.K. Stewart, S.R. Barnes, S.B. Franklin, J.S. Colocousis, and E.A. Hessel. Noninvasive doppler determination of cardiac output in man: clinical validation. *Circulation*, 67:592–602, 1983.

[20] J.R.C. Jansen, R.W. Johnson, J.Y. Yan, and P.D. Verdouw. Near continuous cardiac output by thermodilution. *J Clin Monit*, 13:233–239, 1997.

[21] B. A. Janz, G. D. Clifford, and R. G. Mark. Multivariable Analysis of Sedation, Activity and Agitation in Critically Ill Patients Using the Riker Scale, ECG, Blood Pressure and Respiratory Rate. *Computers in Cardiology*, 32:735–738, September 2005.

[22] T. Kaobi, S. Kaukinen, T. Ahola, and V.M. Turjanmaa. Noninvasive measurement of cardiac output: whole-body impedance cardiography in simultaneous comparison with thermodilution and direct fick oxygen methods. *Int Care Med*, 23(11):1132–1137, 1997.

[23] N.T. Kouchoukos, L.C. Sheppard, and D.A. McDonald. Estimation of stroke volume in the dog by a pulse contour method. *Circulation Research*, 26:611–623, 1970.

[24] Q. Li and GD Clifford. Realistic artificial arterial blood pressure artifact algorithms and an evaluation of a robust blood pressur estimator. *In submission to Biomedical Engineering Online*, 2007.

[25] Q. Li, GD Clifford, and RG Mark. Robust heart rate estimation from multiple asynchronous noisy sources using signal quality indices and a Kalman filter. *Physiological measurement*, 29(1):15–32, 2008.

[26] G. Liljestrand and E. Zander. *Experimental Medicine*, 59:105, 1940.

[27] J.D. Mackenzie, N.E. Haites, and J.M. Rawles. Method of assessing the reproducibility of blood flow measurement: Factors influencing the performance of thermodilution cardiac output computers. *Br Heart J*, 55:14–24, 1986.

[28] P.L. Marino. *The ICU Book*. Lippincott Williams & Wilkins, 3rd edition, 2007.

[29] R.G. Mark. MIT 6.022J Course Reader, Introduction: The Functional Anatomy of the CV System, 2008.

[30] T.M. Masterson, T.C. Rothenhaus, and S.M. Tenner. *The ICU Intern Pocket Survival Guide*. International Medical Publishing, 10th edition, 2003.

[31] T. Nishikawa and S. Dohi. Errors in the measurement of cardiac output by thermodilution. *Canadian Journal of Anaesthesia*, 40(2):142–153, February 1993.

[32] T. Parlikar. *Modeling and Monitoring of Cardiovascular Dynamics for Patients in Critical Care*. PhD thesis, MIT, 2007.

[33] R. Rosenthal and D.B. Rubin. A simple, general purpose display of magnitude of experimental effects. *Journal of Educational Psychology*, 2:166–169, 1982.

[34] M. Saeed, G. Lieu, C.and Raber, and R. G. Mark. MIMIC II: a massive temporal ICU patient database to support research in intelligent patient monitoring. *Computers in Cardiology*, 29:641–644, September 2002.

[35] B.V. Scheer, A. Perel, and U.J. Pfeiffer. Clinical review: Complications and risk factors of peripheral arterial catheters used for haemodynamic monitoring in anaesthesia and intensive care medicine. *Critical Care*, 6(3):198–204, 2002.

[36] C.W. Stetz, R.G. Miller, G.E. Kelly, and T.A. Raffin. Reliability of the thermodilution method in the determination of cardiac output in clinical practice. *Am Rev Respir Dis*, 126(6):1001–1004, December 1982.

[37] J.X. Sun. Cardiac output estimation using arterial blood pressure waveforms. Master's thesis, MIT, 2005.

[38] J.X. Sun, A.T. Reisner, and R.G. Mark. A signal abnormality index for arterial blood pressure waveforms. *Computers in Cardiology*, 32:13–16, September 2005.

[39] J.X. Sun, A.T. Reisner, M. Saeed, and R.G. Mark. Estimating cardiac output from arterial blood pressure waveforms: a critical evaluation using the MIMIC II database. *Computers in Cardiology*, 32:295–298, September 2005.

[40] H. Warner, H. Swan, D. Connolly, R. Tompkins, and E. Wood. Quantitation of beat-to-beat changes in stroke volume from the aortic pulse contour in man. *Journal of Applied Physiology*, 5:492, 1953.

[41] K. Wesseling, B. Wit, J. Weber, and N. Smith. A simple device for the continuous measurement of cardiac output. *Advanced Cardiovascular Physiology*, 5, 1983.

[42] SW White, AW Quail, PW De Leeuw, FM Traugott, WJ Brown, WL Porges, and DB Cottee. Impedance cardiography for cardiac output measurement: an evaluation of accuracy and limitations. *European heart journal*, 11:79, 1990.

[43] W. Zong, T. Heldt, GB Moody, and RG Mark. An open-source algorithm to detect onset of arterial blood pressure pulses. *Computers in Cardiology, 2003*, pages 259–262, 2003.

[44] W. Zong, G.B. Moody, and R.G. Mark. Reduction of false arterial blood pressure alarms using signal quality assessement and relationships between the electrocardiogram and arterial blood pressure. *Medical and Biological Engineering and Computing*, 42(5):698–706, 2004.